



Michigan Technological University  
*Create the Future* Digital Commons @ Michigan Tech

---

Dissertations, Master's Theses and Master's  
Reports - Open

Dissertations, Master's Theses and Master's  
Reports

---

2012

## Laser Thomson scattering measurements of electron temperature and density in a Hall-effect plasma

Robert L. Washeleski

Follow this and additional works at: <https://digitalcommons.mtu.edu/etds>



Part of the [Mechanical Engineering Commons](#)

Copyright 2012 Robert L. Washeleski

---

### Recommended Citation

Washeleski, Robert L., "Laser Thomson scattering measurements of electron temperature and density in a Hall-effect plasma", Dissertation, Michigan Technological University, 2012.  
<https://doi.org/10.37099/mtu.dc.etds/422>

Follow this and additional works at: <https://digitalcommons.mtu.edu/etds>



Part of the [Mechanical Engineering Commons](#)

LASER THOMSON SCATTERING MEASUREMENTS OF ELECTRON  
TEMPERATURE AND DENSITY IN A HALL-EFFECT PLASMA

By  
Robert L. Washeleski

A DISSERTATION  
Submitted in partial fulfillment of the requirements for the degree of  
DOCTOR OF PHILOSOPHY  
(Mechanical Engineering-Engineering Mechanics)

MICHIGAN TECHNOLOGICAL UNIVERSITY  
2012

© 2012 Robert L. Washeleski



This dissertation, "Laser Thomson Scattering Measurements of Electron Temperature and Density in a Hall-Effect Plasma," is hereby approved in partial fulfillment of the requirements for the Degree of DOCTOR OF PHILOSOPHY IN MECHANICAL ENGINEERING-ENGINEERING MECHANICS.

Department of Mechanical Engineering-Engineering Mechanics

Signatures:

Dissertation Advisor \_\_\_\_\_  
Dr. Lyon B. King

Department Chair \_\_\_\_\_  
Dr. William Predebon

Date \_\_\_\_\_



*In olden times men thought of their world as consisting of four substances – earth, air, fire, and water. It is now realized that, from a scientific point of view, modern man must also classify natural phenomena in terms of the behavior of four states of matter – solid, liquid, gaseous, and plasma. The plasma state can be distinguished from the other states of matter in that a significant number of its molecules are in the electrically charged or ionized state. The fact that the two lists can be related to each other is rather intriguing, and in doing this the reader may ponder how far we have come in our ability to describe the world around us.*

*-E. H. Holt and R. E. Haskell in “Foundations of Plasma Dynamics”*



# Contents

<b>List of Figures</b> . . . . .	<b>xiii</b>
<b>List of Tables</b> . . . . .	<b>xxiii</b>
<b>Acknowledgments</b> . . . . .	<b>xxv</b>
<b>Abstract</b> . . . . .	<b>xxvii</b>
<b>1 Introduction</b> . . . . .	<b>1</b>
1.1 Measurement of Electron Properties in Hall-effect Thrusters . . . . .	1
1.2 Aim and Scope . . . . .	4
1.3 Structure . . . . .	5
<b>2 Background and Review of Prior Research</b> . . . . .	<b>7</b>
2.1 Introduction . . . . .	7
2.2 Hall Thrusters . . . . .	8
2.3 Current Electron Diagnostic Techniques . . . . .	11
2.4 Laser Thomson Scattering Review . . . . .	14
2.4.1 Early Work . . . . .	15



2.4.2	Fusion Plasmas . . . . .	15
2.4.3	Extension to Cold Plasmas . . . . .	16
2.4.4	Application to Miniature Ion Thrusters . . . . .	18
2.5	Contribution of this Work . . . . .	19
<b>3</b>	<b>Laser Scattering from Plasma . . . . .</b>	<b>21</b>
3.1	Introduction . . . . .	21
3.2	Rayleigh Scattering . . . . .	22
3.3	Thomson Scattering . . . . .	24
3.3.1	Single Electron . . . . .	24
3.3.2	Scattering from Plasma . . . . .	29
3.4	Laser-Plasma Interaction . . . . .	33
3.4.1	Plasma Heating . . . . .	34
3.4.2	Photo-Ionization . . . . .	35
3.5	Summary of Key Assumptions . . . . .	36
<b>4</b>	<b>Electrostatic Probe Diagnostics . . . . .</b>	<b>39</b>
4.1	Introduction . . . . .	39
4.2	Single Langmuir Probes . . . . .	40
4.2.1	Theory of Operation . . . . .	41
4.2.2	Single Probe Trace Analysis and Limitations . . . . .	43
4.3	Double Langmuir Probes . . . . .	46
4.3.1	Theory of Operation . . . . .	46

4.3.2	Probe Trace Analysis and Advantages . . . . .	48
4.3.3	Double Probe Advantages and Disadvantages . . . . .	51
4.4	Probe Design and Implementation . . . . .	52
<b>5</b>	<b>Equipment and Procedures . . . . .</b>	<b>55</b>
5.1	Introduction . . . . .	55
5.2	Equipment . . . . .	56
5.2.1	Vacuum Facility . . . . .	56
5.2.2	Motion Table . . . . .	56
5.2.3	Thruster . . . . .	58
5.2.4	Cathode . . . . .	58
5.2.5	Mass Flow Controllers . . . . .	59
5.2.6	Laser . . . . .	60
5.2.7	Beam Dump and Viewing Dump . . . . .	61
5.2.8	Spectrograph . . . . .	64
5.2.9	iCCD Camera . . . . .	67
5.2.10	Laser Entrance Optics . . . . .	68
5.2.11	Collection Optics . . . . .	70
5.3	Data Acquisition . . . . .	72
5.4	System Alignment and Calibration . . . . .	74
5.4.1	Alignment . . . . .	74
5.4.2	Rayleigh Calibration . . . . .	76

5.5	Procedure . . . . .	77
5.5.1	Measuring the Thomson Scattering Spectrum . . . . .	77
5.5.2	Laser Measurements . . . . .	82
5.5.3	Probe Measurements . . . . .	84
<b>6</b>	<b>Laser Data Analysis . . . . .</b>	<b>85</b>
6.1	Introduction . . . . .	85
6.2	Thomson Scattering Detection . . . . .	86
6.3	Experimental Challenges . . . . .	89
6.3.1	Difficult Optical Access . . . . .	89
6.3.2	Alignment . . . . .	92
6.4	Determining the Corrected Spectrum . . . . .	94
6.5	Current Methods of Data Processing . . . . .	96
6.5.1	Single-Pulse Measurement . . . . .	96
6.5.2	Pulse Accumulation . . . . .	97
6.5.3	Thresholding . . . . .	101
6.6	New Method: Maximum Likelihood Estimation . . . . .	104
6.6.1	Basics of Maximum Likelihood Estimation . . . . .	105
6.6.2	MLE Applied to Laser Thomson Scattering . . . . .	108
6.7	MLE Processing Algorithm . . . . .	112
6.7.1	MLE Spectrum Analysis . . . . .	114
6.7.2	Determination of Electron Temperature and Density . . . . .	119

6.7.3	Advantages of MLE . . . . .	123
<b>7</b>	<b>Near-Field Plume Measurements . . . . .</b>	<b>125</b>
7.1	Introduction . . . . .	125
7.2	Experimental Parameters and Test Matrix . . . . .	126
7.3	Electron Temperature Measurements . . . . .	129
7.3.1	Probe Results . . . . .	129
7.3.2	Thresholding Results . . . . .	130
7.3.3	MLE Results . . . . .	134
7.3.4	Comparison of Temperature Measurements . . . . .	136
7.4	Plasma Density Measurements . . . . .	141
7.4.1	Probe Results . . . . .	141
7.4.2	Thresholding Results . . . . .	142
7.4.3	MLE Results . . . . .	144
7.4.4	Comparison of Density Measurements . . . . .	145
7.5	Uncertainty, Accuracy, and Signal to Noise Ratio . . . . .	148
7.5.1	Laser Measurements . . . . .	148
7.5.2	Probe Measurements . . . . .	156
7.6	LTS versus Double Probes . . . . .	158
<b>8</b>	<b>Conclusion and Future Work . . . . .</b>	<b>167</b>
8.1	Introduction . . . . .	167
8.2	Summary of Experimental Results . . . . .	168

8.3	Improvements and Future Work . . . . .	170
8.3.1	External Measurements . . . . .	170
8.3.2	Internal Measurements . . . . .	173
8.4	Conclusion . . . . .	181
<b>References . . . . .</b>		<b>185</b>
<b>A Langmuir Probe Traces . . . . .</b>		<b>199</b>
<b>B Folding the Spectrum . . . . .</b>		<b>213</b>

# List of Figures

2.1	Cross-section of a typical Hall-effect thruster. ©2012 M. Hopkins and R. Washeleski. . . . .	10
2.2	Process of determining electron temperature and density using optical emission spectroscopy. . . . .	13
3.1	Solution Coordinates. $R_q$ is the vector from the scattering electron to the observation point and $\hat{R}_q$ is the unit vector with the same direction as R. .	26
3.2	Vector Geometry for General Scattering . . . . .	28
3.3	Scattering Geometry for MTU LTS Diagnostic . . . . .	30
4.1	Ideal (solid) and typical (dashed) single Langmuir probe traces (©2009 Jason Sommerville, used with permission). . . . .	44
4.2	Ideal double probe trace. . . . .	47
4.3	Actual double probe trace (gray) with curve fit (black). . . . .	49
5.1	Motion Table with Probe Stand . . . . .	57
5.2	Photograph of the cathode location on the thruster. The cathode was mounted to the side in order to allow a clear path for the laser beam. . . .	59

5.3	Low Dust Laser Enclosure . . . . .	62
5.4	Schematic of the beam dump using black glass at Brewster's angle. . . . .	63
5.5	Picture of the inside of the custom beam dump. . . . .	64
5.6	Apparatus for performing back-alignment of the spectrograph. . . . .	66
5.7	Laser turning mirror and entrance window. . . . .	69
5.8	Collection lens and baffled exit tube. . . . .	71
5.9	Timing diagram for laser measurements. . . . .	73
5.10	Diagram illustrating the manner in which iCCD data is recorded and stored. Each laser shot produces a 2-D array the size of the binned detector face containing the number of counts recorded at each super-pixel during the acquisition. . . . .	74
5.11	Simulated example of stray light measured at the detector. The light is broadened by the instrument function but is still relatively narrow and centered at the laser wavelength. . . . .	78
5.12	Simulated example of stray light and Rayleigh scatter measured at the detector. The Rayleigh scatter is also slightly broadened and is centered at the laser wavelength. . . . .	79
5.13	Simulated example of all the components of the signal measured at the detector. This figure is for illustrative purposes and the spectrum components are not to scale. . . . .	80
5.14	Example of the total scattered spectrum measured at the detector. . . . .	82

5.15	Sample total spectrum zoomed in to display the Thomson and emission components. . . . .	83
6.1	Internal Geometry of a Modified Spex Triple-Mate Spectrograph. . . . .	88
6.2	Geometry of the probing beam and scattering solid angle. . . . .	91
6.3	Top view of the beam path and scattering volume. The dark green dot indicates the laser focus and the lighter green circle represents the beam diameter approximately 0.3 m from the focus (above and below). . . . .	92
6.4	Effect of angular alignment on the detected scattering signal. . . . .	94
6.5	Acquisition of the total spectrum for a single laser pulse. . . . .	98
6.6	Sample corrected spectrum as determined by pulse accumulation over 27,000 acquisitions. Thruster conditions were 350 V discharge and 40 SCCM mass flow rate (xenon). . . . .	100
6.7	Sample corrected spectrum at 350 V 40 SCCM zoomed in to the region of interest. . . . .	101
6.8	Histogram of the number of counts detected at a super-pixel during emission spectrum acquisition with an exposure time of 20 ns. This figure demonstrates that most acquisitions contain only read noise centered on the mean of the noise $\mu_N$ , which is approximately 85 for this data set. . . . .	110
6.9	Histogram of emission data after being shifted by $\mu_N$ and divided by $\beta$ . . . . .	111



6.10 Histogram of fully processed emission data, zoomed in to clearly display the non-zero bins. The value of $\hat{\mu}$ determined by maximum likelihood estimation is 0.0014. . . . .	112
6.11 Total spectrum determined by the MLE method. Thruster conditions: 350 V, 40 SCCM anode mass flow. . . . .	115
6.12 Total spectrum determined by the MLE method, zoomed-in to clearly show the plasma emission lines. Thruster conditions: 350 V, 40 SCCM anode mass flow. . . . .	116
6.13 Emission spectrum determined by the MLE method. Thruster conditions: 350 V, 40 SCCM anode mass flow. . . . .	117
6.14 Stray light spectrum determined by the MLE method. Data acquisition was performed with the thruster off prior to the test. . . . .	118
6.15 Corrected spectrum determined by the MLE method (emission and stray spectra subtracted from the total). . . . .	119
6.16 Corrected spectrum determined by the MLE method (emission and stray spectra subtracted from the total), zoomed-in to show net-negative values. . . . .	120
6.17 Measured instrument function of the Spex 1877C-AG used in this work.) . . . .	121
6.18 Corrected Thomson scattering spectrum as determined using the maximum likelihood estimation technique. Thruster was operating at 300 V 40 SCCM, and the Gaussian fit indicates an electron temperature of 9.6 eV and density of $7.1 \times 10^{17} \text{ m}^{-3}$ . . . . .	122

7.1	Example of a low-signal line and the corresponding fit using the thresholding method. . . . .	131
7.2	Second example of a low-signal line and the corresponding fit using the thresholding method. Thruster conditions were 250 V discharge and 60 SCCM mass flow rate. . . . .	133
7.3	Example of a low-signal line as processed by the MLE method. Thruster conditions were 300 V discharge and 60 SCCM mass flow rate. . . . .	135
7.4	Example of a good line as determined by the MLE method. Thruster conditions were 300 V discharge and 40 SCCM mass flow rate. . . . .	136
7.5	Comparison of electron temperature measurements vs. mass flow rate at a fixed discharge voltage of 350 V. . . . .	139
7.6	Comparison of electron temperature measurements vs. discharge voltage at a fixed mass flow rate of 60 SCCM. . . . .	140
7.7	Comparison of plasma number density measurements vs. mass flow rate at a fixed discharge voltage of 350 V. . . . .	146
7.8	Comparison of plasma number density measurements vs. discharge voltage at a fixed mass flow rate of 60 SCCM. . . . .	147
7.9	Histogram of the number of counts detected at a super-pixel with the spectrograph entrance slit closed over 27,000 acquisitions with an exposure time of 20 ns. These counts are purely due to noise and possess a mean of 85 counts and a standard deviation of 4.5 counts. . . . .	150

7.10 Plot of the curve fit to a Thomson spectrum, including 95 percent confidence intervals. Thruster operating at 300 V discharge and 40 SCCM mass flow rate. . . . .	153
7.11 Plot of the curve fit to a Thomson spectrum, including 95 percent confidence intervals. Thruster operating at 350 V discharge and 40 SCCM mass flow rate. . . . .	154
7.12 First Langmuir probe trace taken at 300 V discharge and 40 SCCM mass flow rate. The plasma seems to be jumping between two distinct operational states. . . . .	159
7.13 Sample Thomson spectrum measured at 300 V discharge and 40 SCCM mass flow rate. The Gaussian shape of the trace is clearly visible. . . . .	160
7.14 Sample Thomson spectrum measured at 400 V discharge and 60 SCCM mass flow rate. This trace is not fit well by a Gaussian curve. . . . .	161
7.15 Second sample Thomson spectrum measured at 400 V discharge and 60 SCCM mass flow rate. This trace is fit reasonably well by a Gaussian curve, but has very low amplitude. . . . .	162
7.16 First Langmuir probe trace taken at 400 V discharge and 60 SCCM mass flow rate. . . . .	163
7.17 Second Langmuir probe trace taken at 400 V discharge and 60 SCCM mass flow rate. . . . .	164

8.1	Sample scattering configuration with the Hall thruster in a small spool-piece. The laser beam is delivered from above (not shown). . . . .	176
8.2	Sample scattering configuration with the Hall thruster in a small spool-piece. The beam can be passed through the thruster body where the wall has been removed. . . . .	177
8.3	Schematic of measurement geometry where the laser beam passes through the thruster. Downstream optics collect the scattered photons. . . . .	178
8.4	Schematic of measurement geometry where the laser beam passes through the thruster. Slots in the thruster body allow internal measurements of electron temperature and density. . . . .	179
8.5	Schematic of measurement geometry where the laser beam passes through the thruster. Fiber optics embedded in the thruster wall can measure internal electron properties. . . . .	180
A.1	First Langmuir probe trace taken at 300 V discharge and 40 SCCM mass flow rate. . . . .	200
A.2	Second Langmuir probe trace taken at 300 V discharge and 40 SCCM mass flow rate. . . . .	200
A.3	First Langmuir probe trace taken at 350 V discharge and 60 SCCM mass flow rate. . . . .	201
A.4	Second Langmuir probe trace taken at 350 V discharge and 60 SCCM mass flow rate. . . . .	201

A.5	First Langmuir probe trace taken at 350 V discharge and 50 SCCM mass flow rate. . . . .	202
A.6	Second Langmuir probe trace taken at 350 V discharge and 50 SCCM mass flow rate. . . . .	202
A.7	First Langmuir probe trace taken at 400 V discharge and 40 SCCM mass flow rate. . . . .	203
A.8	Second Langmuir probe trace taken at 400 V discharge and 40 SCCM mass flow rate. . . . .	203
A.9	First Langmuir probe trace taken at 300 V discharge and 50 SCCM mass flow rate. . . . .	204
A.10	Second Langmuir probe trace taken at 300 V discharge and 50 SCCM mass flow rate. . . . .	204
A.11	First Langmuir probe trace taken at 350 V discharge and 40 SCCM mass flow rate. . . . .	205
A.12	Second Langmuir probe trace taken at 350 V discharge and 40 SCCM mass flow rate. . . . .	205
A.13	First Langmuir probe trace taken at 400 V discharge and 60 SCCM mass flow rate. . . . .	206
A.14	Second Langmuir probe trace taken at 400 V discharge and 60 SCCM mass flow rate. . . . .	206

A.15 First Langmuir probe trace taken at 400 V discharge and 50 SCCM mass	
flow rate. . . . .	207
A.16 Second Langmuir probe trace taken at 400 V discharge and 50 SCCM mass	
flow rate. . . . .	207
A.17 First Langmuir probe trace taken at 300 V discharge and 60 SCCM mass	
flow rate. . . . .	208
A.18 Second Langmuir probe trace taken at 300 V discharge and 60 SCCM mass	
flow rate. . . . .	208
A.19 First Langmuir probe trace taken at 350 V discharge and 80 SCCM mass	
flow rate. . . . .	209
A.20 Second Langmuir probe trace taken at 350 V discharge and 80 SCCM mass	
flow rate. . . . .	209
A.21 First Langmuir probe trace taken at 450 V discharge and 60 SCCM mass	
flow rate. . . . .	210
A.22 Second Langmuir probe trace taken at 450 V discharge and 60 SCCM mass	
flow rate. . . . .	210
A.23 First Langmuir probe trace taken at 350 V discharge and 70 SCCM mass	
flow rate. . . . .	211
A.24 Second Langmuir probe trace taken at 350 V discharge and 70 SCCM mass	
flow rate. . . . .	211

A.25 First Langmuir probe trace taken at 250 V discharge and 60 SCCM mass flow rate. . . . .	212
A.26 Second Langmuir probe trace taken at 250 V discharge and 60 SCCM mass flow rate. . . . .	212
B.1 Graphical depiction of the data folding operation. . . . .	215
B.2 Emission spectrum calculated at 300 V 40 SCCM after folding the data. Note that due to the folding transform emission lines cover most of the spectrum. . . . .	216
B.3 Corrected spectrum at 300 V 40 SCCM after folding the data. Strong subtraction noise is present from the emission lines in the spectral region of interest. . . . .	216

# List of Tables

7.1	Test Matrix with Measurement Order . . . . .	127
7.2	Discharge current (A) for each operating condition. . . . .	127
7.3	Magnet current (A) for each operating condition. . . . .	127
7.4	Background pressure ( $\times 10^{-5}$ Torr) for each operating condition. . . . .	128
7.5	Electron temperature in eV as measured by electrostatic double probe. . .	130
7.6	Raw electron temperature in eV as determined using the thresholding method. . . . .	131
7.7	Corrected electron temperature in eV as determined using the thresholding method. The number of lines that were removed (if any) are in parentheses.	132
7.8	Raw electron temperature in eV as determined using the MLE method. . .	134
7.9	Corrected electron temperature in eV as determined using the MLE method. The number of lines that were removed (if any) are in parentheses.	135
7.10	Electron number density ( $\times 10^{18} \text{ m}^{-3}$ ) as measured by electrostatic double probe. . . . .	142
7.11	Raw electron number density ( $\times 10^{18} \text{ m}^{-3}$ ) as determined by the thresholding method. . . . .	143



7.12	Corrected electron number density ( $\times 10^{18} \text{ m}^{-3}$ ) as determined by the thresholding method. The number of lines that were removed (if any) are in parentheses. . . . .	144
7.13	Raw electron number density ( $\times 10^{17} \text{ m}^{-3}$ ) as determined by the MLE method. . . . .	145
7.14	Corrected electron number density ( $\times 10^{17} \text{ m}^{-3}$ ) as determined by the MLE method. The number of lines that were removed (if any) are in parentheses.	145

## Acknowledgments

A wise man once told me that getting a PhD is like banging your head against a wall repeatedly: you keep doing it because it feels so good when you stop. That wise man was my advisor Dr. Brad King, and several years later I know exactly what he meant. With the finish line before me I would like to take this opportunity to thank all of the people who have helped me down this long road.

I'll start by saying thank you to Brad King and the members of my committee. What initially attracted me to electric propulsion was Brad's enthusiasm and attitude toward learning, research, engineering, and innovation. People often joke that "can't" isn't in their vocabulary, but in Brad's case I think it really is true. He is always willing to tackle the hard problems and always has ideas for where to go next. The years I have spent in the ISP lab under his direction have been extremely memorable, and no where else in the world would I have had the opportunity to work on and be around so many unique projects. The other members of my committee, Dr. Yevgeny Raitses, Dr. Seong-Young Lee, and Dr. Jeff Allen have also had a great hand in my success. Dr. Raitses' expertise in electric propulsion research and his willingness to share his knowledge have been a huge asset. Whenever I see his work I am struck by its quality, originality, and completeness. Dr. Lee has been generous with his time, expertise, and especially equipment, without which this work would have been impossible. You have my eternal thanks for the use of your equipment and your helpful suggestions. Dr. Allen and I met when I was working for him as a TA my first semester of grad school, and since that time his enthusiasm, feedback, and support have helped me throughout this process.

Research is never free, and I would like to thank the United States Air Force Research Laboratory (AFRL) and the Michigan/Air Force Center for Excellence in Electric Propulsion (MACEEP) for their support of this project. I would like to specifically thank Dr. William Hargus for providing the spectrograph used in this work.

Next on the docket is the rest of the ISP lab, past and present. The first day I set foot in the lab as an undergraduate Alex and Dean talked me into skipping class and going to McDonald's to talk about electric propulsion. I would like to thank them and the rest of the old guard (Jason, Emily, Makela, and Jerry) for sharing their knowledge and making me a part of the lab. Of the old guard the one person I worked with extensively was Jason Makela. I would like to thank you Jason for teaching me how to make anything I ever needed out of uni-strut, fusion tape, and scrap metal. It was also great starting a business together and learning all we never wanted to know about product support. Carrie started

about the same time I did, but has since departed for the desert. Good luck with the plasma cannon, and watch out for snakes! This brings me to the new guard, Mark, Kurt, and EJ. It has been great sharing a lab with you for the past few years and I appreciate all the help you have given me. Mark has leant his LabView expertise and created awesome figures for me, EJ has spent 40-hour tests with me in the lab and helped debug my code, and Kurt has always been ready to help with anything, be it bringing me food during a long test or sitting up late at night to make sure I don't shoot my eye out with the laser. Thanks again to all of you.

Though not technically part of the ISP lab, I owe a huge debt of gratitude to master machinist and TIG-ninja Marty Toth. He accepted my abysmal drawings and could always work with me to turn whatever I had in my head into exactly what I needed. This usually meant something better than what I originally had in mind. You're a great friend, and I have thoroughly enjoyed hunting, fishing, cruising the trails, and even accidentally welding my wedding ring to my truck exhaust with your MIG welder (with my finger still in it).

None of this would have been possible without the help of my family. Since birth my mother and father have gone out of their way to give me every opportunity to succeed in life, and for that I am incredibly thankful. My sister Nicole, brother Ryan, and brother-in-law Delyan are also some of my biggest supporters and I would like to thank them for believing in me. One year into graduate school I extended my family by marrying a local, and I am one of the lucky few who is blessed with great in-laws. My mother- and father-in-law treat me like a true son, and Nate is a second not-so-little brother to me. I want to thank you all for being part of my life.

Most importantly, I want to thank my wife Emily. She has spent the last 4 years working midnights at a job that she hates so I could pursue my dream of becoming a research scientist. Her love and support has kept me sane through this process, and for that I cannot thank her enough.

Rob Washeleski  
*September 2012*

## Abstract

Hall-effect thrusters (HETs) are compact electric propulsion devices with high specific impulse used for a variety of space propulsion applications. HET technology is well developed but the electron properties in the discharge are not completely understood, mainly due to the difficulty involved in performing accurate measurements in the discharge. Measurements of electron temperature and density have been performed using electrostatic probes, but presence of the probes can significantly disrupt thruster operation, and thus alter the electron temperature and density. While fast-probe studies have expanded understanding of HET discharges, a non-invasive method of measuring the electron temperature and density in the plasma is highly desirable.

An alternative to electrostatic probes is a non-perturbing laser diagnostic technique that measures Thomson scattering from the plasma. Thomson scattering is the process by which photons are elastically scattered from the free electrons in a plasma. Since the electrons have thermal energy their motion causes a Doppler shift in the scattered photons that is proportional to their velocity. Like electrostatic probes, laser Thomson scattering (LTS) can be used to determine the temperature and density of free electrons in the plasma. Since Thomson scattering measures the electron velocity distribution function directly no assumptions of the plasma conditions are required, allowing accurate measurements in anisotropic and non-Maxwellian plasmas. LTS requires a complicated measurement apparatus, but has the potential to provide accurate, non-perturbing measurements of electron temperature and density in HET discharges.

In order to assess the feasibility of LTS diagnostics on HETs non-invasive measurements of electron temperature and density in the near-field plume of a Hall thruster were performed using a custom built laser Thomson scattering diagnostic. Laser measurements were processed using a maximum likelihood estimation method and results were compared to conventional electrostatic double probe measurements performed at the same thruster conditions. Electron temperature was found to range from approximately 1 – 40 eV and density ranged from approximately  $1.0 \times 10^{17} \text{ m}^{-3}$  to  $1.3 \times 10^{18} \text{ m}^{-3}$  over discharge voltages from 250 to 450 V and mass flow rates of 40 to 80 SCCM using xenon propellant.



# **Chapter 1**

## **Introduction**

### **1.1 Measurement of Electron Properties in Hall-effect Thrusters**

Hall-effect thrusters (or simply Hall thrusters) are compact electric space propulsion devices with long life and high specific impulse that are used on a variety of satellites for station keeping and orbit transfer manoeuvres [1]. Although Hall thrusters produce thrust by accelerating a beam of ionized propellant in crossed electric and magnetic fields, some of the most important processes in the discharge are governed by electron interactions. Electrons trapped in the crossed-field region are responsible for efficient ionization of the propellant gas. Impacts with propellant atoms allow the electrons to move across the

magnetic field towards the anode, contributing to cross-field mobility in the discharge channel [2]. Electrons are also constantly interacting with the walls of the discharge channel, depositing energy through collisions and producing cold secondary electrons that affect the potential structure near the channel walls [3]. The probabilities of these interactions and the nature of their products is strongly tied to the electron temperature and density in the plasma, and detailed knowledge of these parameters is important for the development of the next generation of Hall thrusters and for validation of numerical plasma simulations of bounded Hall-effect discharges in general.

Hall thruster technology is well developed but the electron properties in the discharge are not completely understood, mainly due to the difficulty involved in performing accurate measurements in the near-field plume and inside the discharge channel itself. Researchers have performed probe measurements in the near-field plume and discharge channel using fast-positioning stages [4–6], but fast-probe measurement methods have some significant disadvantages. Probes in close proximity to the thruster exit plane can significantly disrupt thruster operation, and thus alter the electron temperature and density. Another problem is that most probe data analysis techniques assume that the plasma is isotropic and Maxwellian, which may not be true due to the strong magnetic fields present near the thruster exit plane. While fast-probe studies have expanded our understanding of the temperature and density in Hall thruster discharges, a non-invasive method of measuring the electron temperature and density in the plasma is highly desirable.

Lasers have been used to measure plasma properties since shortly after they were developed in practical form in the 1960s [7]. An alternative to electrostatic probes is a non-perturbing laser diagnostic technique that measures Thomson scattering from the plasma. Thomson scattering is the process by which photons are elastically scattered from the free electrons in a plasma. Since the electrons have thermal energy their motion causes a Doppler shift in the scattered photons that is proportional to their velocity along the scattering vector, the direction of which is determined by the incident laser beam and the location of the collection optics. Like electrostatic probes, laser Thomson scattering (LTS) can be used to determine the temperature and density of free electrons in the plasma. Since Thomson scattering actually measures the electron velocity distribution function no assumptions of the plasma conditions are required, allowing accurate measurements in anisotropic and non-Maxwellian plasmas. Thomson scattering has some excellent advantages over electrostatic probes, but the scattered signal can be difficult to measure for the plasma conditions typical of Hall thrusters. Performing LTS requires a complicated measurement apparatus composed of expensive components, and establishing accurately aligned optical access to the plasma can be difficult. If these experimental difficulties can be overcome LTS has the potential to provide accurate, non-perturbing measurements of electron temperature and density that are currently unavailable to researchers in the field.

Electron properties are most important inside the discharge channel and near the exit plane where electron impact ionization, electron heating, and electron-wall collisions are taking place. While non-invasive laser measurements of electron temperature and density



in this region is the ultimate goal, performing laser measurements here requires significant modification of the thruster body and greatly complicates detection of the scattered signal. As a first step towards a complete laser measurements of electron temperature and density internal to a Hall thruster, this work will focus on measurements in the near-field plume where beam access is possible without modifying the thruster and signal detection is simplified due to lower stray light levels.

## **1.2 Aim and Scope**

The goal of this work was to perform both electrostatic probe and laser Thomson scattering measurements in the near-field plume of a Hall thruster in order to determine the feasibility of laser Thomson scattering as a diagnostic for space propulsion devices. A conventional electrostatic double probe was used to perform measurements of electron temperature and density for a variety of thruster operating conditions. A laser measurement apparatus was developed and used to measure electron temperature and density at the same operating conditions as the probe. The results of the probe and laser measurements were compared in order to assess Thomson scattering measurements performed in the plume of a Hall thruster.

Due to the small scattering signal produced by the relatively low electron density in the thruster plume laser measurements at a single operating condition took approximately two hours to complete. Because of the long measurement time and the use of a fixed scattering

volume all measurements were performed at a single location in the thruster plume for each operating condition. While this results in limited information about the plume properties, it is the first known application of laser Thomson scattering to a Hall thruster plasma.

Due to the difficulty of performing the laser measurements, this work was limited to comparing LTS measurements to electrostatic double probe measurements at a single location in the plume. Spatial mapping of the electron temperature and density in the plume, though valuable, was beyond the scope of this work. The discharge voltage and mass flow rate was varied over a wide range of operating parameters for the purpose of producing different plasma conditions, but mapping of thruster performance was also beyond the scope of this work. Since laser measurements inside the discharge channel were not possible, electrostatic probe measurements were limited to the near-field plume measurement location exclusively.

## **1.3 Structure**

Chapter 2 serves as a brief introduction to laser Thomson scattering research that has been performed over the last 60 years. The physics of laser scattering from plasmas is covered in detail in Chapter 3, and the limitations of such measurements are specified. Chapter 4 explains the operating principles of electrostatic probes and covers the details of their implementation in this work. Chapter 5 provides comprehensive coverage of the facilities and equipment involved in this work, along with detailed measurement

procedures. A discussion of Thomson scattering probability, maximum likelihood estimation, and the data processing algorithms used in this work are the subject of Chapter 6. Chapter 7 contains the results of both laser Thomson scattering and probe measurements along with a comparison of the various data reduction techniques. Finally, Chapter 8 discusses the conclusions that can be drawn from this work and provides suggestions for future research in this field.

## **Chapter 2**

# **Background and Review of Prior Research**

### **2.1 Introduction**

This chapter serves as a review of the material required to put the research of this work in context. A brief description of Hall-effect thruster operation and application is provided, along with a summary of the techniques that have been used to study the plasma properties in Hall-effect discharges. Some basic descriptions of laser diagnostic techniques are then discussed, with an emphasis on the advantages and disadvantages of laser methods compared to traditional diagnostics. The chapter concludes with a discussion of the history of laser Thomson scattering, including the plasma regimes where it has been used and the

data processing techniques that have been employed to reduce the raw scattering data.

## 2.2 Hall Thrusters

Hall thrusters are one of many types of thrusters that are members of the electric propulsion family, which is comprised of devices that produce thrust by either electrically heating propellant or applying electric and magnetic body forces to accelerate the propellant [8]. Electric propulsion devices generate exhaust velocities that are much higher than traditional chemical rockets, providing higher specific impulse and better utilization of propellant mass. Hall thrusters were born from work on magnetrons and cross-field sources during the 1960's [9], and can be divided into two categories. The first category is comprised of thrusters that do not have electrically conductive channel walls, and are referred to as stationary plasma thrusters (or SPTs). The second category contains thruster designs that have conductive channel walls, and are known as thrusters with anode layers (or TALs). For the experiments described in this work an SPT-type thruster was used.

A brief description of Hall thruster operation will be presented: more detailed descriptions can be found elsewhere [4, 10–13]. The defining characteristic of a Hall thruster is the closed electron drift current (known as the Hall current). A detailed representation of an Hall thruster can be seen in Figure 2.1. This drift is contained within a boron nitride annulus called a discharge channel, and is established by an axial electric field and a radial magnetic field. The anode is located in the back of the discharge channel

and serves as a gas distributor for the neutral propellant gas. A bias ranging from 200-1000 V is applied to the anode, providing the axial electric field needed to repel the ions in the discharge. Electromagnet coils and permeable iron front- and back-plates create a radial magnetic field near the discharge channel exit plane. Most thrusters use inert noble gases such as xenon and krypton as propellant, which is ionized and accelerated in the crossed electric and magnetic fields. Electrons are provided by an external thermionic cathode, some of which are attracted to the anode. The magnetic field is sized such that these electrons are magnetized, which greatly impedes electron transport through the channel towards the anode. These trapped electrons experience an  $E \times B$  drift in addition to cyclotron motion due to the magnetic field, and swirl in an azimuthal drift around the discharge channel. Neutral gas from the anode diffuses toward the channel exit and is ionized by electron impacts, and since the ion Larmour radius is much larger than the characteristic dimensions of the thruster, the newly born ions are not significantly magnetized. The trapped electrons allow the existence of a strong gradient in the plasma potential, and ions “roll” down this potential and are accelerated out of the channel, thereby generating thrust. Since the thrust is generated through electrostatic acceleration of ions in a quasi-neutral plasma [3] Hall thrusters are free from space charge effects [14].

The momentum gained by equally charged particles per unit time is identical in an electromagnetic field, but since electrons have very low mass compared to the ions, their velocity (and therefore energy) gain is much greater than the ions [15]. Propellant gas in a Hall thruster is ionized primarily by electron impact since energy exchange between free

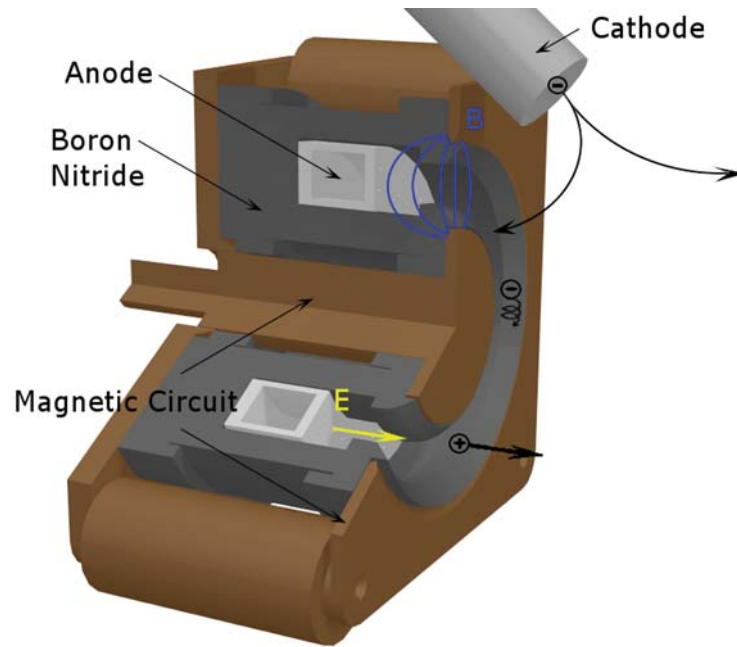


**Figure 2.1:** Cross-section of a typical Hall-effect thruster. ©2012 M. Hopkins and R. Washeleski.

and bound electrons is very efficient (due to their equal masses). Impact ionization depends strongly on the electron density and temperature which makes it important to know the electron properties in the plasma. Electron temperature and density (and their fluctuations) are also coupled to cross-field mobility which determines the potential structure in the plasma [2].

Since electron processes dominate Hall thruster discharges, two of the most important properties to measure in a plasma are the temperature and density of the free electrons. This work will focus on measurements of these electron properties exclusively. Many techniques of measuring the electron temperature and density have been implemented, and diagnostic techniques that have been applied in the past will be discussed in the following section.

## 2.3 Current Electron Diagnostic Techniques

Several methods have been used to experimentally study electron temperature and density in various regions of Hall thruster discharges over the years, but the focus of this discussion will be diagnostics applied in the near-field plume. The first diagnostic tool developed was the Langmuir probe, developed by Nobel Laureate Irving Langmuir in the 1920's [16]. Chapter 4 contains a detailed discussion of Langmuir probes and their operational characteristics, but for now consider a probe to be simply a piece of metal wire that is inserted into the plasma. By connecting this wire to a power supply and monitoring the collected current as a function of voltage one can determine the electron temperature, density, floating potential, and plasma potential. Langmuir probes are simple to use and provide local measurements of plasma properties, but there are some major drawbacks. Presence of the probe in the discharge can disrupt the plasma, and the size of the probe limits the spatial resolution of the measurement. When attempting measurements near the discharge channel exit the heat and particle fluxes to the probe can be enormous, making near-field measurements problematic due to the destruction of the probe by the plasma. In addition to these physical considerations most probe analysis techniques assume the plasma electrons have a Maxwellian distribution, which is often a poor assumption.

In an attempt to solve the problem of probe survival in the near-field plume, researchers have mounted probes on fast motion stages that can move probes into position at speeds



in excess of 3 m/s. Measurements are then quickly taken and the probe is removed, with residence times in the plasma on the order of tens of milliseconds. These types of measurements have been performed with double Langmuir probes [4, 6], and with combinations of cold and emissive probes [3]. This greatly reduces disturbances in the plasma, but does not completely eliminate them [17]. Measurements of electron temperature and density using optical techniques have the potential to be applied while producing virtually no perturbations, and are highly desirable for this reason.

Optical measurements of electron properties have been made using the method of optical emission spectroscopy (OES). When performing OES the emission spectrum of the plasma is recorded over a range of wavelengths that contain multiple emission lines of the propellant gas. The line intensities in the plasma emission spectrum are directly related to the density of the excited heavy-particle states, but models are required to relate these intensities to the electron density and temperature [18]. The indirect nature of this technique is one of its major drawbacks. Emission from ions and neutrals are measured directly along a chord in the plasma and a model is needed to make an estimate of what the electron properties might be, subject to certain assumptions required to make the problem tractable. A schematic depicting this process can be seen in Figure 2.2. It is clear that the results of this method will have a strong dependence on which model one chooses to use for the plasma. In addition to the indirectness of OES, there is also a need for Abel inversion to obtain spatially resolved properties since the emission measurement is line-integrated through the plasma. Both choice of model and need for Abel inversion can be a serious

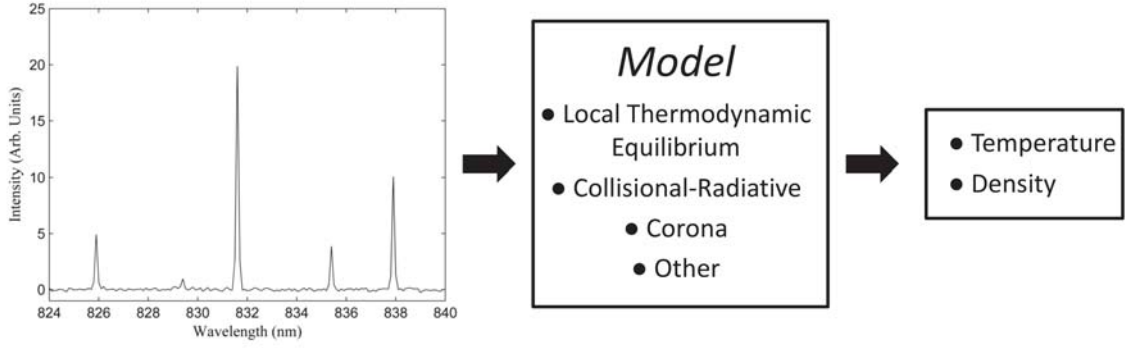


**Figure 2.2:** Process of determining electron temperature and density using optical emission spectroscopy.

concern when one is interested in accurate absolute measurements of electron temperature and density in the plasma [19].

Several models have been employed in the past, ranging from simple to exceptionally complicated. The most simple models assume local thermal equilibrium (LTE), which is satisfied if all species in the discharge follow the Boltzmann distribution. Applying the LTE assumption to a plasma is generally valid if the following condition is satisfied [18]:

$$n_e \gg 10^{19} \left( \frac{T}{e} \right)^{1/2} \left( \frac{\Delta E}{e} \right)^3 m^{-3} \quad (2.1)$$

where  $n_e$  is the electron number density,  $e$  is the fundamental charge, and  $T/e$  and  $\Delta E/e$  are in units of eV. This criterion is not usually satisfied in the near-field plume of Hall thrusters, so other emission models must be used, such as a collisional-radiative model or a corona model [20]. Plasma collisional-radiative models have been used to interpret

almost all line intensity measurements performed on Hall thrusters [21], with reasonable agreement with probe measurements in similar conditions [22].

While electrostatic probe and line emission measurements have provided insight into the plasma conditions in the near-field plume, a method of measuring the electron temperature and density that is direct, non-invasive, and spatially resolved is still needed in order to fully understand the electron dynamics in the discharge. Recent advances in pulsed laser development and photon detection technology may have made such a diagnostic possible for Hall thruster plasmas by measuring scattering of laser light from free electrons in the plasma, a process called Thomson scattering. The next section will discuss the history of Thomson scattering and the plasma conditions in which LTS measurements have been performed.

## **2.4 Laser Thomson Scattering Review**

The process of electromagnetic radiation being scattered from free electrons is named after J. J. Thomson, the Nobel Laureate credited with discovery of the electron. Physical and mathematical details of the scattering process will be discussed in Chapter 3. This section will provide a brief history of Thomson scattering diagnostics in order to put the contribution of this work into context.

### 2.4.1 Early Work

Although most Thomson scattering measurements have been performed using lasers, the earliest application of Thomson scattering took advantage of the large radar cross-section of the electron to make measurements of density versus altitude in the ionosphere [23]. The first laser Thomson scattering measurements were performed using a ruby laser on an electron beam [24]. Subsequent experiments were able to take advantage of the polarization of the scattered light to determine temperature and density in a thetatron [25] and a helium arc plasma [26], with the latter making use of a giant-pulse (Q-switched) laser. The proliferation of ruby lasers made Thomson scattering a widespread diagnostic tool in plasma physics [27], most notably in the fusion community.

### 2.4.2 Fusion Plasmas

Fusion plasmas have high electron density and temperature which produce a strong Thomson scattering signal. High temperatures produce a spectrally broad scattered signal easily distinguishable from the laser light and high density produces a strong signal that can easily be seen over background noise sources. Scattering measurements using a multi-channel system on the T-3 Tokamak in the U.S.S.R. produced measurements of electron temperature ranging from 100 eV to 1000 eV with densities of  $1\text{--}3 \times 10^{19} \text{ m}^{-3}$  [28]. Demonstration of the usefulness of incoherent LTS on the T-3 Tokamak was a huge milestone in Thomson scattering diagnostic development [20]. Since the late

1960's Thomson scattering with ruby lasers has been a staple of fusion research, with implementations ranging from the multi-channel TVTS system on the TFTR tokamak at Princeton University [29] to measurements in inertial confinement plasmas [30].

### 2.4.3 Extension to Cold Plasmas

In the mid 1980s Thomson scattering was extended to colder processing plasmas ( $T_e = 1\text{-}10\text{ eV}$ ) with moderate electron densities ( $10^{18} - 10^{21}\text{ m}^{-3}$ ). Performing Thomson scattering measurements in this domain has a different set of challenges compared to fusion and thetatron plasmas. Plasmas with high temperature and density have large amounts of line emission, Bremsstrahlung, and stray light present as noise sources. For cold plasmas Bremsstrahlung is typically negligible, and there is a lack of strong line emission at most relevant wavelengths. As a logical extension of fusion work, early measurements on cold plasmas continued to use ruby lasers. Examples of this are measurements on an inductively coupled plasma (ICP) [31, 32], measurements on a low-pressure plasma spray (LPPS) device [33], and the first LTS measurements of an electron cyclotron resonance (ECR) plasma [34].

Contemporary with this early work, Nd:YAG lasers with high pulse energy and high repetition rates were being developed along with visible-wavelength detectors with high sensitivity and low noise [35]. These lasers combine good power and pointing stability, low beam divergence, and good beam quality [20], and as a result frequency doubled

Nd:YAG lasers operating at 532 nm have become the dominant laser source for Thomson scattering measurements. Electron temperature and density in many devices have since been measured using Nd:YAG lasers, including expanding arc plasmas [36, 37], ECR discharges [38–40], and microwave plasma torches [41, 42].

Similar advances in detector technology have also aided the development of LTS. Until the late 1990s most LTS diagnostics on cold plasmas used photomultiplier tubes (PMTs) to detect the scattered Thomson signal. PMTs have excellent sensitivity and the ability to count single photons, but they also have the disadvantage of being able to detect only one wavelength of scattered light at a time, necessitating measurements at multiple wavelengths to reconstruct a full scattered spectrum. Such wavelength scanning can be exceptionally time consuming, especially when low electron density necessitates acquisition times of 30 minutes or more at each wavelength. The desire for shorter acquisition times led to the use of intensified charge-couple devices (iCCDs) to collect the entire scattered spectrum at once, greatly reducing acquisition times and potentially reducing the detection limit. In one experiment an iCCD was combined with a multi-pass cell and low-power/high rep-rate Nd:YAG laser, resulting in a detection limit of approximately  $10^{17} \text{ m}^{-3}$  for acquisition times of about 25 minutes [43].

The next major advance in Thomson scattering was the extension of the technique to small lamp plasmas, bringing a new set of challenges. Most of the processing plasmas investigated up to this point had fairly open geometries, with simple beam and collection

lens access. The compact nature of the lamp environment causes the stray light level to increase considerably from close proximity of the walls and from the scatter generated by the laser passing through glass walls very close to the collection lenses. For the low temperatures and densities characteristic of lamp plasmas the scattered signal is very close to the Rayleigh and stray light at the laser wavelength, and can be completely obscured. In order to deal with this high stray light level researchers developed atomic notch filters to make spectrally narrow band-stops centered at the laser wavelength using sodium vapor [44], iodine, and mercury [45], and rubidium [45–47]. Around the same time other research groups introduced physical band-stop filters into their spectrographs using metal plates to block the laser wavelength after dispersion [15, 48], commonly called “Rayleigh blocks”. These methods have since become widely applied when dealing with high levels of stray light and/or close measurement geometries.

#### **2.4.4 Application to Miniature Ion Thrusters**

Beginning in the late 2000’s Thomson scattering measurements have been taken inside the discharge chamber of a miniature microwave ion thruster [49]. A triple grating spectrograph and PMT were used for this work, and the data was processed using a photon counting method. Electron densities of approximately  $10^{18} \text{ m}^{-3}$  were measured, and electron temperature ranged from about 2-10 eV. These measurements were the first application of LTS to a space propulsion device.

## 2.5 Contribution of this Work

Thomson scattering has been a crucial plasma diagnostic for over 50 years, but has only recently been applied to a space propulsion device. The goal of the research reported in this document was to determine the suitability of LTS as a technique to measure electron density and electron velocity distribution function (EVDF) in the near-field plume of a Hall thruster. In order to make this assessment both LTS and probe measurements of electron density and EVDF/temperature were performed in the plume of a Hall thruster. The electron density and temperature in the near-field plume of a Hall thruster is near the detection limit reported in available contemporary literature and the geometry of Hall thruster experiments adds complications to signal detection that must be overcome. In order to determine the suitability of LTS for Hall thruster research a complete scattering system was designed and built to perform LTS on a 2-kW-class thruster.

After performing measurements with the Thomson scattering diagnostic it was found that the signal was right at or below the detection limit of the apparatus using established data processing techniques. In an attempt to extract meaningful information from the extremely weak scattered signal a new data processing technique based on maximum likelihood estimation was developed, and measurements with both the laser system and electrostatic probes were compared. The resulting data processing technique was able to determine electron temperature and density from the scattering data and may be capable



of lowering the detection limit, thus extending LTS measurements to a wider variety of plasmas.

# Chapter 3

## Laser Scattering from Plasma

### 3.1 Introduction

The scattering of laser light from a plasma can provide a great deal of information about the properties of the plasma. Scattering can occur from neutral gas particles, ions, dust and other impurity species, and from the free electrons in the plasma. Depending on the source of the scattering, information about the electron temperature, electron velocity distribution, electron density, and the heavy particle temperatures can be determined [15]. These properties can typically be measured with excellent spatial resolution and accuracy due to the high spatial and temporal coherence of laser light [20]. Laser diagnostic methods are also non-perturbing, which is a significant advantage over electrostatic probe methods. This chapter will give an overview of light scattering and laser-plasma interactions of

concern in this work.

There are many ways laser light can be scattered by particles in a plasma. The wavelength of the probing laser, particle size, and particle geometry all determine what type of scattering will occur. Each type of interaction relevant to plasma scattering will be covered briefly in the following sections.

## 3.2 Rayleigh Scattering

Rayleigh scattering is elastic scatter of photons from heavy particles (neutrals and ions) in a plasma. Because the interaction is elastic neither particle experiences a change in energy and the scattered light remains at the incident wavelength. This type of scattering occurs in the small size parameter regime,  $\zeta \ll 1$ , where:

$$\zeta = \frac{2\pi a}{\lambda} \quad (3.1)$$

is the size parameter, and  $a$  is the radius of the scatterer. The Hall thruster used in this work runs on xenon which has an atomic radius of approximately 200 pm, so this condition is readily satisfied. The heavy particles are typically not moving very quickly and the scattering is Doppler broadened by a very small amount [15].

For any type of scattering, the expression for the scattered light passing through a

volume of interest is given by [15]:

$$P_s = P_i \cdot n \cdot L_{det} \cdot \frac{d\sigma}{d\Omega} \cdot \Delta\Omega \quad (3.2)$$

where  $P_s$  and  $P_i$  are the scattered and incident powers (respectively),  $n$  is the number density of scatterers,  $L_{det}$  is the length along the beam from which scattering is being detected,  $\frac{d\sigma}{d\Omega}$  is the differential scattering cross-section for the process, and  $\Delta\Omega$  is the solid angle of detection. For Rayleigh scattering, the differential scattering cross-section is given by [50]:

$$\frac{d\sigma_R}{d\Omega} = \frac{\pi^2 \alpha^2}{\epsilon_0^2 \lambda^4} \cdot \sin^2 \phi \quad (3.3)$$

where  $\alpha$  is the polarisability of the medium,  $\lambda$  is the incident wavelength, and  $\phi$  is the angle between the electric field and the direction of scattering. Substituting parameters for the conditions in this work yields a differential cross-section for xenon gas under Rayleigh scattering of  $5.82 \times 10^{-32} \text{ m}^2$ .

Rayleigh scattering by atoms can in theory be used to determine the temperature and density of the heavy particles in the plasma, but in practice this is difficult. The broadening due to thermal motion is so small that most spectrometers can not spectrally resolve the Rayleigh line well enough to accurately determine the temperature. Density can be measured from the intensity of the Rayleigh line, but the presence of stray light at the laser wavelength can make the detection limit for density measurements higher than the heavy particle densities one is trying to measure. The main use of Rayleigh scatter in this work

is for calibration of absolute density measurements. Rayleigh calibration is described in detail in section [5.4.2](#).

### **3.3 Thomson Scattering**

Thomson scattering is scattering from free electrons in the plasma. This is the type of scattering that is of interest in this work since the properties that we want to measure are the free electron temperature and density. Thomson scattering is an elastic process, but the scattered light is Doppler broadened due to the motion of the electrons. Formulation of Thomson scattering can be done from either a quantum or classical approach, though this work will only cover the latter. The following subsections will cover the details of both individual scattering events and how these events manifest themselves in bulk plasma.

#### **3.3.1 Single Electron**

Classically speaking, Thomson scattering occurs because free electrons in the plasma are accelerated by the laser's oscillating electric field. Accelerated charges radiate energy, and this is what is measured as scattered light. To determine what happens to an electron

accelerated in the electric field of a laser, one must start with Maxwell's equations:

$$\begin{aligned}
\nabla \times \vec{E} &= -\frac{\partial \vec{B}}{\partial t} \\
\nabla \times \vec{B} &= \mu_0 \vec{J} + \mu_0 \epsilon_0 \frac{\partial \vec{E}}{\partial t} \\
\nabla \cdot \vec{E} &= \frac{\rho}{\epsilon_0} \\
\nabla \cdot \vec{B} &= 0
\end{aligned} \tag{3.4}$$

Taking the curl of the first equation, substituting the second equation, then rearranging gives:

$$\nabla \times (\nabla \times \vec{E}) + \mu_0 \epsilon_0 \frac{\partial^2 \vec{E}}{\partial t^2} = -\mu_0 \frac{\partial \vec{J}}{\partial t} \tag{3.5}$$

In order to determine the electric field produced by a single accelerated charge one must substitute the current density for a single charge,  $\vec{J} = q \cdot \vec{v}(t')$ , and solve the above equation [51]. The coordinate system used in the solution can be seen in Figure 3.1.

Detailed solutions to this problem can be found in Jackson [52] and Smith [53], the results of which will be summarized here. The complete solution given by Smith is:

$$\vec{E}(\vec{r}, t) = \frac{q}{4\pi\epsilon_0} \left[ \frac{\hat{R}_q - \vec{\beta}}{\gamma^2 R_q^2 (1 - \hat{R}_q \cdot \vec{\beta})^3} \right]_{ret} + \frac{q}{4\pi\epsilon_0 c^2} \left[ \frac{\hat{R}_q \times (\hat{R}_q - \vec{\beta}) \times \vec{a}}{R_q (1 - \hat{R}_q \cdot \vec{\beta})^3} \right]_{ret} \tag{3.6}$$

where  $\vec{\beta} \equiv \vec{v}/c$ ,  $\gamma \equiv \frac{1}{\sqrt{1-\beta^2}}$  is the Lorentz factor, and the subscript *ret* indicates that the fields are evaluated at the retarded time  $t_r = t - (R/c)$ . The expression for  $\vec{E}$  is

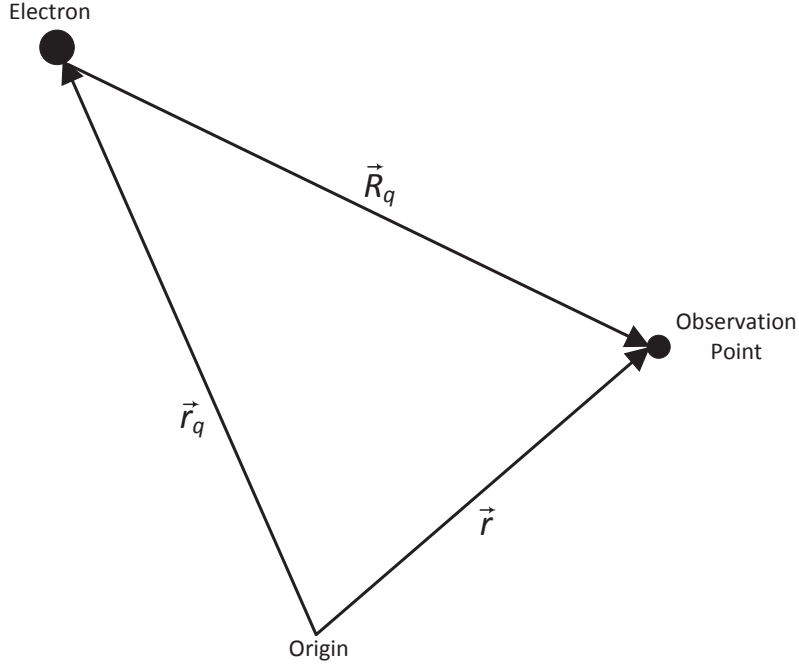


**Figure 3.1:** Solution Coordinates.  $R_q$  is the vector from the scattering electron to the observation point and  $\hat{R}_q$  is the unit vector with the same direction as  $R$ .

separated into two terms, one that arises from the velocity of the particle and one from its acceleration. For the plasma under consideration in this work the velocity of the electrons is much less than the speed of light, so it is permissible neglect the velocity term and make the approximations  $\gamma \approx 1$  and  $\vec{\beta} \ll 1$ . These assumptions reduces the previous equation for  $\vec{E}(\vec{r}, t)$  to:

$$\vec{E}(\vec{r}, t) = \frac{q}{4\pi\epsilon_0 c^2} \left[ \frac{\hat{R}_q \times (\hat{R}_q \times \vec{a})}{R_q} \right]_{ret}. \quad (3.7)$$

Likewise, the simplified expression for the magnetic field of the accelerated charge,  $\vec{B}(\vec{r}, t)$ ,

can be expressed as:

$$-\frac{\mu_0 q}{4\pi c} \left[ \frac{\hat{R}_q \times \vec{a}}{R_q} \right]_{ret}. \quad (3.8)$$

Now that the electric and magnetic fields are known, the radiated power can be determined. Using the definition of the Poynting vector,  $\vec{S}$ :

$$\vec{S} \equiv \frac{1}{\mu_0} \vec{E} \times \vec{B} \quad (3.9)$$

the scattered power per unit solid angle is given by [53]:

$$\frac{dP}{d\Omega} = \frac{q^2}{16\pi^2 \epsilon_0 c^3} \left[ |\hat{R}_q \times (\hat{R}_q \times \vec{a})|^2 \right]_{ret} \quad (3.10)$$

Introducing  $\theta$  as the angle between the acceleration vector and direction of scattering, the radiated power can be re-written as:

$$\frac{dP}{d\Omega} = \frac{q^2}{16\pi^2 \epsilon_0 c^3} [a^2 \sin^2 \Theta]_{ret} \quad (3.11)$$

which reveals the angular dependence of the scattering. The electric field of the linearly polarized laser can be written as:

$$\vec{E}_i = \hat{e} E_0 e^{i\vec{k}_i \cdot \vec{r} - i\omega_i t} \quad (3.12)$$

where  $\hat{e}$  is a normalized vector indicating the direction of polarization. For a linearly



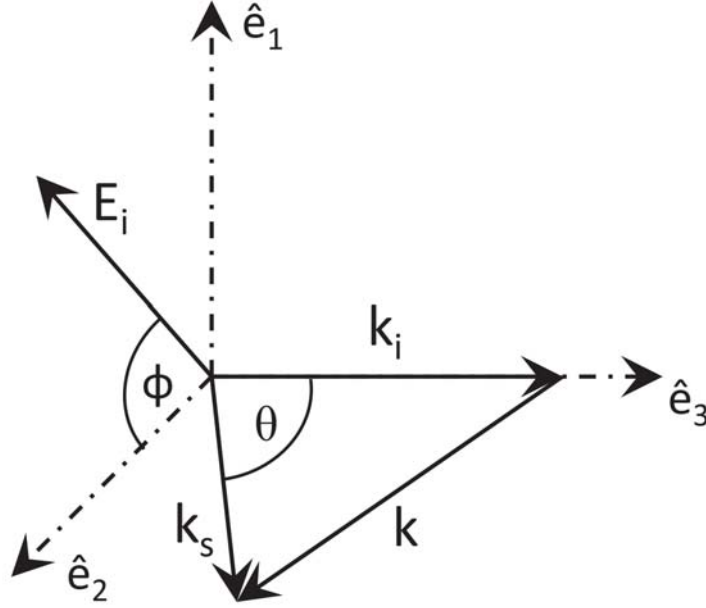


**Figure 3.2:** Vector Geometry for General Scattering

polarized electric field the geometric term  $\hat{R}_q \times (\hat{R}_q \times \hat{e})$  can be written as [51]:

$$\hat{R}_q \times (\hat{R}_q \times \hat{e}) = 1 - \sin^2 \theta \cos^2 \phi \quad (3.13)$$

The general coordinate geometry for this equation can be seen in Figure 3.2. For the scattering geometry in this work both  $\theta$  and  $\phi$  are 90 degrees, chosen intentionally to maximize the scattered signal in the direction of the collection optics and provide a good compromise between a large Doppler shift and signal to noise ratio (SNR). Although the Doppler shift is largest at 180 degrees [19], the scattered signal from a collection of electrons has a fixed area determined by the electron density. This means that larger scattering angles lead to a “flattened” spectrum with lower total amplitude at wavelengths

near the laser line where SNR is typically highest.

### 3.3.2 Scattering from Plasma

So far this discussion has been based on a mythical stationary electron that is briefly accelerated by an electric field, thus scattering the incident radiation outward with a known angular distribution similar to a radiating dipole. In reality a free electron in the plasma will be moving randomly with thermal motion, and it is precisely this thermal motion that we wish to measure. Depending on a particle's velocity the light scattered from an electron may be at a different wavelength than the incident light. This shift in frequency is due to Doppler shift from the electron's motion. There are actually two Doppler shifts that can occur, one due to the velocity component of the electron along the path of the laser beam and one due to the velocity component of the electron along the direction of observation. The Doppler shift is directly proportional to the velocity of the particle along the scattering vector  $\vec{k}$ , given by [15]:

$$\vec{k} = \vec{k}_s - \vec{k}_i \quad (3.14)$$

where  $\vec{k}_s$  is the vector component directed from the scattering volume towards the detector and  $\vec{k}_i$  is the vector component along the path of the laser beam. The scattering geometry for this work can be seen in Figure 3.3.

This total scattering vector can be used to define the total frequency shift due to the

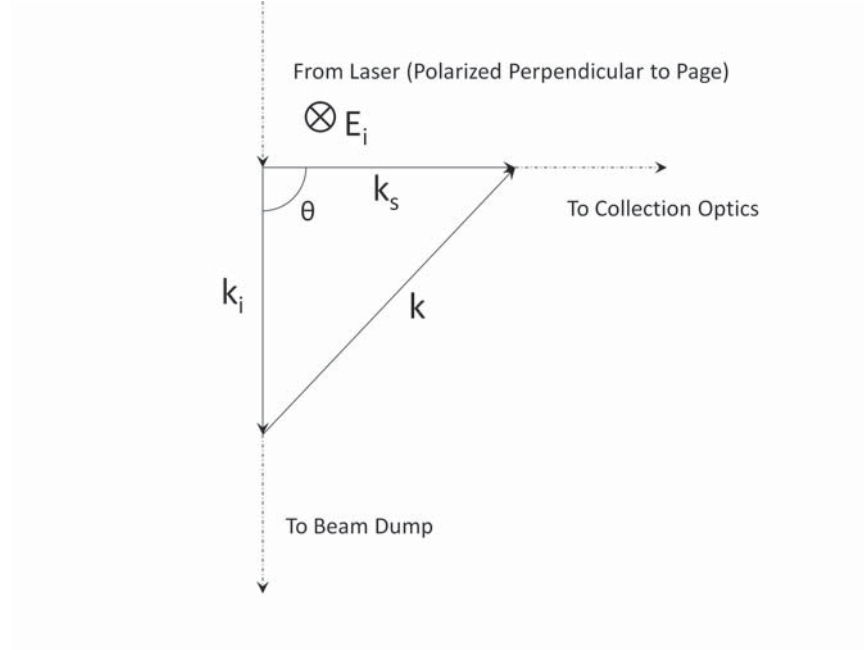


**Figure 3.3:** Scattering Geometry for MTU LTS Diagnostic

composite Doppler shift according to [51]:

$$\Delta\omega = \vec{k} \cdot \vec{v} \quad (3.15)$$

As can be deduced from Figure 3.3, the orientation of the laser beam, detection optics, and plasma source can all be adjusted to obtain measurements of the electron velocity distribution along specific directions in the plasma, which can be advantageous when attempting measurements in strong magnetic fields. The magnetic fields are relatively weak in the near-field plume of a Hall thruster and magnetic effects will not be considered. The LTS diagnostic can only measure the velocity distribution along a single direction in the plasma for a given measurement geometry, which is a significant drawback. Since other

directions in the plasma cannot be measured with the fixed scattering geometry used in this work an isotropic electron velocity distribution was assumed.

When calculating the scattered signal from a collection of electrons the phase of the scattering must be considered since it can have a drastic effect on the scattered spectrum. Depending on the laser wavelength, inter-particle spacing, and scattering angles, the scattering from individual electrons in the scattering volume can emit radiation with correlated phase. This coherence effect greatly changes the scattered spectrum and it is necessary to know whether the scattering system is operating in a coherent or incoherent manner. The scattering parameter is used to determine which regime the system is operating in, and is given by [15]:

$$\alpha \equiv \frac{1}{k\lambda_D} \approx \frac{1}{4\pi \sin(\theta/2)} \frac{\lambda_i}{\lambda_D} \quad (3.16)$$

where  $k$  is the scattering vector,  $\lambda_i$  is the incident laser wavelength, and  $\lambda_D$  is the Debye length. When the laser wavelength is short compared to the Debye length the scattering from electrons in the scattering volume is randomly distributed and the scattering is said to be incoherent [51]. This situation corresponds to values of  $\alpha \ll 1$ . For values of  $\alpha \approx 1$  and larger the scattering from electrons in the volume depends on the collective behaviour of the electrons and the phase is strongly correlated. For the plasma conditions and measurement geometry used for this work the scattering is incoherent. With  $\lambda_i = 532$  nm,  $\theta = 90$  degrees,  $T_e = 1 - 45$  eV, and  $n_e = 1 \times 10^{15} - 1 \times 10^{19} \text{ m}^{-3}$ , the value of  $\alpha$  ranges from 0.000036 - 0.0038, clearly in the incoherent scattering regime.

Having established that we are operating in the incoherent limit we can calculate the scattered power from a collection of electrons. We begin with an equation describing the scattered power for a population of electrons with a one dimensional velocity distribution in the  $\vec{k}$  direction,  $S_k(\Delta\omega)$ , given by [15]:

$$\frac{dP_s}{d\omega_s}d\omega_s = P_i n_e L_{det} \frac{d\sigma_T}{d\Omega} \Delta\Omega \cdot S_k(\Delta\omega) d\omega_s. \quad (3.17)$$

The spectral distribution function  $S_k(\Delta\omega)$  is normalized, and the shape of this function is directly proportional to the electron velocity distribution function along the scattering vector  $\vec{k}$ . In principal this allows direct measurement of the electron velocity distribution function, but for the plasma conditions in this work the scattered signal is so weak that some assumptions were necessary. The scattered spectra that were obtained had shapes that look approximately Gaussian, and even if there was some deviation from a Gaussian shape the SNR was too low to confirm said deviation. The plasma in the near-field plume was expected to be thermalized and a Maxwellian distribution was assumed for all calculations in the present work.

For an isotropic Maxwellian plasma the electron velocity distribution is the same along any arbitrary direction, and is equal to a one-dimensional Boltzmann distribution given by:

$$f_v(v_k) = \sqrt{\frac{m}{2\pi k_B T}} \exp \frac{-mv_k^2}{2k_B T} \quad (3.18)$$

This can be related to the shift in wavelength by comparing equation 3.18 to the expression for a one-dimensional normal distribution:

$$f(x; \mu, \sigma^2) = \frac{1}{\sigma\sqrt{2\pi}} \cdot \exp \frac{-(x - \mu)^2}{2\sigma^2} \quad (3.19)$$

Comparison of equations 3.18 and 3.19 show that  $\sigma = \sqrt{\frac{m}{k_B T}}$ . Equation 3.19 can be manipulated to determine the value of  $\Delta\lambda_{1/e}$  by setting the amplitude equal to  $\frac{1}{e}$  for an arbitrary value of  $f(x; \mu, \sigma^2)$ . Doing this one finds that  $\Delta\lambda_{1/e} = \sqrt{2\sigma^2}$ . After converting equation 3.17 from frequency to wavelength these values can be substituted to yield:

$$\frac{dP_s}{d\lambda_s} d\lambda_s = P_i n_e L_{det} \frac{d\sigma_T}{d\Omega} \Delta\Omega \cdot \frac{1}{\sqrt{\pi} \Delta\lambda_{1/e}} \exp \frac{-(\Delta\lambda)^2}{(\Delta\lambda_{1/e})^2} d\lambda_s \quad (3.20)$$

This this is the final expression for the incoherent scattering of laser light from a population of free electrons in a plasma. The parameter  $\Delta\lambda_{1/e}$  can be measured and converted to temperature via the following equation [15]:

$$T_e = \frac{m_e c^2}{8k_B \sin^2(\theta/2)} \cdot \left( \frac{\Delta\lambda_{1/e}}{\lambda_i} \right)^2 \quad (3.21)$$

## 3.4 Laser-Plasma Interaction

The powerful lasers required for Thomson scattering measurements can produce unwanted effects in the plasma in addition to the intended scattering. It is important to

understand these effects and ensure that the laser is not disrupting or otherwise perturbing the plasma. The following subsections discuss some of the problems that can arise from laser-plasma interaction.

### 3.4.1 Plasma Heating

The high energy density of a probing laser beam can cause localized heating of a plasma, thus altering the electron temperature. Plasma heating due to local absorption of photons through inverse Bremsstrahlung is discussed in detail by Evans and Katzenstein [27]. A formula estimating the change in electron temperature due to laser heating is given by Kunze [54] as:

$$\frac{\Delta W}{W} = 5.32 \times 10^{-7} \cdot \frac{nZ}{W^{3/2}} \cdot \lambda^3 \cdot \{1 - \exp\frac{-h\nu}{W}\} \cdot I_0 \cdot \Delta\tau \quad (3.22)$$

where  $n$  is the electron number density in  $cm^{-3}$ ,  $Z$  is the charge state of the ions,  $W$  is the temperature of the electrons in eV,  $\lambda$  is the incident wavelength in  $cm$ ,  $\nu$  is the laser frequency in Hertz,  $I_0$  is the laser intensity in  $W/cm^2$ , and  $\Delta\tau$  is the pulse duration of the laser in seconds. For the plasma investigated in this work the electron temperature ranges from about 5 - 15 eV with density of around  $1 \times 10^{18} m^{-3}$ . Using these values and the relevant laser parameters yields a fractional temperature increase of  $9.5 \times 10^{-8}$ , indicating that plasma heating by the beam is insignificant.

### 3.4.2 Photo-Ionization

Laser photons can also disturb the plasma by means of photo-ionization of neutral particles. This topic is discussed in great detail by Mainfray and Manus [55]. The first and second ionization energies of xenon are 12.13 eV and 20.98 eV, respectively. At 532 nm the energy of a single photon is only 2.331 eV, so direct photo-ionization of neutral atoms from the ground state does not occur. However, multiphoton ionization from the ground state can occur in addition to ionization of meta-stable xenon that is at an energy higher than the ground state. The number of ions produced by multiphoton events is described by the following formula [56]:

$$N_i \propto n_0 \sigma_N \Gamma^N \quad (3.23)$$

where  $N_i$  is the number of ions produced,  $\sigma_N$  is the cross section of the event,  $\Gamma^N$  is the photon flux, and  $N$  is the number of photons required for the process. The cross-sections for such events are theoretically small (and have not been accurately measured for metastable states at 532 nm), but the photon flux produced by sufficiently strong laser can cause such multiphoton events to occur.

Photo-ionization is not considered a significant perturbative effect in this work for a variety of reasons. First, no lines are observed when pulsing the laser into the thruster plume while propellant gas is flowing with the discharge off, indicating that no significant ionization of neutral xenon is occurring. Second, several xenon lines are visible in the



scattered spectrum collected during Thomson scattering measurements and there is no enhancement in line emission seen during full spectrum measurements with the plasma on. This indicates that a negligible amount of metastables are ionized by the laser beam. Third, experimental evidence shows that for the low particle density in the Hall thruster plume the probability of multi-photon ionization is very low. The power density at the laser focus is approximately  $9 \times 10^{10} \text{ W/cm}^2$ . Agostini et. al. [57] measured a xenon ion production rate of  $3 \times 10^6$  ions per pulse with a Nd:Glass laser operating at  $0.53 \mu\text{m}$  with the same power density at a pressure of  $2 \times 10^{-3} \text{ Torr}$ . Neutral pressure in the thruster used in this work is estimated to be this high at the channel exit, but is much lower than this value 10 mm downstream from the exit plane at the measurement location. This further confirms that the small amount of laser-produced ions and electrons is insignificant compared to the plasma density of approximately  $1 - 10 \times 10^{17} \text{ m}^{-3}$ .

### 3.5 Summary of Key Assumptions

Thomson scattering is a powerful diagnostic tool with broad applications. However, a number of simplifying assumptions have been made throughout this treatment and are summarized as follows:

1. Scattering is assumed to be incoherent, and the scattered signal can be treated as a linear superposition of many individual scatterers.
2. The magnetic field of the incident laser light is ignored. This can be justified for

non-relativistic scattering, i.e.  $v/c \ll 1$  [51].

3. The laser does not significantly disrupt the plasma. Reasons for this assumption are discussed above.

In order to validate Thomson scattering measurements it is necessary to take measurements of electron temperature and density using an accepted technique for comparison. The next chapter introduces electrostatic probes and discusses how they are used to determine temperature and density in a plasma.



# Chapter 4

## Electrostatic Probe Diagnostics

### 4.1 Introduction

The most common way to measure electron temperature and density in a discharge plasma is with electrostatic probes. Electrostatic probes have been a fundamental plasma diagnostic technique since the work of Mott-Smith and Langmuir in the mid-1920s [16]. Commonly called Langmuir probes, this class of probe consists of one or more small metal electrodes which are immersed in plasma. Tungsten is typically used for its ability to withstand high temperatures and for ease of probe construction. Langmuir probes have the advantage of providing local measurements of plasma properties, but the disadvantage of requiring sometimes complicated theory to determine the properties from the raw probe measurements. Probes of numerous designs have been used in almost every type of plasma,

ranging from low density collisionless plasmas to high density collisional fusion plasmas and everything in between. For the plasma conditions in this work only collisionless probe models assuming a Maxwellian distribution will be considered.

There are many types of Langmuir probe configurations, typically classified according to electrode number and shape [4]. The theory of current collection varies greatly depending on plasma conditions and probe type, and can range from very simple to incredibly complicated. In addition, while the theory of probes predicts I-V characteristics that are relatively simple to dissect, actual probe data typically provide traces that deviate from the ideal case. Because of this many theories and probe data-reduction techniques have been proposed to deal with these deviations. The probe measurements in this work were performed with a cylindrical double probe. In order to demonstrate why the double probe was chosen, single Langmuir probe theory and trace analysis will be discussed in addition to double probe theory.

## **4.2 Single Langmuir Probes**

The first Langmuir probes had a single electrode and usually came in one of three configurations: spherical, cylindrical, or planar. Spherical probes can be made by simply spot-welding a wire to a ball-bearing. Cylindrical probes can be made by inserting a wire into an insulting sheath such that only a small portion is exposed to the plasma. Planar probes are either of the disc type, with a wire spot-welded to a thin metal disc, or of the

flush type, with a flat piece of metal inserted in an insulating sheath such that the flat end of the conductor is flush with the insulator. Single probe theory and data analysis will be presented in the following sections.

### 4.2.1 Theory of Operation

The general theory of current collection for a single Langmuir probe is quite simple. The probe is inserted into the plasma and biased over a range of voltages, typically with respect to the vacuum chamber wall. With no bias applied the probe will experience both electron and ion thermal flux from the plasma, given by [18]:

$$\Gamma = \frac{1}{4} n_k \bar{v} \quad (4.1)$$

where  $n_k$  represents the species density and  $\bar{v}$  is the mean particle speed. Because the electrons are so much lighter and faster (and typically hotter), the probe will collect more electron current than ion current and begin to charge negatively. As the probe floats to a more negative voltage, some low energy electrons will be turned away by the potential field of the probe, but the probe will continue to charge. This process will continue until the potential of the probe is such that the electron and ion current flowing to the probe is exactly equal, and the probe assumes the floating potential,  $V_f$ , in the plasma.

Now that the probe is floating in the plasma, the potential of the probe must be varied to determine the plasma properties. If the probe tip is biased below the floating potential

the probe will begin to turn away more and more electrons and attract ions until only ions are being collected. Any further decrease in probe potential past this point will have a minimal effect on the collected current. The current collected at this operating condition is called the ion saturation current, and can be used to determine the plasma density. Biasing the probe positively with respect to the floating potential causes ions to be repelled and electrons to be attracted up until the point where all ions are being repelled. At this point any increase in probe potential has a small effect on the current being collected by the probe. This condition is called electron saturation, and the current measured by the probe is called the electron saturation current. This occurs when the probe is at or above the plasma potential. For a Maxwellian plasma the electron current collected is exponential as a function of voltage between the floating potential and the plasma potential, and is given by [58]:

$$I = I_{es} \exp \frac{-e (V_B - V_P)}{kT_e} \quad (4.2)$$

where  $I_{es}$  is the electron saturation current,  $V_B$  is the probe bias potential, and  $V_P$  is the plasma potential.

The preceding description is accurate for a simple two-species Maxwellian plasma in the thin-sheath limit, and some discussion of probe operation regimes is in order to clarify this point. A simple non-dimensional number characterizes the regime in which the probe is operating, given by the ratio of the probe radius,  $r_p$ , to the Debye length,  $\lambda_D$ . The Debye

length is a key characteristic length scale in the plasma given by [59]:

$$\lambda_D = \sqrt{\frac{\epsilon_0 k_B T_e}{n_e e^2}} \quad (4.3)$$

where  $\epsilon_0$  is the permittivity of free space,  $k_B$  is Boltzmann's constant,  $T_e$  is the electron temperature in Kelvin,  $n_e$  is the electron density in  $m^{-3}$ , and  $e$  is the charge of an electron in Coulombs. When the ratio  $\frac{r_p}{\lambda_D} \gg 1$  the disturbance in the plasma due to the probe is like a small skin on the electrode, and the area of the sheath is approximately equal to the area of the probe. In this situation the probe is said to be operating in the thin-sheath limit. In the opposite extreme ( $\frac{r_p}{\lambda_D} \ll 1$ ), the sheath is much larger than the probe itself and the current collected by the probe is not a function of the physical probe area, but of the sheath size. This regime is called “orbital motion limited”, since the probe collection mechanics are determined by the orbits of particles entering the sheath [60]. In between these two extremes is the transitional regime, which is traditionally avoided to limit the need for complicated analysis, although probe theories do exist to handle this regime [61].

#### 4.2.2 Single Probe Trace Analysis and Limitations

In practice, the probe potential is swept over a range of voltages and the current is plotted versus voltage, generating an  $I - V$  trace such as seen in Figure 4.1. This figure contains both an idealized trace (solid line) and a more typical trace (dashed line). For the ideal trace the general analysis algorithm would proceed as follows:



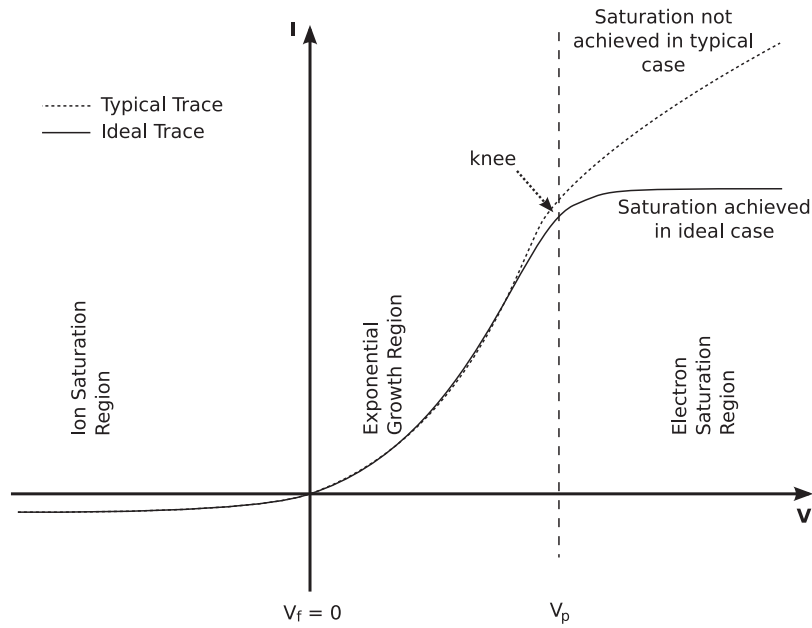


**Figure 4.1:** Ideal (solid) and typical (dashed) single Langmuir probe traces (©2009 Jason Sommerville, used with permission).

1. Fit the ion saturation region with a horizontal line
2. Find the floating potential ( $I = 0$ )
3. Determine  $V_P$  from the “knee” in the  $I - V$  curve
4. Take the natural log of the current from  $V_f$  to  $V_P$
5. Fit a line to  $\ln I$  to calculate  $T_e$
6. Calculate plasma density from the fit to ion saturation region

Such analysis is simple and straight forward when the trace conforms closely to the ideal shape, but often real probe data looks much worse. Single probe data can be extremely

difficult to interpret when there is either a lack of electron current saturation or the exponential electron region is not linear after taking the natural log of the current. It is often the case that the electron current continues to grow as voltage is increased above  $V_P$  instead of saturating. This is due to the growth of the plasma sheath surrounding the probe as the voltage on the probe is increased above plasma potential, as well as plasma fluctuations. One common way to try to determine  $V_P$  in this case is to take  $\ln(I)$  for all  $V > V_f$ , making the knee in the trace easier to see. If the natural log of the exponential electron region is not linear, it indicates that the plasma is not Maxwellian. Most electrostatic probe reduction techniques assume an isotropic Maxwellian plasma, and if the plasma does not satisfy those criteria the probe measurements become much more complicated. While in theory the second derivative of the probe current in the exponential growth region should yield the electron velocity distribution function [62], in practice the noise present in the probe current for low density plasma measurements make this difficult to determine.

In conclusion, single probes are versatile tools for plasma measurement but they are not without limitations. Plasma density, electron temperature, floating potential, and plasma potential can all be determined from good probe traces. However, most probe I-V characteristics are not quite ideal. Another drawback is that the plasma potential in the near field of a Hall thruster can range from a few volts all the way up to the discharge voltage. Single probes are swept relative to a fixed reference (such as the vacuum chamber wall or the cathode body), and performing low current voltage sweeps over such a large range can be difficult. Perhaps most importantly, the electron saturation current can be enormous in

the near-field plume of a Hall thruster, and substantial current draw can both disrupt the discharge and damage the probe.

## **4.3 Double Langmuir Probes**

Double Langmuir probes were first proposed by Johnson and Malter [63] in 1950. A double Langmuir probe typically consists of two single probes placed in close proximity to each other and insulated from ground. There are several advantages to using double probes that will be discussed in the following sections, along with double probe theory and trace analysis.

### **4.3.1 Theory of Operation**

Double probes are operated similarly to single probes, but with a few key differences. Instead of biasing the probe tips versus the vacuum chamber wall or the cathode, the voltage sweep is performed between the two floating probe tips. This allows the probe system to electrically float, allowing it to follow changes in plasma potential [64]. The current between the probes is measured as a function of the voltage applied between the probes. With no voltage applied between the probes no net current is collected by either probe, and both probes remain at the floating potential. As the voltage between the probes increases, one probe is pushed above the floating potential and the other is pushed below. The probe pushed below floating potential collects less electron current than the probe that

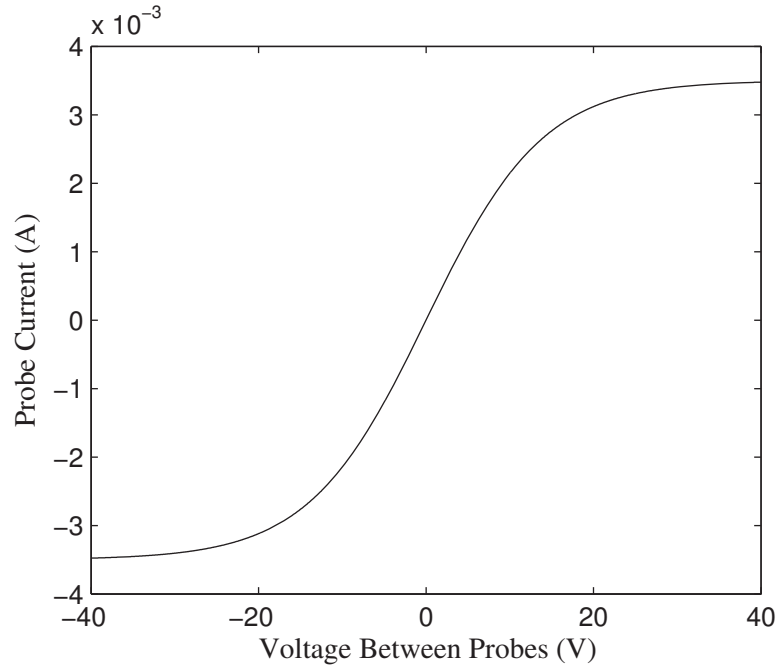


**Figure 4.2:** Ideal double probe trace.

is now above floating potential, resulting in a net current between the two electrodes. For large applied voltages the probe pushed below floating potential will repel all electrons and collect the ion saturation current. The other probe will still be negative with respect to plasma potential, but close enough to plasma potential that it can collect enough electron current to cancel the ion current flowing to it. At this point the current flowing between the probes is simply the ion saturation current. The same progression happens when the voltage between the electrodes is opposite in sign, however the current will then flow in the opposite direction, producing the curve seen in Figure 4.2. The maximum current that can be drawn by the system is limited to the ion saturation current, which is about two orders of magnitude smaller than the electron saturation current drawn by a single probe.

### 4.3.2 Probe Trace Analysis and Advantages

There are several ways to analyze double probe traces, including the line fitting method outlined by Chen [64], the peak separation method described by Brockhaus, Borchardt, and Engemann [65], the non-dimensional curve fitting procedure described by Peterson and Talbot [61], and the hyperbolic tangent method [66]. The author has compared all of these methods in previous work [67], and in additional unpublished work. The hyperbolic tangent method was used in all data analysis due to ease of use, the excellent curve fits to the real data, and close agreement with other methods.

Data analysis using the hyperbolic tangent method will now be described. Using this method requires the following assumptions: the electron energy distribution in the plasma is Maxwellian, the probe is operating in the thin-sheath limit, and the probes are of equal area (the ion saturation currents are equal). When these conditions are satisfied the ideal I-V characteristic is a hyperbolic tangent curve give by:

$$I = I_{sat} \tanh \left( \frac{eV}{2k_B T_e} \right) \quad (4.4)$$

where  $I_{sat}$  is the ion saturation current,  $k_B$  is Boltzmann's constant,  $T_e$  is the electron temperature in Kelvin, and  $V$  is the voltage applied between the probes. A least-squares

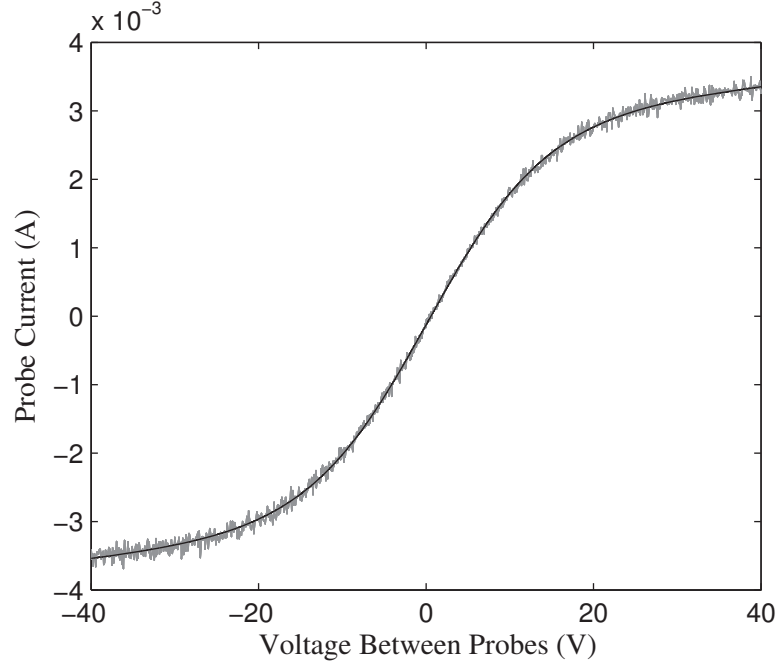


**Figure 4.3:** Actual double probe trace (gray) with curve fit (black).

hyperbolic tangent fit was performed according to the following equation:

$$I(V) = A \cdot \tanh[B \cdot (V - C)] + D \cdot V + E \quad (4.5)$$

where  $A$  is the ion saturation current,  $B$  is proportional to the inverse of the electron temperature,  $D$  helps to compensate for sheath expansion in the saturation regions [4], and  $C$  and  $E$  account for small offsets caused by stray capacitance in the probe system and gradients in the plasma [60]. An example of a double probe fit to real data can be seen in Figure 4.3.

Calculation of temperature, density, and plasma potential from a double probe trace is relatively simple. The electron temperature can be calculated directly through the following

equation:

$$T_e = \frac{e}{2k_B B} \quad (4.6)$$

where  $T_e$  is in Kelvin. Calculation of plasma density is not as straight-forward. In order to calculate plasma density one needs to start with the ion saturation current. For a quasi-neutral Maxwellian plasma with  $T_e = T_i$  the ion saturation current is given by [18]:

$$I_{sat} = \frac{1}{4} en A_p v_{i,th} = en A_p \sqrt{\frac{k_B T_i}{2\pi m_i}} \quad (4.7)$$

where  $e$  is the charge of an electron in Coulombs,  $n$  is the plasma density,  $A_p$  is the probe area, and  $v_{i,th}$  is the ion thermal speed, and  $m_i$  is the ion mass. However, in Hall thruster plasmas  $T_e \gg T_i$  and the ion saturation current is actually given by the Bohm ion current [58]:

$$I_{sat} = I_{Bohm} = 0.6 en A_p \sqrt{\frac{k_B T_e}{m_i}} \quad (4.8)$$

This equation can then be arranged as follows to yield the plasma density:

$$n = \frac{I_{sat}}{0.6eA_p} \sqrt{\frac{m_i}{k_B T_e}} \quad (4.9)$$

Once the electron temperature and plasma density have been determined, the plasma potential can be calculated according to [58]:

$$V_p = V_f - \frac{k_B T_e}{e} \ln \left( 0.6 \sqrt{\frac{2\pi m_e}{m_i}} \right) \quad (4.10)$$

This equation is valid for isotropic Maxwellian plasma. However, since plasma potential can not be measured by laser Thomson scattering it will not be considered further in this work.

### **4.3.3 Double Probe Advantages and Disadvantages**

Double Langmuir probes are often used in electric propulsion research for several reasons. First, when near or above the plasma potential a single probe can draw substantial electron current, thereby disrupting the plasma [64]. Second, it is common for the current collected by a single probe to increase with applied potential above the plasma potential, leading to a lack of distinct saturation. Third, when operating in strong magnetic fields the collection of electron current can be greatly altered, making the I-V characteristic difficult to interpret. Plasma potential is never reached by a double probe, so the first problem is eliminated. Since the probes can never collect more than the ion saturation current, one is more likely to find better saturation since the relatively massive ions are affected less by sheath growth, eliminating the second problem. Finally, a double probe is less dependent on electron current than a single probe for determination of plasma parameters so the effect of strong magnetic fields on double probe measurements is also reduced, minimizing the third problem.

Double probes do suffer from four key limitations. First, the fact that you have two probes inserted into the plasma instead of just one limits the spatial accuracy of the



measurement. Second, since the whole system floats with the plasma the floating potential cannot be directly measured by a double probe. For this work the potential of one probe with respect to ground was also measured, so that when the applied voltage is zero the floating potential is measured. Third, the plasma potential is not directly measured by a double probe. However, the temperature and density measured by the probe can be combined with the floating potential measurement to calculate the plasma potential. Fourth, the separation of the probes makes them susceptible to gradients in the plasma. In situations where the plasma conditions are changing rapidly in space, such as inside the discharge channel of a Hall thruster, the tips of the double probe may be in significantly different plasma conditions, which would cause asymmetry in the probe trace.

## 4.4 Probe Design and Implementation

In the near-field plume of a Hall thruster the Debye length typically ranges from 10s to 100s of  $\mu\text{m}$ . The diameter of the wire and its protruding length were chosen such that the exposed area is large compared to the Debye length to ensure operation in the thin-sheath limit. It is important to note that since the temperature and density are both functions of position, one may be operating in different probe regimes at different locations in the plasma. Prior to performing probe measurements the plasma temperature and density were estimated as approximately 10 eV and  $1 \times 10^{17} \text{ m}^{-3}$ , respectively. Using these the parameters the Debye length is approximately 74  $\mu\text{m}$ . Based off this estimate the electrostatic double probe used in this work consisted of two tungsten wires 1.27 mm in

diameter inside of an alumina sheath, with the wires protruding a length of 3.8 mm. This give a ratio of probe radius to Debye length of approximately 10, which places the probe in the thin-sheath limit. Actual probe measurements taken during this work showed that  $\frac{r_p}{\lambda_D}$  was actually over 30, validating use of the thin-sheath limit approximations in the data processing.

The probe was mounted on a 2-axis motion table described in detail in Chapter 5. Graphoil shielding in a low-drag wedge configuration was used to protect the probe stand and reduce aluminum sputtering. The probe was electrically driven with a programmable source meter controlled by an automated measurement program. Voltage between the probe tips was varied from -50 to 50 V in 0.1 V steps, with only a single sweep taken to reduce heating and ablation of the probe in the near-field plume plasma environment. Previous probe experiments showed saturation of the collected current at applied voltages of approximately 25 volts, and the range of -50 to 50 was chosen to ensure saturation was observed. For each operating condition the probe was quickly driven to the measurement position. Upon arrival a single sweep was taken, followed by immediate retraction. The total dwell time at the measurement position was approximately 3 seconds. Two individual measurements (insertion, sweep, retraction) were performed at each operating condition and the resulting electron temperatures and densities were averaged. During measurements the thruster discharge current was disrupted by a maximum of 5%, with minimal disruption typical. Discussion of the probe measurement results can be found in Chapter 7.



# **Chapter 5**

## **Equipment and Procedures**

### **5.1 Introduction**

A great deal of equipment is required in order to take measurements of Thomson scattering on a plasma device. The purpose of Chapter 5 is to describe the equipment used for the reported work and the procedures used when taking measurements. Also included in this chapter is a description of how the laser diagnostic system was calibrated.

## **5.2 Equipment**

### **5.2.1 Vacuum Facility**

All experiments were run in Michigan Tech's Xenon Vacuum Test Facility, which is a 2-m-diameter stainless steel vacuum chamber with a length of 4 m. Rough vacuum is attained with a 400 cfm Stokes<sup>®</sup> two-stage mechanical booster pump. High vacuum is maintained by two CVI<sup>®</sup> Torr Master<sup>™</sup> 48-inch cryogenic pumps with a combined pumping speed of 120,000 L/s (nitrogen) and a base pressure of approximately  $2 \times 10^{-6}$  Torr. Tank pressure was measured by a dual tungsten filament Bayard-Alpert style ion gauge mounted to a flange on the side of the of the vacuum chamber.

### **5.2.2 Motion Table**

The electrostatic probe was positioned using a 2-axis (X-Y) motion table manufactured by Techno Linear Motion Systems. Each axis is driven by a servo motor that can drive loads of up to 375 pounds at a maximum rate of 20 inches/sec. The 5 mm pitch ball-screws are equipped with anti-backlash nuts that provide an accuracy of  $\pm 0.1$  mm with a repeatability of  $\pm 0.01$  mm. An adjustable aluminum probe stand was attached to the motion table to allow for precise vertical positioning of the probe. The probes were driven into position, a single sweep was performed, and then the probes were rapidly retracted.



**Figure 5.1:** Motion Table with Probe Stand

The probe stand and motion tables were covered with Graphoil® graphite laminate sheeting. Graphoil® helps to reduce the amount of aluminum that is sputtered from the motion tables and probe stand by energetic ions and charge-exchange neutrals in the thruster plume. If not covered, sputtering of aluminum rapidly coats the collection optics and reduces the transmission of scattered light to the spectrograph. A secondary benefit of graphite shielding is that it helps to protect the probe stand from rapid heating from the plume during the brief periods of close proximity to the thruster. A picture of the motion table and probe stand can be seen in Figure 5.1.

### 5.2.3 Thruster

The Hall thruster used for this work was a 2-kW-class thruster similar to an Aerojet BPT-2000 [68–72]. The outer diameter of the thruster body is 120 mm and the channel width is 13 mm. Nominal power input is 2200 W at 350 V, which yields a specific impulse of 1,765 seconds (operating on xenon) with approximately 50% efficiency. The thruster weighs 5.3 kg and was operated at a variety of flow rates using xenon as propellant gas.

### 5.2.4 Cathode

The cathode used for this work was a laboratory cathode with a  $\text{LaB}_6$  emitter fabricated in the ISP Lab. The body is made of titanium and measures approximately 25 mm in diameter by 100 mm long. The cathode orifice is 4 mm in diameter. A tungsten keeper electrode is placed approximately 3 mm from the cathode face. Operating gas supplied to the cathode was also xenon for all experiments. Normally the cathode is mounted above the thruster and is aligned with the thruster centerline, but for this work the cathode was placed to the side such that the orifice was approximately 40 mm vertically above the end of the channel and 35 mm off-center from the axis of the thruster. The cathode was mounted to the side in order to give the laser a clear path to pass through the near-field plume. A picture of the cathode in this off-center position can be seen in Figure 5.2.

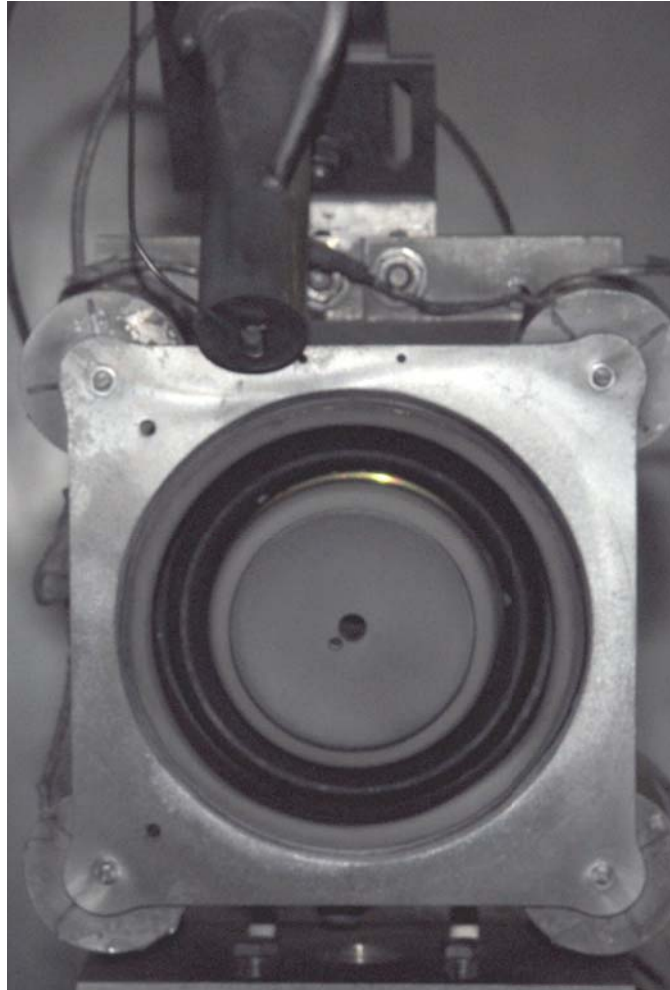


**Figure 5.2:** Photograph of the cathode location on the thruster. The cathode was mounted to the side in order to allow a clear path for the laser beam.

### 5.2.5 Mass Flow Controllers

The flow of gas to the anode and cathode was controlled by two MKS 1479a mass flow controllers. Accuracy of the mass flow controllers is 1% of full scale, with a 100 SCCM controller used for the anode and a 20 SCCM controller used for the cathode. Both units have particle filters upstream of the flow controller to prevent contaminants from entering



the device. The flow rate was calibrated at each operating condition by flowing the gas into a small calibration tank and measuring the pressure rise with an MKS type 622 Baratron pressure transducer

### 5.2.6 Laser

A Quantel YG980 Q-switched Nd:YAG laser with second harmonic generation was used for this work. At a repetition rate of 10 Hz the beam divergence is less than 0.45 mrad (full angle), with a polarization ratio over 80%. The laser output is horizontally polarized (parallel to the floor) upon exiting the amplifier at 1064 nm, and the polarization is converted to vertical during frequency doubling to 532 nm. The laser was operated exclusively at 532 nm for this work. Output energy is 610 mJ at 532 nm with a pulse duration of 6 ns (full width at half-maximum). Peak power can be calculated by:

$$P_{peak} = \frac{E_{pulse}}{t_{pulse}} \quad (5.1)$$

Using this equation the peak power at 532 nm is just over 100 MW. The laser has excellent operational stability, with shot-to-shot power drift of less than 4% over 8 hours of operation and pointing stability of  $< 0.45 \mu\text{rad}$ .

Control of the laser can be accomplished by either an attached remote control box or via an RS232 computer serial port. A dedicated computer controls both the laser and the iCCD. A LabView<sup>®</sup> program controls laser operation and contains numerous safeties to

prevent dangerous operating conditions. The laser also has a Q-switch synchronization TTL output signal that is connected directly to the iCCD for precise time-gated operation.

The laser consists of two main assemblies: the optical head and the utility rack. The optical head contains all of the components necessary for generating the laser light, including the oscillator, amplifier, and second harmonic crystal. The utility rack contains the main power supply, auxiliary power supply, cooling group, and all of the electronics for laser operation and interface with external devices. A 3 m umbilical connects the laser head with the utility cabinet, allowing placement of the laser on top of the vacuum chamber. The laser is clamped onto an aluminum platform that is inside of a positive-pressure/low dust enclosure made of polycarbonate and plastic sheeting. Positive pressure is maintained by an electric fan on top of the enclosure, and all incoming air is filtered for dust and other contaminants. The position of the laser can be seen in Figure 5.3. The aluminum box in front of the laser encloses the entrance optics to contain any scattering from the turning mirror and entrance window.

### **5.2.7 Beam Dump and Viewing Dump**

The laser passes through the plasma virtually unattenuated and a beam dump is required to dissipate the laser energy while preventing any scattered light from reaching the collection optics. The high intensity of the beam destroyed commercially available beam dumps, necessitating design and construction of a custom beam dump. After



**Figure 5.3:** Low Dust Laser Enclosure

experimentation with a cone-type beam dump proved that the laser power was too high for direct absorption or reflection, a beam dump using a series of semi-absorptive glass plates at Brewster's angle was designed. This design works for reasonably well-collimated beams as long as scatter from the glass surface is controlled and contained within the dump [73].

Design of the beam dump was based on the principles laid out by Rahn [74]. A schematic of the internal configuration of the beam dump can be seen in Figure 5.4. Light enters a 10.5 inch black-anodized aluminum tube and travels through the gap between the first and second plates. These top two plates are made of polished NG11 glass oriented at Brewster's angle so that the p-polarized light is transmitted with minimal reflection. The optical density of the glass is rather low, with only 20% of the light absorbed on a single pass through the glass. Due to imperfect alignment and surface irregularities some of the light is reflected at the surface and the light that isn't transmitted 'rattles' down the beam dump, losing energy at each interface. The bottom plate is made of NG1 glass that

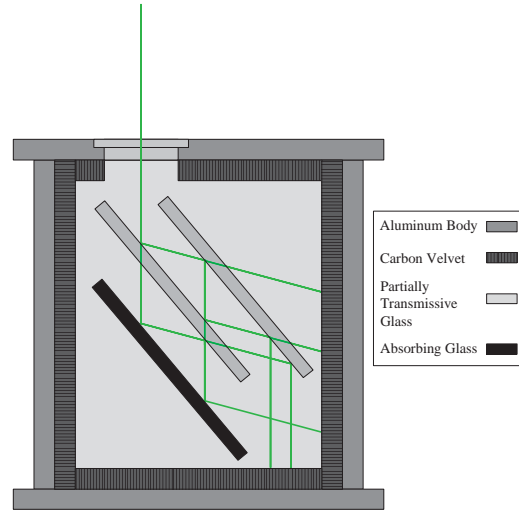


**Figure 5.4:** Schematic of the beam dump using black glass at Brewster's angle.

has a much higher optical density and can absorb more energy per pass than the NG11 glass without sustaining damage, since the light that makes it to the bottom plate has been greatly attenuated by the time it arrives. While this handles most of the incident beam, light can still work its way out to the sides of the beam dump. The inside of the beam dump is lined with VelBlack<sup>®</sup> carbon velvet to absorb this residual light. VelBlack<sup>®</sup> is an ultra-low reflectance material produced by Energy Science Laboratories, Inc. which has a reflectance of less than 0.5%. The combination of light absorbing glass at Brewster's angle, ultra-absorptive carbon velvet lining, and a long entrance tube (with baffle) makes the beam dump highly effective at preventing laser light from entering the acceptance cone of the collection optics. A picture of the inside of the beam dump can be seen in Figure 5.5.

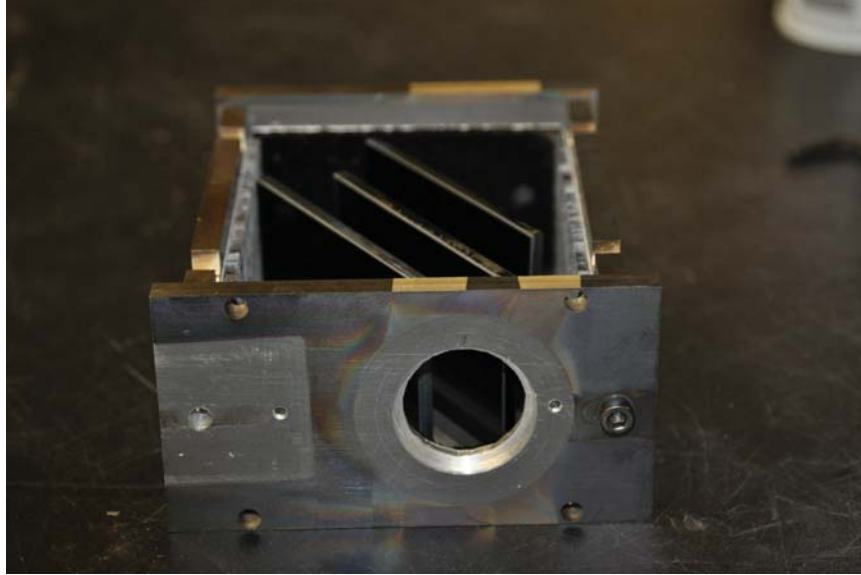


**Figure 5.5:** Picture of the inside of the custom beam dump.

A viewing dump is mounted opposite of the collection lens in order to further reduce stray light transmission in the system. The viewing dump is simply a 5-sided box made of VelBlack<sup>®</sup> deposited on aluminum sheeting. Having the detector looking into the viewing dump prevents any stray light bouncing around the tank from entering the collection optics from an angle that would make it appear to be from the scattering volume.

### 5.2.8 Spectrograph

The spectrograph used for this work was a Spex<sup>®</sup> Triplemate 1877C-AG triple spectrograph. A detailed schematic can be seen in Figure 6.1 in section 6.2. This imaging spectrograph is designed to provide excellent stray light reduction combined with a flat focal plane for use with two-dimensional imaging devices. The first stage consists of two Czerny-Turner monochromators with 600 gr/mm gratings coupled in subtractive-dispersive

mode. This pair provides a tunable bandpass filter with exceptionally steep roll-off ( $10^{-14}$  at 10 bandpass units), and passes a small spectral region of non-dispersed light to the final spectrograph stage. The final spectrograph has a 0.6 m length and is of asymmetrical Czerny-Turner design. There is a turret that holds up to three  $64 \times 64$  mm gratings that can be selected using an external knob. For this work an 1800 gr/mm holographic grating was used, providing approximately 11 nm of spectral coverage at the detector plane. According to spectrograph specifications the focal plane is undistorted and unvignetted over the entirety of the iCCD chip, and small deviations across the detector face were compensated for with non-uniformity correction and detector calibration.

Modification of the spectrograph from stock configuration was required for this work. The spectrograph has two ports on the back of the final spectrograph stage. One of the ports is equipped with mounting plates for attaching a detector. The second port is designed to allow back-alignment of the system by using a low-power alignment laser and flip-in mirror. Due to space limitations it was necessary to swap the functionality of the two ports. Instead of attaching a detector to the normal exit port, an aluminum platform was bolted into the back of the spectrograph. A custom 5-axis laser mount was attached that was composed of several smaller manipulation stages. A 5 mW Helium-Neon laser (633 nm) equipped with a 20x beam expander was then aligned with the optical axis of the spectrograph. In addition to the laser, a 1 inch diameter plano-convex focusing lens was placed on a multi-axis stage for use during optical alignment. A picture of the alignment apparatus can be seen in Figure 5.6.

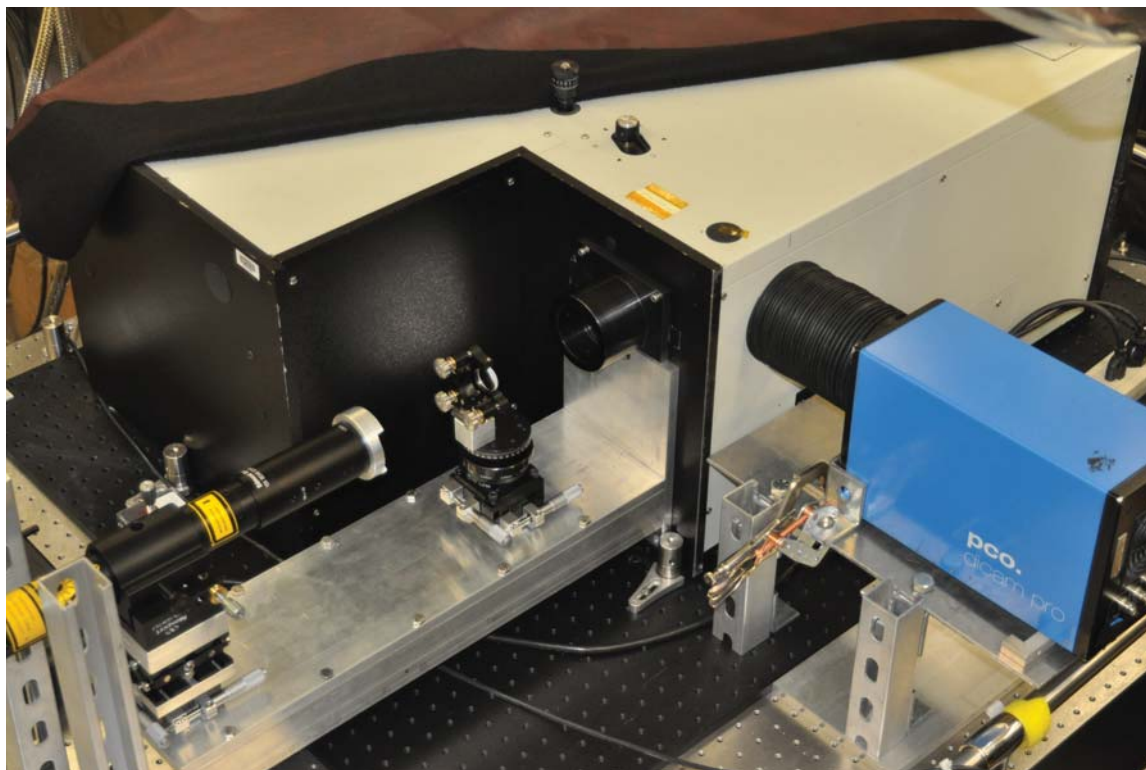


**Figure 5.6:** Apparatus for performing back-alignment of the spectrograph.

Additional changes were required to use the detector with the port normally used for alignment. The company that manufactured the spectrograph went out of business decades ago and the appropriate a flip-in mirror mount that fits the spectrograph could not be procured. The solution that was decided upon was to drill and tap the optical deck inside the spectrograph for installation of a magnetic base. A planar turning mirror was then installed in a 3-axis kinematic mount attached to the matching magnetic platform (Picture Here). The result is a turning mirror that can be accurately aligned with the camera one time, but can also be rapidly removed to allow back-alignment of the system prior to testing. After alignment the mirror easily locks back into its magnetic base with a return to zero within  $20\text{ }\mu\text{m}$ . A second aluminum platform was constructed to support the iCCD camera. The

camera was clamped to the platform for support and a flexible black-out tube was installed between the spectrograph wall and camera housing to block all outside light. The camera is inclined four degrees in order to reduce back reflections in the spectrograph.

### **5.2.9 iCCD Camera**

All imaging was performed with a Dicam Pro intensified CCD camera. The sensor element is of progressive-scan type with 'lens-on-chip' technology. Sensor format is SuperVGA with a scan area of 8.6 mm (H)  $\times$  6.9 mm (V). This range is covered by 6.7  $\mu\text{m}$   $\times$  6.7  $\mu\text{m}$  pixels, yielding sensor coverage of 1280 (H)  $\times$  1024 (V) pixels. The sensor is cooled by a two-stage Peltier thermoelectric cooler to an operating temperature of  $-12^\circ\text{C}$  in order to reduce the dark noise. Data is read off the CCD at 12.5 MHz by a 12-bit analog to digital converter with a conversion of  $5\text{ }e^-/\text{count}$ .

The key element of an intensified CCD is the intensifier itself, which in addition to supplying large gain to the signal can also be used to gate the intensifier. The Dicam can gate down to 3 ns but a gate time of only 20 ns was required for this work. Gating protects the detector by limiting its exposure to light while operating at high gain. Gain factors as high as 10,000x can be generated by the multi-channel plate(MCP) and over-exposing the MCP can saturate the signal or even cause localized etching of the photocathode. Gating the detector also allows one to gather light only in a short window containing the laser pulse, greatly reducing the contribution of continuous background emission from the plasma.



Control of the camera was performed using a program called PCO Camware from the Cooke Corporation. This software suite allows detailed control over gating, gain, triggering, binning, region-of-interest, and data output. The camera accepts a trigger input from the laser Q-switch synchronization output via a BNC cable and then transmits the data from the camera to the computer via a fiber-optic cable. Due to the low density of the plasma investigated in this work and the poor quantum efficiency of the photocathode (only 10% at 532 nm), the pixels were binned into 8 (H)  $\times$  32 (V) super-pixels in order to improve the detection limit and reduce acquisition times.

### **5.2.10 Laser Entrance Optics**

Steering of the laser beam is accomplished using a small optical breadboard mounted to the top of the vacuum chamber in front of the laser beam. The beam passes through two adjustable irises that serve to filter non-collimated components of the beam near its edges. Even though the laser has very low divergence, the optical power is so high that poorly collimated photons can contribute significantly to stray light in the vacuum chamber. After passing through the irises the beam is turned 90 degrees with a specially coated dichroic plane mirror designed to reflect high-power Nd:YAG laser beams. The laser then enters the vacuum chamber through a window at Brewster's angle to minimize reflections. A picture of the turning mirror and baffles can be seen in Figure 5.7.

The laser is focused into the plasma by a 1-inch-diameter plano-convex lens with a

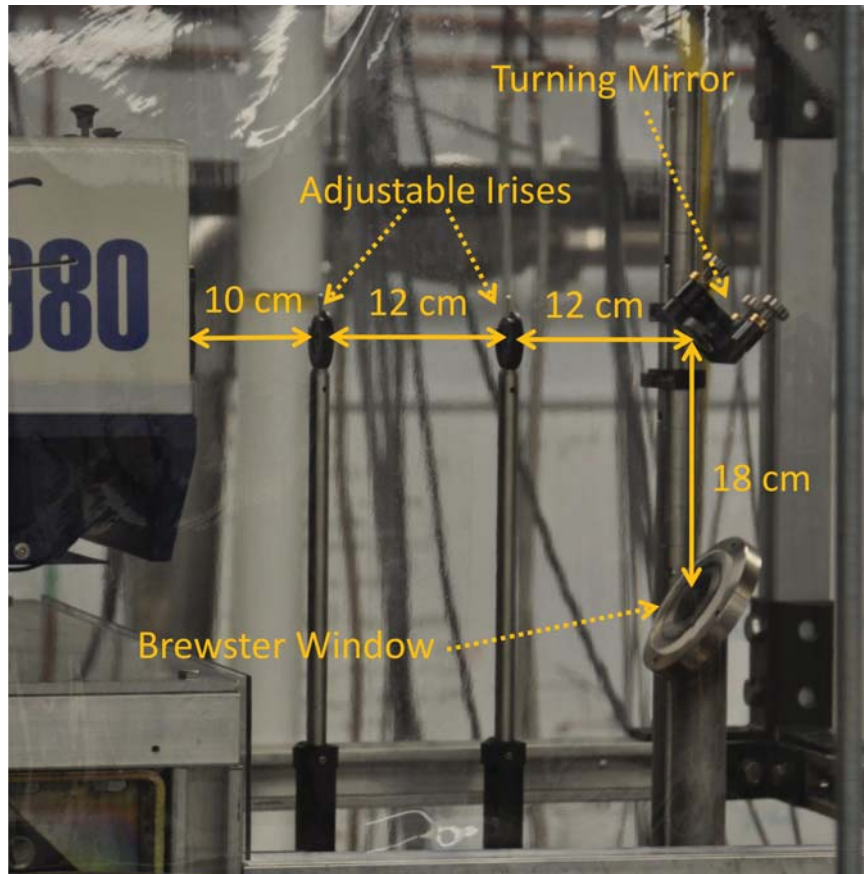


**Figure 5.7:** Laser turning mirror and entrance window.

focal length of 500 mm. This lens focuses the beam from a diameter of 9 mm to a spot approximately  $375\ \mu\text{m}$  in diameter. The lens is located one meter from the entrance window in an anodized aluminum tube. After passing through the lens the beam travels another 30 mm before exiting the tube and entering the plasma. The beam is then trapped by the custom beam dump described in section 5.2.7.

### 5.2.11 Collection Optics

The LTS diagnostic at MTU uses two lenses in infinite-conjugate configuration for collecting and focusing the scattered light onto the spectrograph entrance slit. The first lens collects and collimates the scattered light from the plasma. In order to maximize the signal passed to the detector the collection lens must collect as much light as possible. One limit on lens selection for this experiment was the size of the exit port on the vacuum chamber. The exit tube is 101.6 mm in diameter, but is lined with VelBlack<sup>®</sup>, which reduces the effective diameter to just over 80 mm. Having chosen the maximum diameter feasible (76.2 mm so a standard lens could be used), the focal length was chosen in order to position the lens as close to the scattering volume as possible without putting the lens in danger of damage from the thruster plume. A focal length of 100 mm was chosen, which gives an extremely fast  $f/\#$  of 1.3. Post-test examination shows minimal to significant coating of the lens as a result of its close proximity to the plasma, with the level of coating highly dependant on how long the thruster was operating. The collection lens is mounted in an anodized aluminum tube with an iris mounted on the front that serves as a light baffle. A picture of the collection optics can be seen in Figure 5.8.

The second lens focuses the collimated light from the collection lens onto the spectrograph entrance slit. This lens is also 76.2 mm in diameter, but with a focal length of 310 mm. This focal length was chosen in order to match the spectrograph input solid angle. The difference in focal lengths leads to a magnification of the image of the scattering

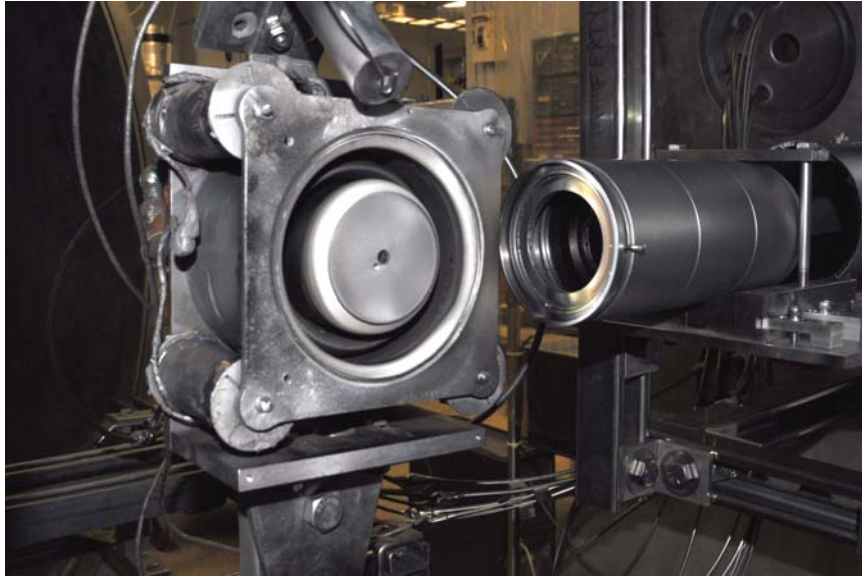


**Figure 5.8:** Collection lens and baffled exit tube.

volume by a factor of 2.97.

## 5.3 Data Acquisition

Now that the equipment has been described in detail the process of data acquisition can be presented. The entire scattering system is controlled with a dedicated computer system that runs two programs, one that controls the camera and one that controls the laser system. Since the camera is gated to only detect signal in a small window containing the laser pulse the camera requires a highly accurate trigger pulse. For a sequence of laser shots the trigger is provided by a synchronized output trigger on the laser control unit. The BNC trigger line is connected to the camera and provides a time-advanced rising edge trigger to the camera, which then waits a fixed delay before opening the electro-optical shutter on the camera. The camera shutter is only open for 20 ns each pulse, allowing the capture of the 6 ns (FWHM) laser pulse with some room for jitter in the electronics. This short gating time is critical for reducing the background emission light level from the plasma. For measurements with the laser off, the camera is triggered by an Agilent 33120A digital function generator operating at the laser repetition rate of 10 Hz. The shutter times are the same as for laser measurements so that the measured emission can be accurately subtracted from the total spectrum.

For all measurement conditions 27,000 acquisitions were taken, which was limited by the memory available in the camera. A simple timing diagram for laser measurements can be seen in Figure 5.9. Each individual acquisition is stored in a separate ascii file

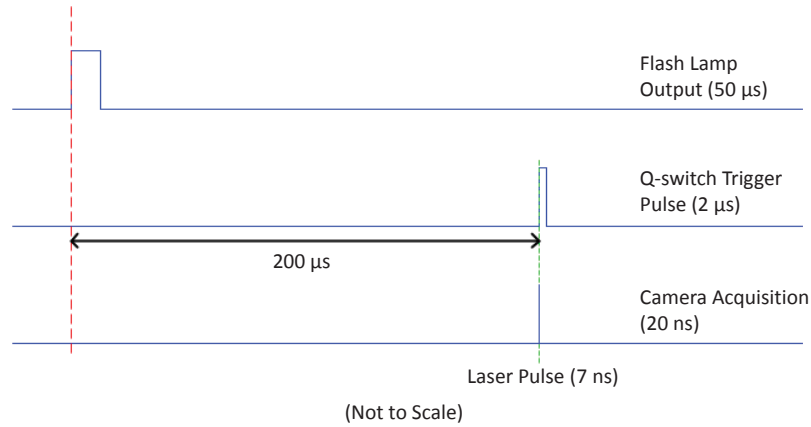


**Figure 5.9:** Timing diagram for laser measurements.

containing a two-dimensional matrix the size of the detector face, with each unit in the matrix corresponding to a binned super-pixel. The value of each matrix unit is the number of counts received during that particular pulse. A set of acquisitions makes up a stack of images, depicted in Figure 5.10.

The binned detector contains 14 rows (spatial dimension) and 160 columns (wavelength dimension), but not all of the super-pixels are used during data processing. The height of the entrance slit of the spectrograph determines how much of the iCCD chip will be illuminated in the vertical direction, and for an entrance slit height of 2 mm there are 6 rows uniformly illuminated (determined by measurement of Rayleigh scattering). Above and below these 6 rows the signal strength decreases rapidly, and the values recorded at these rows are not used in LTS calculations.

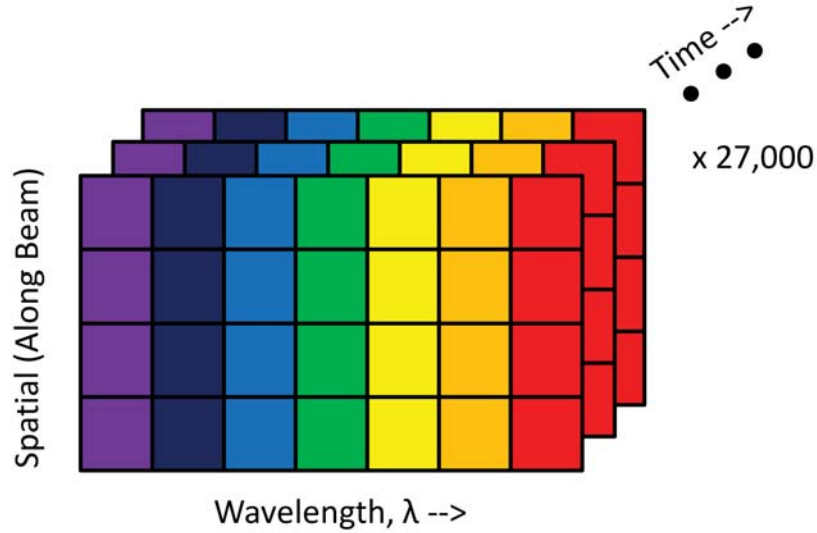


**Figure 5.10:** Diagram illustrating the manner in which ICCD data is recorded and stored. Each laser shot produces a 2-D array the size of the binned detector face containing the number of counts recorded at each super-pixel during the acquisition.

## 5.4 System Alignment and Calibration

### 5.4.1 Alignment

A complete system alignment was performed prior to every test, starting with the collection optics and spectrograph. All slits were completely opened and both the pre-monochromator stage and the spectrograph stage were set to zero-order (reflective) operation. The turning lens described in section 5.2.10 is removed from its base and the back-alignment laser is turned on. A focusing lens is placed in front of the beam in order to focus the laser onto the flat-field plane of the spectrograph. Doing so produces a beam that

is aligned with the optical axis of the spectrograph and is exiting at the monochromator acceptance angle ( $f/3.9$ ). This light is then collimated by the first (matching) lens and focused to a spot by the second (collection) lens.

Having determined where the spectrograph is in focus, alignment from the laser side of the system is performed. When aligning the laser the first step was to increase the delay between the flash lamps and the Q-switch in order to reduce the laser output to a power level safe for visual alignment. Both irises in front of the laser were opened and the laser was turned on in continuous pulsed operation mode. Using the turning mirror on top of the tank the laser was steered to intersect the focal point of the spectrograph alignment beam. This region of intersection is referred to as the scattering volume, and is defined by the cross-section of the laser beam and the height of the entrance slit of the spectrograph. The beam dump was then carefully positioned in the bottom of the tank to ensure the proper angle of incidence on the beam dump glass. The irises along the laser path were then adjusted in order to improve the spot quality at the beam waist.

With the scattering volume defined, the thruster was positioned such that the scattering volume was along the centerline of the discharge channel. Due to the speed of the focusing lens the closest the thruster could be positioned was such that the scattering volume was 1 cm from the exit plane of the discharge channel. This region has considerable plasma density and electron temperature, but also allows for probe measurements provided residence time is short (less than about 10 seconds). Probe alignment is then performed by



positioning the probe such that the center of the topmost probe tip intersects the Nd:YAG laser and then HeNe alignment laser is focused between both probe tips. This places the center of the active area of the probes in the scattering volume.

### 5.4.2 Rayleigh Calibration

In order to have an absolute measure of density the system must be calibrated using Rayleigh scattering off of a gas at known pressure and temperature [35]. The system is pumped down to the 1 to 10 Torr range and allowed to sit for several hours (usually overnight) to allow dust to settle. The dust particles have scattering cross-sections orders of magnitude larger than gas molecules [51] and must not be included in the calibration. The laser is then pulsed at the same power, repetition rate, and number of shots used for acquisitions with the thruster operating. Since the Thomson signal is directly proportional to density, the electron number density can be determined from [54]:

$$n_e = n_R \frac{\sigma_R}{\sigma_T} \frac{P_T}{P_R} \frac{\int_{\lambda} I_T}{\int_{\lambda} I_R} \quad (5.2)$$

where  $n_R$  is the number density of the calibration gas (nitrogen),  $\frac{P_T}{P_R}$  is the ratio of laser powers for the 2 measurements (in this case unity), and  $\int_{\lambda} I_x$  is the integrated intensity of each spectrum.

## 5.5 Procedure

### 5.5.1 Measuring the Thomson Scattering Spectrum

Chapter 3 was concerned with the details of what happens when a laser beam is directed into a plasma. The details of this interaction are important, but when Thomson scattering measurements are performed there are additional contributions to the measured spectrum that are not a product of laser-plasma interaction. Some of these contributions are caused by the measurement apparatus and some come from the plasma itself. All of the components of the total scattered spectrum that is measured will now be introduced one at a time.

To begin, consider the case when the laser is fired into the vacuum chamber with the plasma off. As the laser encounters the turning mirror, focusing lens, and vacuum chamber entrance window light is scattered during each surface interaction. This light can then bounce around the vacuum chamber and enter the collection system as if it originated from the scattering volume. The light that arrives at the detector in this way is called stray light. It is detected at the laser wavelength but is broadened by the instrument function of the spectrograph. This imperfect transfer function arises due to the fact that the slits in the spectrograph have finite size and the spectrally narrow laser light arrives at the detector with some degree of spectral spread. A sample spectrum produced by stray light arriving at the detector can be seen in Figure 5.11.

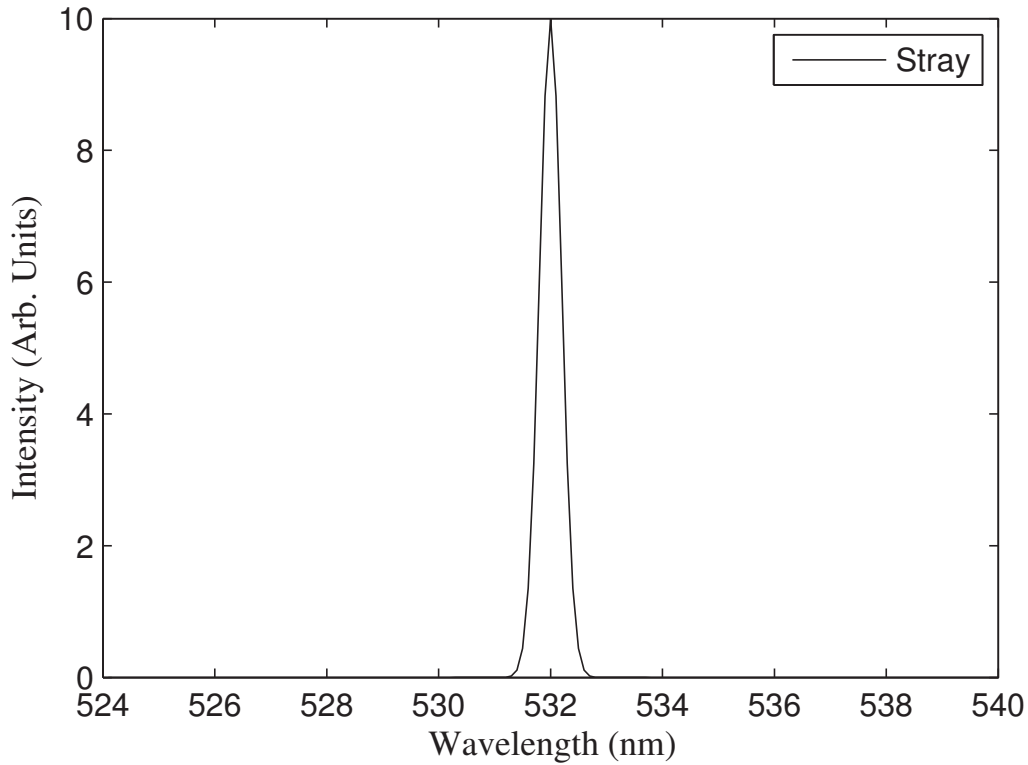


**Figure 5.11:** Simulated example of stray light measured at the detector. The light is broadened by the instrument function but is still relatively narrow and centered at the laser wavelength.

For the next case, consider that propellant is now being fed to the Hall thruster and the laser is once again being fired past the face of the thruster. The discharge is off so there is still no plasma, however there are xenon atoms that can produce Rayleigh scattered light. Light that is Rayleigh scattered by xenon atoms is also detected at the laser wavelength, and is broadened from two sources. The first source of broadening is the instrument function of the spectrograph and the second is from Doppler broadening due to the thermal motion of the atoms. Xenon atoms are typically very cold (less than 0.1 eV) and the Doppler broadening can be neglected. The scattered signal that will be measured in this situation

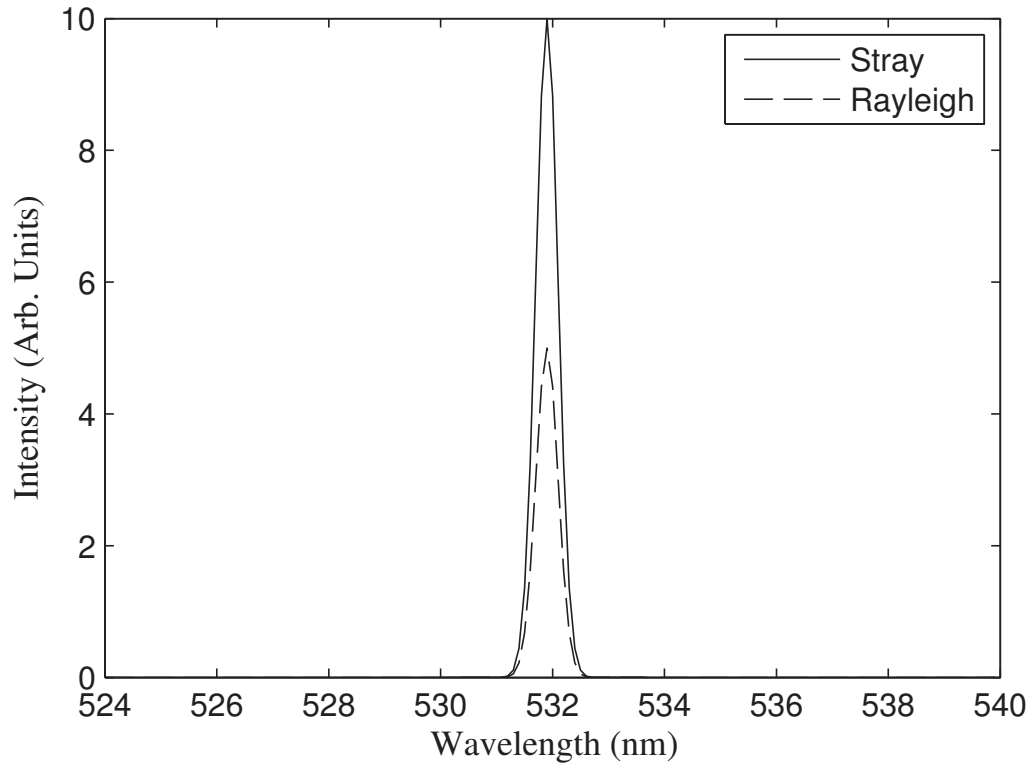


**Figure 5.12:** Simulated example of stray light and Rayleigh scatter measured at the detector. The Rayleigh scatter is also slightly broadened and is centered at the laser wavelength.

will contain both the Rayleigh scattering from the propellant gas and the unavoidable stray light signal, which can be seen in Figure 5.12.

For the next case consider that the Hall thruster discharge is now on and the laser is passed through the plasma. Two new components will then be added to the spectrum. The first component is due to plasma emission, and consists of both weak broad-band emission and relatively strong line emission. The final component is the Thomson scattering signal produced by the scattering of laser photons from free electrons in the plasma and contains

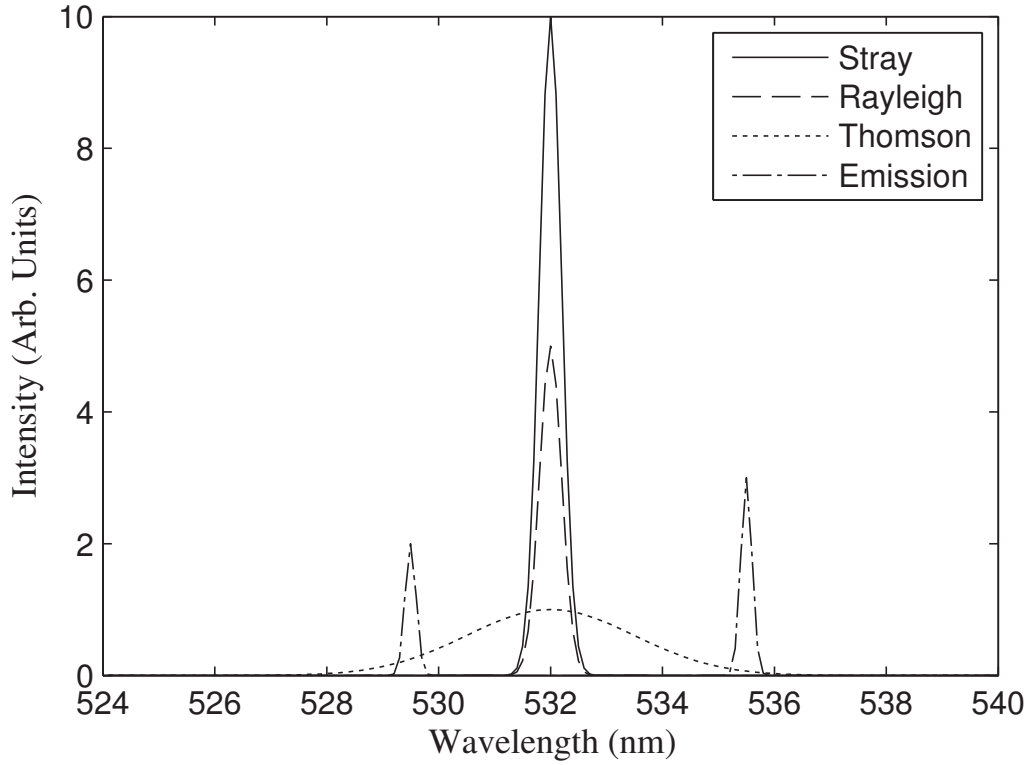


**Figure 5.13:** Simulated example of all the components of the signal measured at the detector. This figure is for illustrative purposes and the spectrum components are not to scale.

the electron velocity distribution information. If we assume an isotropic plasma the Thomson signal will also be centered on the laser wavelength, but will be significantly more broad than the stray and Rayleigh signals since the Thomson signal is primarily broadened due to the fast thermal motion of the electrons. A simulated spectrum with each of the individual components can be seen in Figure 5.13.

The relative strength of each component depends on both the plasma conditions and the measurement apparatus. Plasmas contain multiple ion species and the line emission is

relatively strong. The characteristics of the Thomson component depends on the plasma conditions. If the plasma is hot and dense the Thomson signal will be broad and large in amplitude. The stray light can be relatively weak for a laser measurement in an open geometry, or many orders of magnitude higher if the measurement occurs in close proximity to walls or windows in the vacuum chamber. The Rayleigh component depends on the relative density of heavy particles in the plasma, and can be strong for atmospheric pressure plasmas or negligible for low density plasmas. These individual components of the spectrum were previously shown separately, but the sum of all the contributions is what is actually measured at the detector. A sample spectrum containing all of the components can be seen in Figure 5.14. From now on a spectrum that contains all contributing sources will be referred to as a “total” spectrum. Figure 5.14 is an actual measured spectrum.

In order to determine the electron velocity distribution function and density we need to isolate the Thomson component of this total scattered spectrum. For this work we are not concerned with the strong stray/Rayleigh signal at the laser wavelength since the Doppler broadening from heavy particle motion is less than the spectral resolution of the detection system and the heavy particle temperature cannot be determined. A zoomed-in version of Figure 5.14 that more clearly shows the Thomson and emission signals can be seen in Figure 5.15. The way that the Thomson spectrum is determined is by performing multiple measurements in order to isolate certain components of the scattered signal which can then be subtracted from the total spectrum to obtain the corrected Thomson spectrum (this will also be referred to simply as the “corrected” spectrum). The details of these measurements

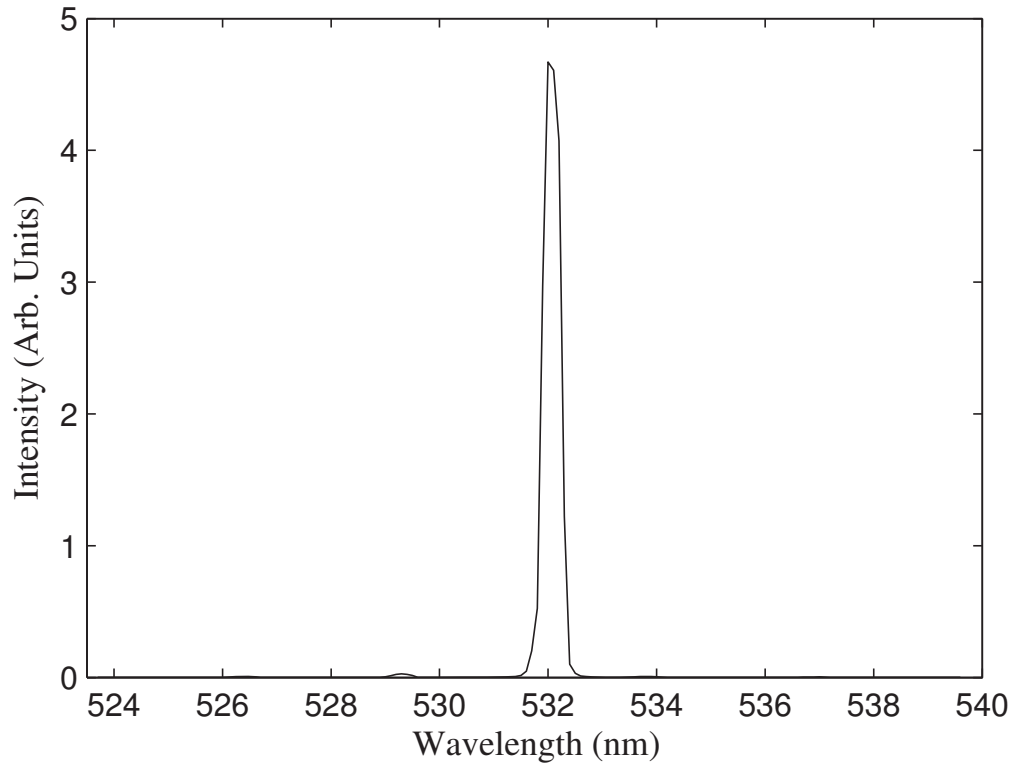


**Figure 5.14:** Example of the total scattered spectrum measured at the detector.

will be discussed in the following section.

### 5.5.2 Laser Measurements

Thomson scattering spectra are always determined by taking the difference of at least two separate measurements [15]. The typical way in which the Thomson spectrum is isolated from the total spectrum is by performing three separate measurements at each thruster operating condition.

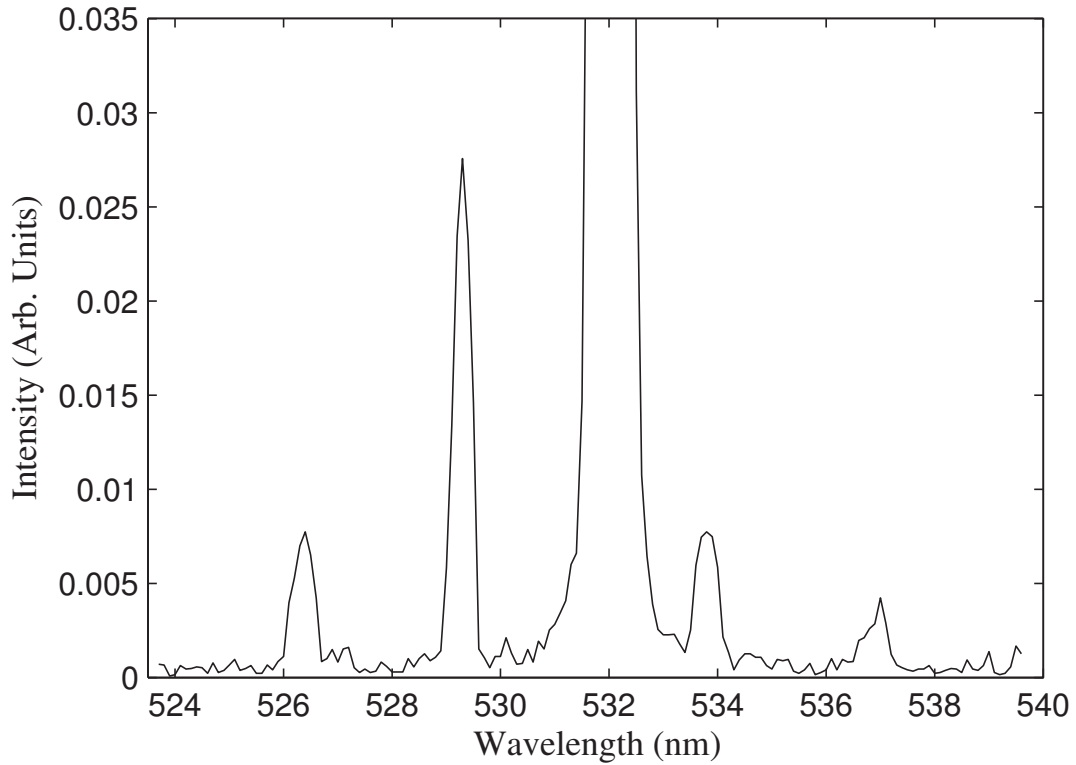


**Figure 5.15:** Sample total spectrum zoomed in to display the Thomson and emission components.

1. The first measurement is taken with the Hall thruster operating at the nominal condition with the laser off. This data set contains the background emission spectrum of the thruster for that specific operating condition. Since the laser is off the only contribution to the spectrum is due to emission. This will be referred to as the emission spectrum.
  
2. A second measurement is made with the thruster operating and the laser on. This measurement contains all of the possible contributions, including Rayleigh scattering, Thomson scattering, the stray light, and the background plasma emission.



This will be referred to as the total spectrum.

3. A third measurement is performed with the thruster discharge off and the laser on.

This measurement contains the stray light contribution to the spectrum and minimal Rayleigh scatter from the propellant gas, and will be referred to as the stray spectrum.

Construction of the corrected Thomson spectrum from these measurements is accomplished by subtracting the stray spectrum and emission spectrum from the total spectrum. Performing this subtraction leaves only the Thomson spectrum, which is a direct measure of the electron velocity distribution in the plasma. The full details of how these three sets of 27,000 acquisitions are processed to determine the various spectra are discussed in Chapter 6.

### **5.5.3 Probe Measurements**

For each operating condition of the thruster two corresponding probe traces were taken (see Section 4.4). When not in use the probe sits approximately 1.5 m downstream of the thruster and 0.5 m from the thruster axis. The motion table control software moves the probe into the measurement position and performs a single sweep before moving back to the home position. Residence time at the measurement location is approximately three seconds. The current and voltage during the sweep are recorded into an HDF5 file, along with all of the thruster operating parameters. Details of the probe data analysis can be found in Chapter 4.

# Chapter 6

## Laser Data Analysis

### 6.1 Introduction

Analysis of the scattered data is necessary in order to determine the temperature and density in the plasma. A detailed description of Thomson scattering theory was provided in Chapter 3, but this only covered the scattering event itself. The collection optics described in Chapter 5 collect only a small fraction of the scattered signal and there are additional losses as the photons move through the spectrograph to the detector. The purpose of this chapter is to provide a detailed discussion of detection and processing of the scattered photons.

## 6.2 Thomson Scattering Detection

Before discussing how the data is processed it is worthwhile to cover the entire detection process, starting with a single laser pulse. The process begins when the Q-switched laser emits an intense pulse of spatially and temporally coherent photons at a wavelength of 532 nm. This “swarm” of photons is focused into the plasma at the desired location in the plume, and as the photons pass through the plasma they have a chance of interacting with the free electrons in the scattering volume. It is important to note that the probability of Thomson scattering occurring is incredibly small. The total number of photons scattered into a given solid angle can be estimated by [35]:

$$N_p = \left( \frac{I_L}{h\nu} \right) \Delta V n_e \frac{d\sigma_T}{d\Omega} \Delta\Omega \tau_L \quad (6.1)$$

where  $I_L$  is the laser intensity,  $\Delta V$  is the size of the scattering volume,  $n_e$  is the electron density,  $\frac{d\sigma_T}{d\Omega}$  is the differential Thomson scattering cross-section,  $\Delta\Omega$  is the detection solid angle, and  $\tau_L$  is the length of the laser pulse. Using the relevant parameters from the LTS diagnostic at MTU yields a value of approximately 685 photons per pulse. This number is quite small considering the total number of photons emitted by the laser in a single pulse, given by:

$$N_{p,total} = \frac{E_{pulse}}{h\nu} \quad (6.2)$$

is approximately  $1.61 \times 10^{18}$  photons! The probability of a photon being scattered into the detection solid angle is a mere  $4.27 \times 10^{-16}$ , which means that most photons simply pass through the scattering volume without ever scattering off an electron. Of the few electrons that actually encounter photons, most will scatter the photon in a direction other than the collection optics, and the signal will be lost.

Matters get even worse when the losses that occur in the collection system are considered. As described in Chapter 5, the photons that are scattered into the solid angle subtended by the collection optics are collimated by a lens and passed through the vacuum chamber exit window to a second lens that focuses the image of the scattering volume onto the triple-spectrograph entrance slit. Both of these lenses and the window have transmission coefficients of between 90 and 95 percent. The spectrograph contains multiple mirrors and diffraction gratings, all of which can attenuate the signal on its way to the detector. A schematic of the internal arrangement of the spectrograph elements can be seen in Figure 6.1. Once the scattered light has entered the spectrograph it is collimated by a curved mirror (M1). The light is then passed to a diffraction grating that disperses the light spectrally (G1). After this initial dispersion the light is focused by another mirror (M2) through a slit (S2) that controls the bandwidth of light that is passed through to the detector. The light then encounters a folding mirror (M3) followed by a second collimating mirror (M4). The collimated light then encounters a second diffraction grating (G2), followed by a mirror (M5) that focuses the light onto the entrance slit (S3) of the final spectrograph stage. In the final spectrograph stage the light is once again collimated by a mirror (M6) before

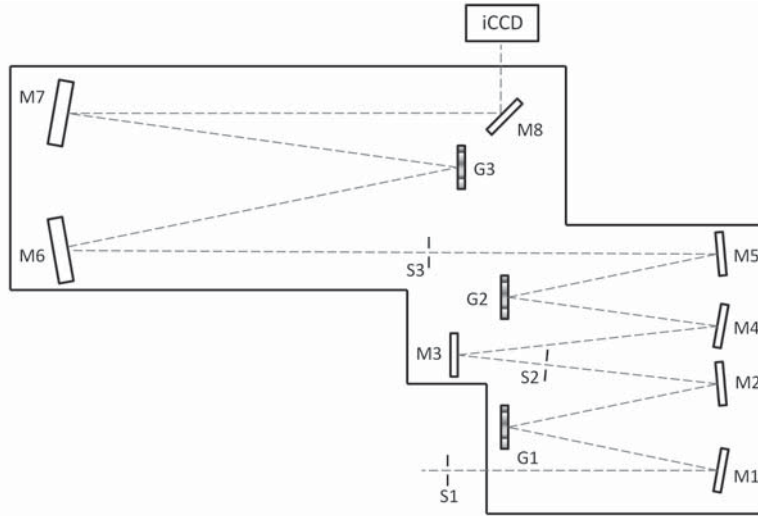


**Figure 6.1:** Internal Geometry of a Modified Spex Triple-Mate Spectrograph.

being passed to the final dispersive element (G3). The dispersed light is then reflected by a focusing mirror (M7) onto the final turning mirror (M8), which sends the light to the iCCD. Assuming the mirrors reflect 97 percent of the light and the gratings have efficiencies of approximately 50 percent each, the total system throughput is only 8.4 percent. As a final loss term, the iCCD has a quantum efficiency of only 10 percent in the visible spectrum near 532 nm, which means the total number of photons that are detected on (average) each laser pulse is only 5.75.

Measurement of Thomson scattering spectra varies a great deal depending on the strength of the scattered signal. For plasmas with high densities, such as fusion plasmas and plasma torches, the signal can be strong enough that it can be measured directly in a single laser pulse. As the density decreases fewer photons are scattered per pulse, and it

is common to use pulsed lasers with high repetition rates combined with gated detectors to accumulate the scattering from tens to hundreds or even thousands of pulses. Further decreases in density require the use of photon counting methods and long measurements consisting of tens of thousands of laser pulses. The plasma conditions and measurement equipment available for this work stretch the limits of detection, and a new method of data processing was developed to handle the exceptionally small photon fluxes that were detected. This method will be discussed in detail in section 6.6.

## **6.3 Experimental Challenges**

Performing laser Thomson scattering measurements on a Hall thruster presents its own unique set of challenges. The next few sections will discuss some of the most important factors and how they affect the measurement of Thomson scattering.

### **6.3.1 Difficult Optical Access**

Optical access to Hall thruster plasma is difficult for a number of reasons. The laser beam is incredibly powerful and must be focused from a diameter of 9 mm down to a diameter of approximately  $375\ \mu\text{m}$  in the scattering volume, after which the beam diverges and enters the beam dump at a reduced power density. During this time it is important that the beam does not encounter any objects. If the beam was to hit any part of the thruster material would be ablated, and after only a few pulses the thruster could be permanently

damaged. Such beam collision also produces enormous quantities of stray light, and if the stray light is intense enough the spectrograph will not be able to suppress the light from nearby wavelengths. This can either modify the measured signal at wavelengths near the laser or be so large that the signal is obscured.

Another issue related to beam access involves the geometry of the measurement and limitations on where the beam can pass through the plasma. Because the laser pulse envelope is rapidly converging on its way to the scattering volume there is a limit to how close the scattering volume can be to exit plane of the thruster. A simple diagram of the beam geometry can be seen in Figure 6.2. The vertical cone is the envelope of the beam that is traced out as the photon packet passes through the plasma to the beam dump and the lighter cone marks the solid angle subtended by the collection lens. The closest the scattering volume can be to the thruster exit plane in this configuration is approximately 4 mm if the  $1/e$  intensity point is considered to be the beam radius, but in practice the point of closest measurement is further away. The reason for this is that for the intense pulses used in this work there is significant energy far away from the center of the beam due to imperfect beam quality, and the scattering produced by this energy can saturate the iCCD at the laser wavelength. For this work all measurements were taken at a distance of 10 mm from the thruster exit plane. This allowed a relatively close measurement in order to maximize the signal while avoiding stray light from photons reflecting off of the thruster. A top-down view of the beam path and scattering volume can be seen in Figure 6.3.



**Figure 6.2:** Geometry of the probing beam and scattering solid angle.

It is clear from the previous description of optical access issues that internal measurements of a Hall thruster are extremely difficult to carry out. Internal measurements require modification of the thruster itself to allow the beam to pass through the discharge channel without creating a massive quantity of stray light, and also modifications that allow collection optics to see into the discharge channel. This places limits on the beam diameter since removing large sections of the thruster body for beam access may greatly alter thruster operational characteristics. Using a smaller beam with sufficient power then creates its own





**Figure 6.3:** Top view of the beam path and scattering volume. The dark green dot indicates the laser focus and the lighter green circle represents the beam diameter approximately 0.3 m from the focus (above and below).

problems as the increased power density makes beam steering and dissipation difficult. Even if relatively small access ports are added to the thruster body and a beam of sufficient power can be delivered there is still the problem of alignment, discussed in the next section.

### 6.3.2 Alignment

Beam alignment is critical for laser scattering measurements. The exceptionally small number of detected photons from each pulse calculated in section 6.2 assumed perfect alignment, which can be difficult to obtain when performing LTS on Hall thrusters. Hall thrusters in the 2-4 kW power range require fairly spacious vacuum chambers to operate

without inducing facility effects. The distance from the output of the laser to the scattering volume is approximately 2.5 m, with a turning mirror, entrance window, and focusing lens in the path. When the chamber is rough-pumped down the flange with all of the entrance optics on it can shift in position as the air pressure difference causes the sealing gaskets to compress. Partial compensation for this effect comes from using the Rayleigh scattering intensity to align the system at rough vacuum, but no such corrections can be made when the system is pumped down to hard vacuum since the pressure is too low to detect significant changes in the weak Rayleigh scattering signal over the stray light.

In addition to the vacuum chamber elements shifting as the pressure changes, the heat produced by the thruster adds a thermal load to the mounting structures in the vacuum chamber. The thruster itself is mounted on a stainless steel uni-strut structure, and the first collimating collection lens is mounted on a similar stainless structure in close proximity to the thruster. As the thruster heats these mounting structures and the aluminum lens barrel there is a degree of thermal expansion and warping of the structures due to uneven heating by the thruster. Such deviations in alignment produced by these changes are both difficult to adjust for and highly dependent on the operating conditions of the thruster. There were instances where no scattered signal could be detected after a full pump-down, and after attempting to align by making blind adjustments to the turning/steering mirror, the vacuum chamber had to be vented and a re-alignment performed.

For the MTU LTS system even very small angular adjustments on the steering mirror

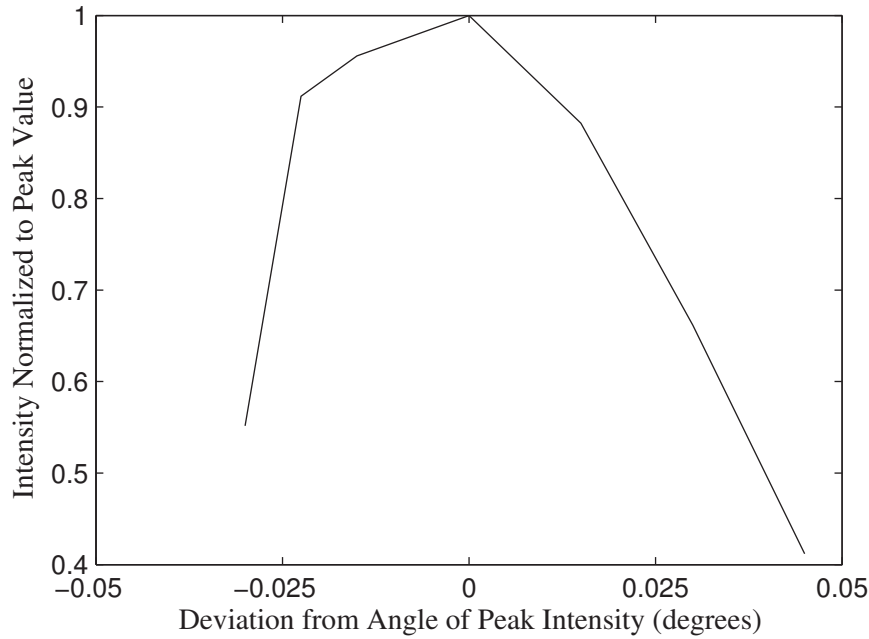


**Figure 6.4:** Effect of angular alignment on the detected scattering signal.

can move the focal point of the laser significantly. A plot showing the effect of angular deviation on the strength of Rayleigh scattering measured during calibration can be seen in Figure 6.4. As the beam angle is changed the laser begins to move out of the focal volume of the collection optics and the detected Rayleigh signal decreases rapidly. Even if the beam is initially aligned small changes in position of the collection optics or focusing beam can cause serious degradation of the detected scattering signal.

## 6.4 Determining the Corrected Spectrum

The process of laser measurement was described in Chapter 5, but the raw data sets that result from the measurements must be processed in order to determine the Thomson

spectrum. For incoherent Thomson scattering measurements on low temperature plasmas it is often the case that the Thomson signal is relatively narrow and not much wider than the redistributed stray light. In these situations the stray light and Rayleigh scatter near the laser wavelength must be handled carefully. If the heavy particle densities are high it is often necessary to physically block the light at this wavelength from being transmitted through the spectrograph in order to protect the detector (often called a “Rayleigh block”). This effectively eliminates the stray light and Rayleigh signals scattered from the plasma, but not without some distortion of the spectrum near the stop-band. Since there is no stray/Rayleigh signal to detect when using a Rayleigh block the corrected Thomson scattering spectrum is obtained by subtracting the emission spectrum from the total spectrum, while the region centered at the laser wavelength that is obstructed by the Rayleigh block is ignored during data analysis.

When the stray light and Rayleigh signals are weak enough that measuring them will not damage the detector it is possible to use the total, emission, and stray spectra to construct the corrected scattering spectrum. Bowden et. al. [43] constructed a corrected spectrum for his multi-pass cell system by subtracting both the emission spectrum and the stray spectrum from the total spectrum, but concluded that while the signal near the laser wavelength was “contaminated” by the stray light and Rayleigh scattering signals, the outer parts of the spectrum were unaffected by the stray and Rayleigh signals due to how narrow they are spectrally. During preliminary measurements in this work it was determined that the anode mass flow was small enough that it made a minimal contribution

to the stray/Rayleigh spectrum (this has been referred to simply as the stray spectrum for this reason). In order to reduce measurement time and extend the laser flash lamp life a single measurement of the stray light was performed at the start of each test, and the emission and total spectra measurements were performed at each operating condition. The next sections will describe the methods used to process the sets of 27,000 acquisitions in order to obtain a single spectrum for each measurement condition (one each for the total, emission, and stray light) at each operating condition that can be used to determine the corrected Thomson spectrum.

## **6.5 Current Methods of Data Processing**

Before discussing the methods used to process the data collected in this work it is worthwhile to discuss some of the processing methods that have been used to date, and why a new processing method was developed. The next few subsections will describe the three main methods of processing Thomson scattering data and assessments of their suitability for application to the measurements taken for this work will be given.

### **6.5.1 Single-Pulse Measurement**

The simplest method of data processing is what I will call single-pulse measurement. For plasmas with relatively high electron density and electron temperature (such as fusion reactors and field-reversed configuration plasmoids) a complete Thomson spectrum with

good signal to noise ratio can be measured in a single pulse. The emission spectrum still has to be measured to correct for the background signal (especially since in these types of plasmas line emission and Bremsstrahlung can be very strong [51]), but measurement of the emission spectrum does not require a laser pulse.

For the low density plasma used in this work this method is ineffective. The scattering rate is simply too small to measure a complete scattered spectrum in a single laser pulse. An example of what an acquisition of the total spectrum looks like for a single pulse selected at random can be seen in Figure 6.5. Due to dark current in the CCD chip pixels that do not experience photon arrivals still record a non-zero count value, but this offset is consistent for a given pixel. In this particular laser pulse there are no Thomson photons and only stray/Rayleigh photons arrived at this row of super-pixels in the detector. Even if one or two Thomson photons did arrive, it would be impossible to determine the shape of the electron velocity distribution with such a small amount of signal.

### **6.5.2 Pulse Accumulation**

When the plasma density and temperature are near the detection limit, pulse accumulation methods are used to “build up” a spectrum from a number of laser pulses. This can either be done by integrating on the sensor chip of the detector or by simply summing a sequence of individual acquisitions. The first method is preferable since read noise is only added to the data once, but strong stray light and Rayleigh signal

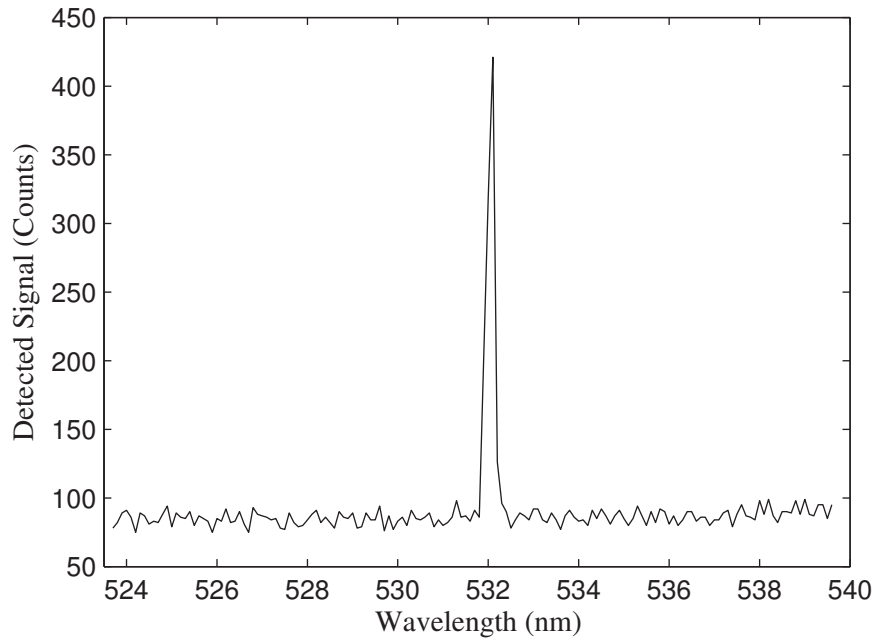


**Figure 6.5:** Acquisition of the total spectrum for a single laser pulse.

usually requires use of a Rayleigh block to prevent the detector from saturating near the laser wavelength when accumulating on-chip. The more pulses that are accumulated the better the signal to noise ratio, which allows the choice of acquisition time to balance the measurement time against signal strength and detection limit needed for the plasma conditions being measured.

The small scattered signal produced in the plume of a Hall thruster combined with the inability of the iCCD used in this work to integrate on-chip makes this method unusable for our system. Read noise from the detector is added at every read-out, so each acquisition contains the full read noise of the detector. Even though the extra read noise is a problem, the main factor limiting determination of the scattered spectrum is the low photon scattering

rate. The procedure for the pulse accumulation method is as follows:

1. All acquisitions taken with both the plasma and laser on are added together pixel by pixel. This results in a single matrix the size of the binned detector face and is the accumulated total spectrum.
2. This process is repeated for the emission and stray light acquisitions.
3. The emission and stray spectra are subtracted from the total spectrum, which should leave only the Thomson spectrum.

An example of the corrected Thomson spectrum produced using the pulse accumulation method applied to the measurements taken in this work can be seen in Figure 6.6. It is immediately clear that something is suspicious about this corrected spectrum since there is a strong negative peak at the laser wavelength. Only the total and stray spectra have strong contributions at this wavelength, so it seems that the stray light signal is stronger than the total signal. What happened in this case is that the stray light measurements were performed first, after which the thruster was turned on and a coating was deposited on the lens. This caused a reduction in the transmission of the collection optics and the stray signal measured during the total spectrum acquisitions was less than during the stray light measurements. The effect this causes on the corrected spectrum will be discussed fully in a later section, but for now we will assume that the stray light contribution is confined to a narrow range around 532 nm. We are then concerned with whether or not we see



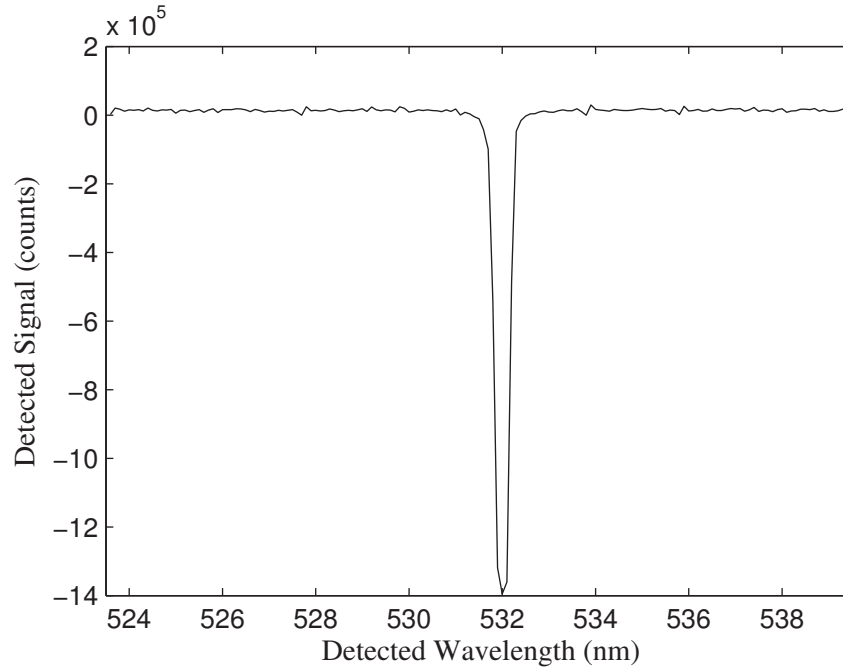


**Figure 6.6:** Sample corrected spectrum as determined by pulse accumulation over 27,000 acquisitions. Thruster conditions were 350 V discharge and 40 SCCM mass flow rate (xenon).

any signal a few nanometers away from the laser wavelength. A zoomed-in version of Figure 6.6 can be seen in Figure 6.7. In this figure there is a great deal of variation pixel to pixel, and the spectrum is essentially flat across all wavelengths (no Thomson spectrum is discernible). This result is not surprising, since the probability of a photon arriving during a single acquisition at any given super-pixel is so low (see section 6.2). Even after tens of thousands of acquisitions there may only be a few photons that arrive at a single super-pixel, but the dark noise and read noise are recorded for every acquisition. The mean value of this noise can be subtracted, but the variance it adds to the spectrum cannot be eliminated. With few photons arriving at the detector the scattered photons do not stand out from the noise using this method.

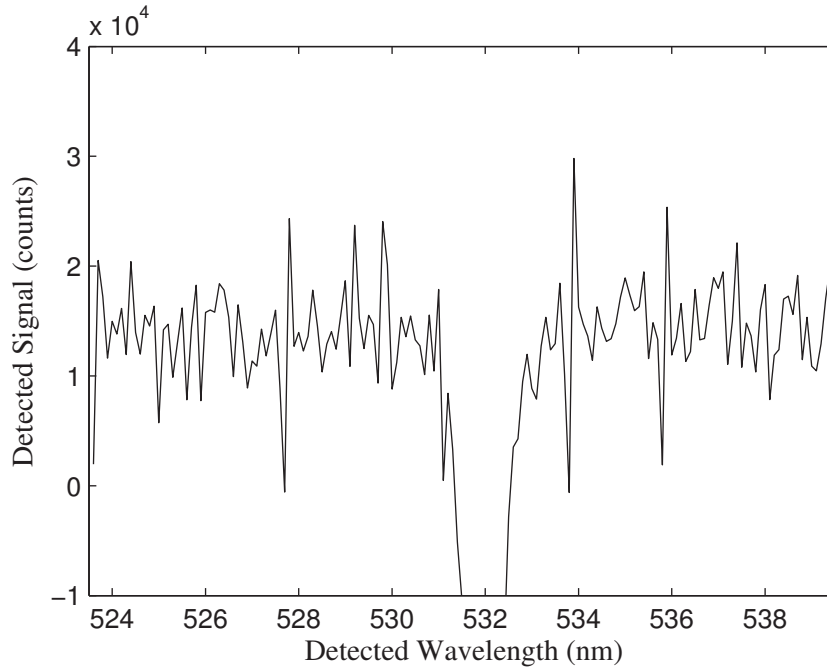


**Figure 6.7:** Sample corrected spectrum at 350 V 40 SCCM zoomed in to the region of interest.

### 6.5.3 Thresholding

In situations where the photons can be distinguished from the noise in the detector thresholding methods can be applied to improve signal detection. The concept behind thresholding is that a limit is set and any events that produce a count values below this limit are considered to be non-events. If the event exceeds the threshold limit it is considered a photon arrival. The iCCD applies gain to photons that arrive at the detector, and this allows events that are produced by real photon arrivals to be distinguished from events that were produced purely by noise sources in the camera. This is possible because the gain supplied by the iCCD is larger than the variance in the noise-generated counts, and while

there is still noise on the count levels produced by real photons, photon arrivals can be clearly distinguished from non-arrivals. Thresholding techniques are commonly used for Thomson scattering measurements, and it is possible to build up a spectrum over many acquisitions that should ideally only contain signal due to real photon detection events.

The scattering data collected at each operating condition was processed using a simple thresholding technique (in addition to a second technique described in a later section). Prior to performing plasma measurements, noise measurements were performed with the spectrograph entrance slit closed. Using these measurements the mean ( $\mu_N$ ) and standard deviation ( $\sigma_N$ ) of the noise are calculated for each individual super-pixel and are stored in new variables. The noise across the detector is not uniform, and the noise parameters are used to perform non-uniformity compensation. The algorithm for processing the data was as follows:

1. A single super-pixel location is selected and a vector containing the count values for all acquisitions is created from the master data matrix.
2. Each value in this vector (the counts detected at that pixel for each acquisition) is compared to the mean value of the noise at that super-pixel plus 4 standard deviations ( $\bar{n} + 4\sigma$ ). Using this value as the threshold ensures that 99.994% of the noise values are removed. If the count level is less than  $\bar{n} + 4\sigma$  the program moves on to the next acquisition in the vector, and if it is higher than  $\bar{n} + 4\sigma$  the program increments a counter variable for that super-pixel, effectively recording a single photon event for

that acquisition.

3. This is repeated for all super-pixels in the master data matrix for both the total, emission, and stray light data sets, as well as the Rayleigh calibration data set.

After each individual spectrum is determined (total, emission, etc.), the stray and emission spectra are subtracted from the total spectrum to give the corrected Thomson scattering spectrum. Extraction of temperature and density from this corrected spectrum will be discussed in section 6.7.2.

Thresholding methods do have one major drawback. Any event above the threshold is considered to be a single photon arrival, and the number of counts recorded by the detector is disregarded. This means that multiple-photon arrival events are incorrectly recorded as a single photon arrival. This is not a significant source of error for the Thomson signal since the probability of multiple photons arriving at a single pixel in a single acquisition is low. However, such incorrect counting can make Rayleigh calibration somewhat complicated since the Rayleigh calibration data is not in the same photon arrival rate regime, with many photons arriving at a super-pixel during each laser pulse. The implications of this are discussed in chapter 7. In order to make full use of the photon arrival information a new data processing method was developed using a maximum likelihood estimation technique described in the following section.

## 6.6 New Method: Maximum Likelihood Estimation

Maximum likelihood estimation (MLE) is one of many methods of estimating the parameters of a distribution <sup>1</sup>. Given a statistical model of the expected distribution of a set of data and a (usually small) measurement sample, MLE provides an estimate of the distribution parameters that have the highest probability of producing the given measurement sample. This method requires detailed knowledge of the statistical nature of the process that is being estimated, and for Thomson scattering measurements the process is rather straight-forward to calculate.

The concept of maximum likelihood estimation was developed by R. A. Fisher in the early 1900's. Fisher actually developed the fundamental principles of maximum likelihood estimation under multiple names with multiple justifications over a period of about ten years [75]. The phrase “maximum likelihood” and the foundations of its current form were published by Fisher in 1922 [76]. Fisher was concerned with the state of theoretical statistics, especially concerning methods of estimating the parameters of an unknown distribution from small measurements of that population, and the accuracy of such estimations. His seminal work differentiated the concept of “likelihood” from probability, while simultaneously demonstrating that maximum likelihood estimates of the parameters of a distribution (called the estimators) satisfy the criterion of sufficiency, which

---

<sup>1</sup>The author would like to thank Brian Thelen, Joel LeBlanc, and John Valenzuela of the Michigan Tech Research Institute (MTRI) for suggesting use of a maximum likelihood estimation method.

states that the statistic chosen to characterize the sample summarizes the whole of the relevant information supplied by the sample [76].

The method of maximum likelihood estimation was a remarkable breakthrough in theoretical statistics, but widespread application was limited initially due to computational difficulty. With the invention of the computer, MLE has become a somewhat standard tool in the arsenal of the practical statistician, and good summaries can be found in many texts on probability and statistics. A brief description of the MLE method will be presented, followed by a more detailed description of the method as it was applied to the scattering data collected for this research.

### **6.6.1 Basics of Maximum Likelihood Estimation**

The ultimate goal of maximum likelihood estimation is to estimate the parameters of a distribution from a sample of data. To begin, one must specify the distribution whose parameters are the object of estimation. Let  $x = \{x_1, x_2, \dots, x_n\}$  represent a set of random measurements from an unknown population. The probability density function that characterizes this unknown distribution can be written generically as  $f(x|\mu)$ , where the function  $f$  represents the probability of measuring the value  $x$ , given the fact that the distribution is known to be characterized by the parameter  $\mu$ . Since the observations  $x_i$  are randomly obtained, they can be considered to be statistically independent, since measuring  $x_1$  in no way affects the future measurements of  $x$ . By definition, for a

statistically independent random variable the probability of obtaining the measurements  $x = \{x_1, x_2, \dots, x_n\}$  can be expressed as the product of the individual probabilities of each measurement [77], given by:

$$f(x = \{x_1, x_2, \dots, x_n\}|\mu) = f_1(x_1|\mu) \cdot f_2(x_2|\mu) \cdots f_n(x_n|\mu) \quad (6.3)$$

where  $\mu$  can take on any value that satisfies the distribution  $f$ .

This statement is predictive in nature, in that it is assumed that if the form of  $f$  and its characteristic parameter  $\mu$  is known, predictions can be made concerning measurements of this distribution. In reality, the problem is reversed in practical statistics. One does not usually know the exact parameters of a distribution, such as the average height of an American boy between the ages of 8 and 12, but it is often the case that a researcher has thousands of actual measurements of boys in this age range. The researcher wants to know what the average height of the entire population of 8-12 year old boys in America is, and she or he only has a small measurement sample from which an estimation of this parameter can be made. Attempts to determine this parameter from a given sample of heights can be thought of as an inverse problem, and this is the domain of the concept of “likelihood”.

In order to determine the solution to this inverse problem, the likelihood function can

be defined by reversing the roles of the data and the distribution parameters [77], yielding:

$$L(\mu|x) = f(x|\mu) = \prod_{i=1}^n f(x_i|\mu) \quad (6.4)$$

In this case the measurements,  $x$ , are considered to be fixed and the value of  $\mu$  is varied while computing the value of  $L$ . The value of  $\mu$  that maximizes this function is the maximum likelihood estimator of  $\mu$ , often written as  $\hat{\mu}$ . Likelihood is very closely related to probability, but Fisher emphasized that likelihood is not probability for the following reasons [76]:

1. Likelihood is not a differential element like a probability, and cannot be integrated.
2. Because likelihood is assigned to a definite measured value and not a range of values, likelihood is not an absolute measure.
3. The sum of all values of likelihood is always infinite.

Maximizing the likelihood function can be computationally difficult. In the previous example the distribution was characterized by only one parameter, but the MLE method works for much more complicated models with multi-parameter distributions. For large samples, calculating the likelihood for each estimate of the characteristic parameters can take a long time. Another problem that often occurs is that when computing the maximum likelihood as written in equation 6.4, one may end up with many very large or very small numbers that must be multiplied. Computers have difficulty handling very large and very



small numbers, so the natural logarithm of the likelihood function is often maximized instead. In this case the convention is to refer to this new function as the log-likelihood, given by:

$$\ln [L(\mu|x)] \quad (6.5)$$

Taking the natural logarithm of the likelihood function greatly compresses the function values making computation much faster (for example,  $\ln 10^{10} = 23.03$ ). Since the logarithm is a monotone transform, the resulting value of the maximum likelihood estimator is the same whether the likelihood or log-likelihood function is maximized.

### 6.6.2 MLE Applied to Laser Thomson Scattering

Maximum likelihood estimation requires a statistical model of the system to which it is being applied. The model must be expressed in terms of a probability distribution to take the place of the function  $f$  introduced in section 6.6.1. Scattering events are random occurrences that happen sparsely in time and very few photons arrive at a single super-pixel during a single acquisition, even over tens of thousands of acquisitions. Such events are well modelled by the Poisson distribution, given by [78]:

$$P(X = x) = \frac{e^{-\mu} \mu^x}{x!} \quad (6.6)$$

where  $X$  is the random variable and  $\mu$  is the characteristic parameter of the distribution. By convention,  $0^0 = 1$  and  $0! = 1$ . For Poisson processes  $\mu$  is both the mean and the variance

of the distribution. In the case of photon scattering,  $\mu$  is the mean number of photons that are scattered per laser pulse and  $P(x)$  is the probability that  $x$  photons are scattered from any single pulse.

Since there are so few photon arrivals, most acquisitions contain only read noise with a normal distribution centered on the mean value of the noise,  $\mu_N$  (in counts), for that super-pixel. When a photon does arrive at the detector it will produce a count value given by  $\mu_N + k\beta$ , where  $k$  is the number of photons arriving during the acquisition time and  $\beta$  is the mean camera gain in counts per photon. There will be some small variation in the count level produced by any given photon due to noise present in the amplification process and noise from sources in the camera (dark noise, read noise, etc.). A sample histogram demonstrating this distribution of counts can be seen in Figure 6.8.

Using knowledge of the noise parameters for the system and the nature of photon arrival the data can be processed in a way that essentially performs advanced photon counting, where multiple photon arrivals are counted accurately. First, the distribution is shifted by subtracting  $\mu_N$  from the count values such that the mean of the count values produced by non-events is zero. Second, all values are divided by the detector gain,  $\beta$ , with the goal of transforming the data from counts into the number of photons that produced that count value. A sample histogram of the data after these operations have been performed can be seen in Figure 6.9. Because there is noise from various sources present in the data the values do not round exactly to integer values (e.g. it appears as if fractional photons are

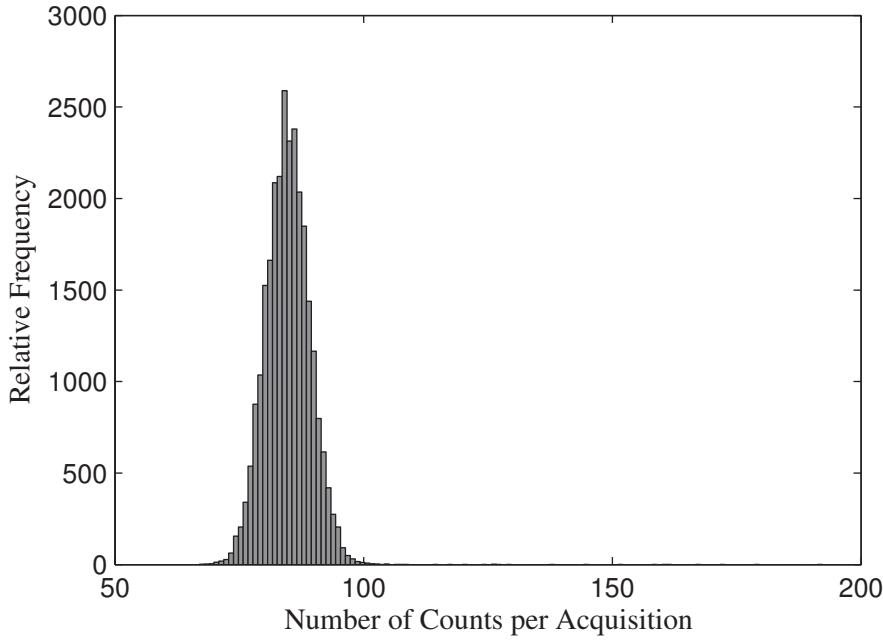


**Figure 6.8:** Histogram of the number of counts detected at a super-pixel during emission spectrum acquisition with an exposure time of 20 ns. This figure demonstrates that most acquisitions contain only read noise centered on the mean of the noise  $\mu_N$ , which is approximately 85 for this data set.

arriving). The variance of the noise is much smaller than  $\beta/2$ , which means that the noise will very rarely cause an event generated by  $k$  photons to appear to have been generated by  $k \pm 1$  photons (a full discussion of this point can be found in section 7.5.1). Knowing this, the data can be rounded to the nearest integer value with confidence that it is the number of photons that produced that count level. The result of this operation can be seen in Figure 6.10.

When the data are processed in this manner the resulting histogram is very similar to a Poisson distribution (described previously) with a very small characteristic parameter  $\mu$  that corresponds to the mean photon arrival rate. If one were to generate a Poisson random

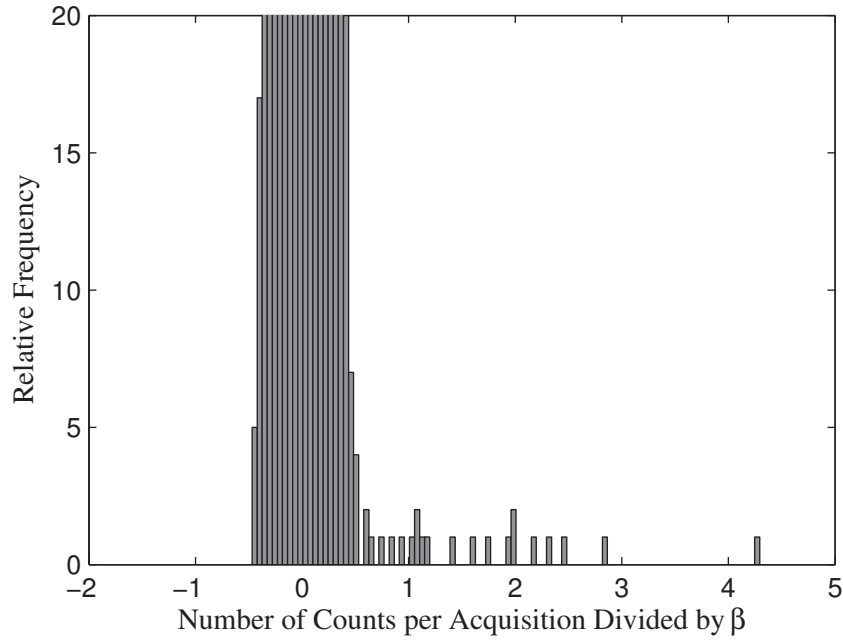


**Figure 6.9:** Histogram of emission data after being shifted by  $\mu_N$  and divided by  $\beta$ .

variable to simulate photon arrivals with  $\mu \ll 1$  and sample it 27,000 times, the result would be mostly zeros corresponding to non-events and very few arrivals corresponding to one or more photons. The transformed data follow this distribution reasonably well and can be fit using a maximum likelihood estimation algorithm with a Poisson model. The resulting maximum likelihood estimator,  $\hat{\mu}$ , provides the most likely arrival rate for the given data, which includes multiple photon events. For the processed data shown in Figure 6.10 the calculated value of  $\hat{\mu}$  is 0.0014 photons per acquisition.

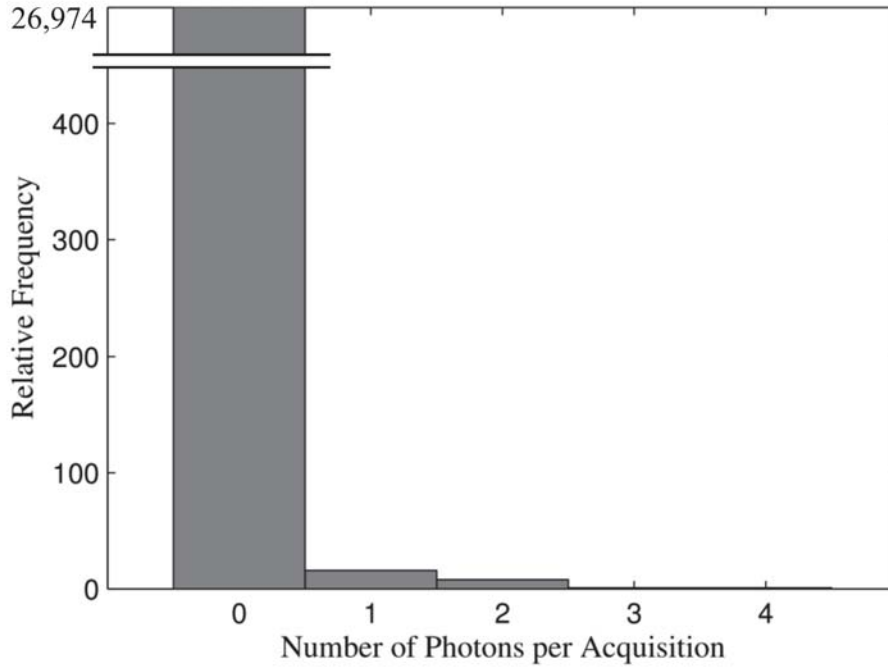


**Figure 6.10:** Histogram of fully processed emission data, zoomed in to clearly display the non-zero bins. The value of  $\hat{\mu}$  determined by maximum likelihood estimation is 0.0014.

## 6.7 MLE Processing Algorithm

Processing of the laser Thomson scattering data is performed using a multi-step algorithm. As described in Section 5.3, the iCCD program stores each individual acquisition as a separate ascii file. Each acquisition for the plasma measurements and the Rayleigh calibration measurements are also stored in individual ascii files as described in section 5.3. These files are loaded into Matlab<sup>®</sup> where they are combined into 3-D matrices containing all of the individual acquisitions. After this pre-processing step there are four matrices containing the total spectrum measurements, the emission spectrum

measurements, the stray light measurements, and the Rayleigh spectrum measurements (for calibration purposes, described later).

The algorithm used to process the data is as follows:

1. A single super-pixel is selected and a vector containing the count values for all acquisitions is created from the master data matrix.
2. The mean value of the noise at this super-pixel,  $\mu_N$  as determined from the pre-recorded noise measurements, is then subtracted from all of the values in order to shift the noise to zero mean.
3. After shifting, all values are divided by the mean detector gain  $\beta$ .
4. All values are then rounded to the nearest integer, which combined with the previous step converts the data from counts to photons.
5. This corrected vector is provided to Matlab's<sup>®</sup> maximum likelihood estimation function and fit with a Poisson distribution. The maximum likelihood estimator,  $\hat{\mu}$ , corresponds to the mean photon arrival rate at that super-pixel.

This process was performed on every super-pixel multiple times, once for each of the spectra sequences measured (total, emission, stray, and Rayleigh). The results of this process are two-dimensional matrices the size of the binned detector that contain the estimated photon arrival for each data set.

### 6.7.1 MLE Spectrum Analysis

As mentioned previously determination of the corrected Thomson spectrum is typically performed by subtracting the emission spectrum and stray spectrum from the total spectrum. This process will be covered step by step, starting with the total spectrum. Figure 6.11 shows the total scattered spectrum determined using the MLE method. A zoomed in version of this spectrum that displays the plasma emission lines can be seen in Figure 6.12. The emission spectrum determined from the data collected with the thruster on and laser off can be seen in Figure 6.13. The stray spectrum taken at the start of the test can be seen in Figure 6.14. If the emission spectrum and stray spectrum are subtracted from the total spectrum (see Figure 6.15) there is a strong negative peak seen previously in section 6.5.2. This strong negative peak at the laser frequency is due to the fact that the stray light data was taken before the test, and during the test a coating of graphite and aluminum was deposited on the lens as a result of sputtering caused by the thruster's ion beam. Figure 6.16 shows a zoomed-in version of Figure 6.15 which demonstrates that subtraction of the unattenuated stray light spectrum from the attenuated total and emission spectra results in a corrected spectrum that is net negative across all wavelengths. Clearly, the stray spectrum cannot be subtracted from the total spectrum without losing the Thomson spectrum, but the effect this will have on the corrected spectrum must be quantified.

In order to determine the effect that the stray light has on the Thomson spectrum the redistribution level of the spectrograph must be determined. The stray light redistribution

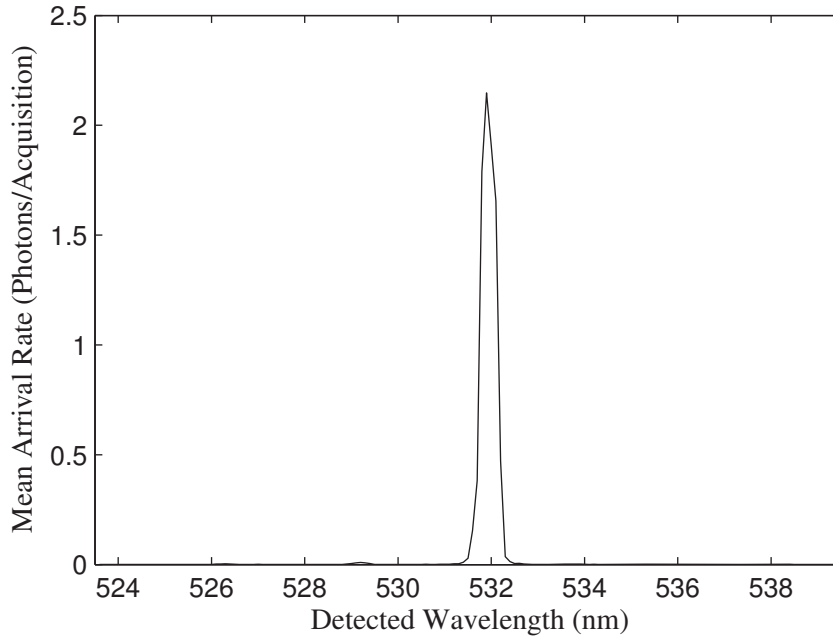


**Figure 6.11:** Total spectrum determined by the MLE method. Thruster conditions: 350 V, 40 SCCM anode mass flow.

level is given by the normalized instrument function of the spectrograph-camera system, given by [15]:

$$\int_0^{\infty} f(\lambda - \lambda_0) d\lambda = 1 \quad (6.7)$$

where  $f(\lambda - \lambda_0)$  is the instrument function centered at  $\lambda_0$ . A plot of the instrument profile of the spectrograph-camera system used in this work can be seen in Figure 6.17. The stray light redistribution level shown in Figure 6.17 is quite good, but we need to calculate the ratio of Thomson scattered light and redistributed stray light in order make sure that the redistributed stray light will not overpower the Thomson signal. The stray light level for the scattering system used in this work was equivalent to Rayleigh scattering on  $N_2$  gas with a density of  $2.04 \times 10^{22} \text{ m}^{-3}$ . A velocity distribution must be assumed for the electrons and



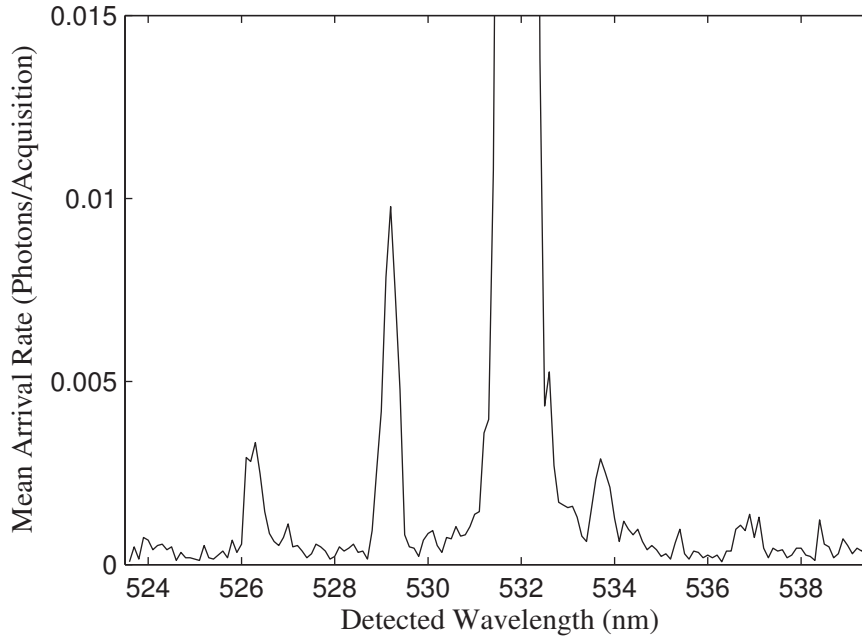


**Figure 6.12:** Total spectrum determined by the MLE method, zoomed-in to clearly show the plasma emission lines. Thruster conditions: 350 V, 40 SCCM anode mass flow.

for convenience we will assume that the electrons in the plasma are thermalized, implying that the Thomson spectrum is Gaussian in shape. The ratio of the Thomson scattered power to the redistributed light power can then be expressed as [15]:

$$\frac{P_T}{P_R} = \frac{0.3}{R} \cdot \frac{n_e}{n_{N_2}} \cdot \frac{d\sigma_T/d\Omega}{d\sigma_R/d\Omega} \quad (6.8)$$

where  $R$  is defined as the redistribution level of the system,  $n_e$  is the electron number density,  $n_{N_2}$  is the calibration gas number density (nitrogen), and  $d\sigma_T/d\Omega$  and  $d\sigma_R/d\Omega$  are the differential Thomson and Rayleigh scattering cross-sections, respectively.

We can now calculate the Thomson to stray light ratio for a range of plasma conditions

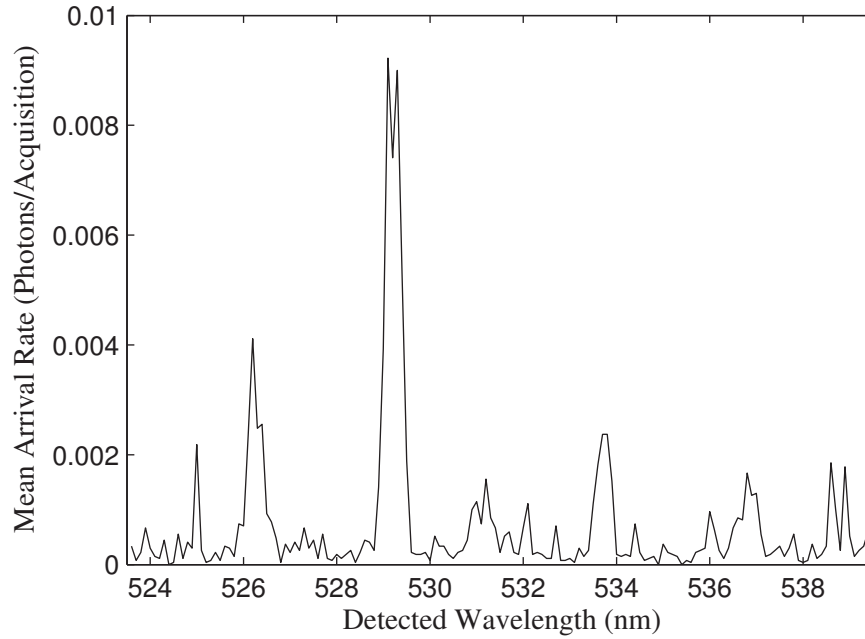


**Figure 6.13:** Emission spectrum determined by the MLE method. Thruster conditions: 350 V, 40 SCCM anode mass flow.

and see how much effect the stray light will have. To begin, we assume an electron density of  $1 \times 10^{17} \text{ m}^{-3}$  and an electron temperature of 1 eV. Using these values we calculate that the  $\Delta\lambda_{1/e}$  width for a temperature of 1 eV is approximately 1.5 nm. The stray light redistribution level at  $\Delta\lambda = 1.5 \text{ nm}$  is approximately  $4.5 \times 10^{-5}$ , indicating a Thomson to stray light ratio of 4.27. This level is not tremendous, but clearly sufficient to detect the Thomson signal. Previous probe measurements of electron temperature in the near-field plume of the thruster used in this work indicated temperatures of approximately 5 eV, and if we use this new temperature value we find that the Thomson to stray light ratio increases to 24. If we also increase the electron density to  $5 \times 10^{17} \text{ m}^{-3}$  we find that the ratio increases to over 120, and the stray light contribution to the Thomson spectrum is negligible.

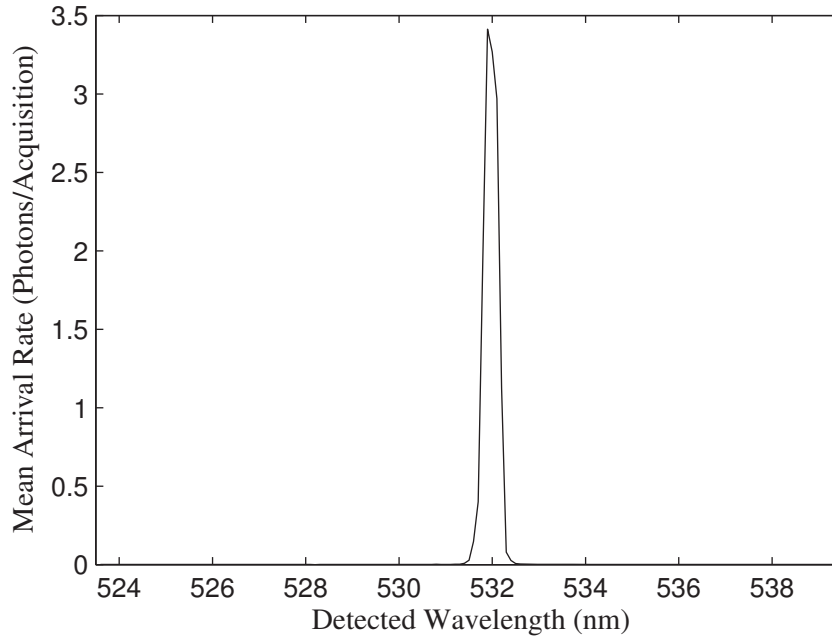


**Figure 6.14:** Stray light spectrum determined by the MLE method. Data acquisition was performed with the thruster off prior to the test.

We have established that the stray light redistribution of the spectrograph good enough that for electron temperatures above 1 eV and electron densities above  $1 \times 10^{17} \text{ m}^{-3}$  the contribution of stray light is low to negligible. In general, the higher the temperature and density the less the redistributed stray light matters. Since we cannot accurately subtract the stray light contribution from the total spectra obtained in this work, the corrected Thomson spectra will be determined by subtracting the emission signal from the total signal and simply masking (in software) the center of the spectrum which is contaminated by stray light. The mask covers a 2 nm range ( $\pm 1 \text{ nm}$  from 532 nm), which covers the range at which the Thomson to stray light ratio is less than 2 for an electron temperature of 0.5 eV and electron density of  $1 \times 10^{17} \text{ m}^{-3}$ . This temperature and density combination is

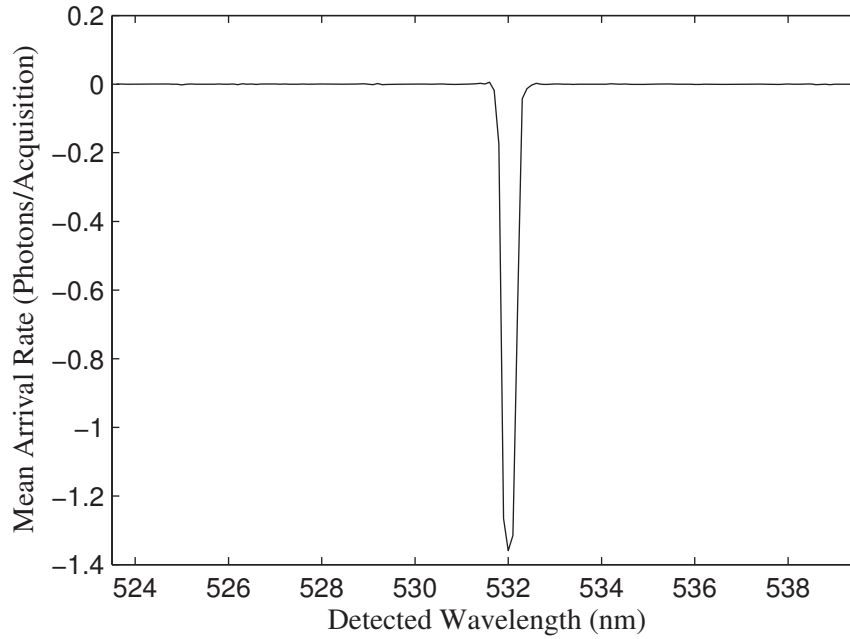


**Figure 6.15:** Corrected spectrum determined by the MLE method (emission and stray spectra subtracted from the total).

considered to be a practical minimum, and for higher temperatures and densities only a small fraction of the usable portion of the Thomson spectrum will be excluded from data processing.

### 6.7.2 Determination of Electron Temperature and Density

Now that the method of obtaining and processing the scattered signal has been established, the extraction of electron temperature and density from the scattered spectra can now be discussed. As was previously mentioned, the Thomson scattering spectrum is a direct measurement of the electron velocity distribution function along the scattering vector in the plasma. In theory, any deviations from a Maxwellian distribution in the plasma will

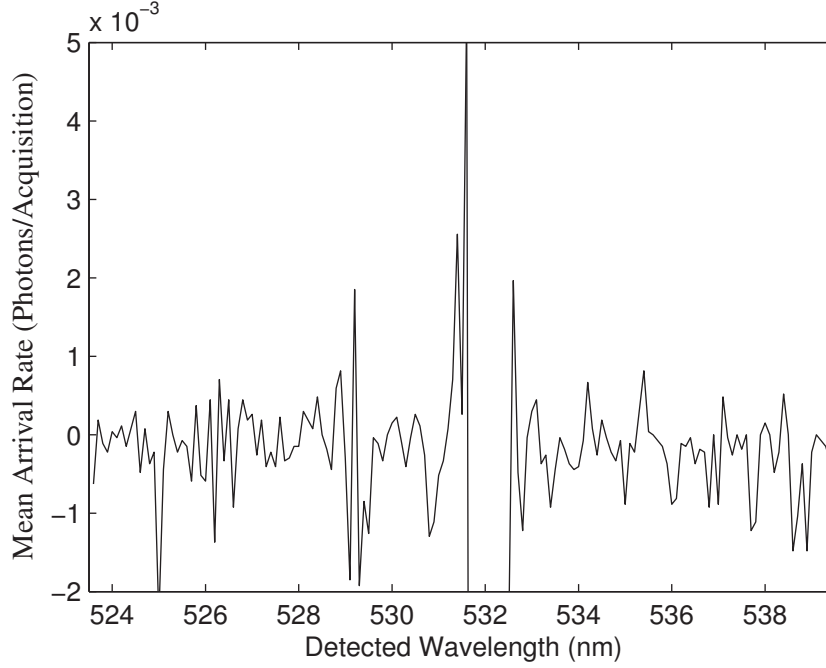


**Figure 6.16:** Corrected spectrum determined by the MLE method (emission and stray spectra subtracted from the total), zoomed-in to show net-negative values.

be visible in the shape of the spectrum, but the scattered signal obtained in this work was extremely weak and low SNR made it impossible to say with certainty that the electron velocity distribution deviated from Maxwellian. Because of this, a Maxwellian distribution was assumed and a non-linear least-squares Gaussian fit was performed on the corrected scattering spectrum <sup>2</sup>. The determined value of  $\sigma$  was used to calculate the  $1/e$  width according to the following equation:

$$\Delta\lambda_{1/e} = \sqrt{2\sigma^2}. \quad (6.9)$$

<sup>2</sup>In certain cases making this assumption allows processing of the data in a new way (See Appendix B).

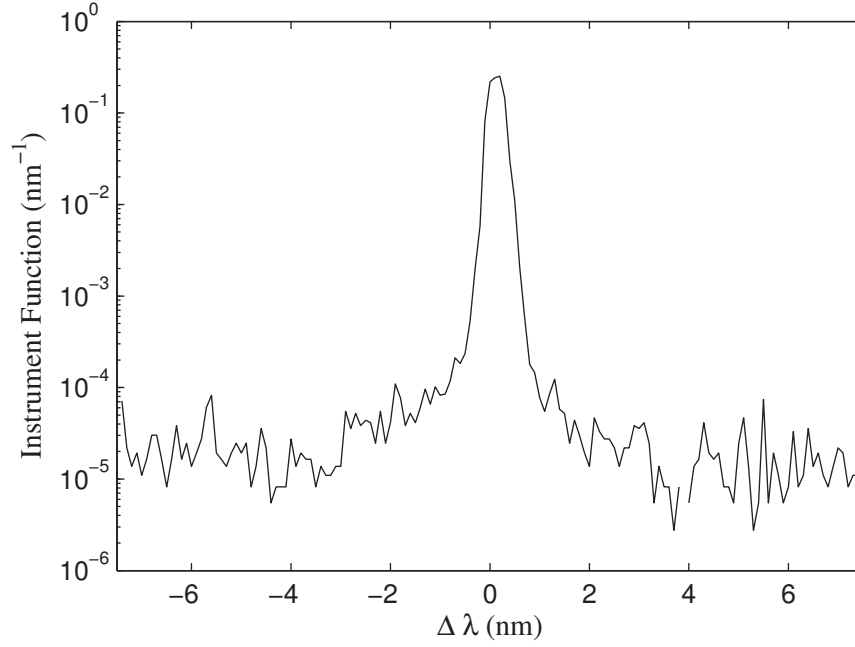


**Figure 6.17:** Measured instrument function of the Spex 1877C-AG used in this work.)

This value was then substituted into equation 3.21, which can also be expressed (for our particular dispersion and binning) as:

$$T_e = 0.00905 \cdot \sigma^2 \quad (6.10)$$

where  $T_e$  is in eV and  $\sigma$  is in super-pixels. Six rows of data (described in section 5.3) are fitted in this way, and the resulting values of electron temperature are averaged to obtain the final value. This averaging of six rows corresponds to taking a spatial average along the beam over a length of approximately 0.5 mm, which is much better spatial accuracy than the electrostatic double probe can provide. An example of a corrected spectrum and corresponding fit can be seen in Figure 6.18.

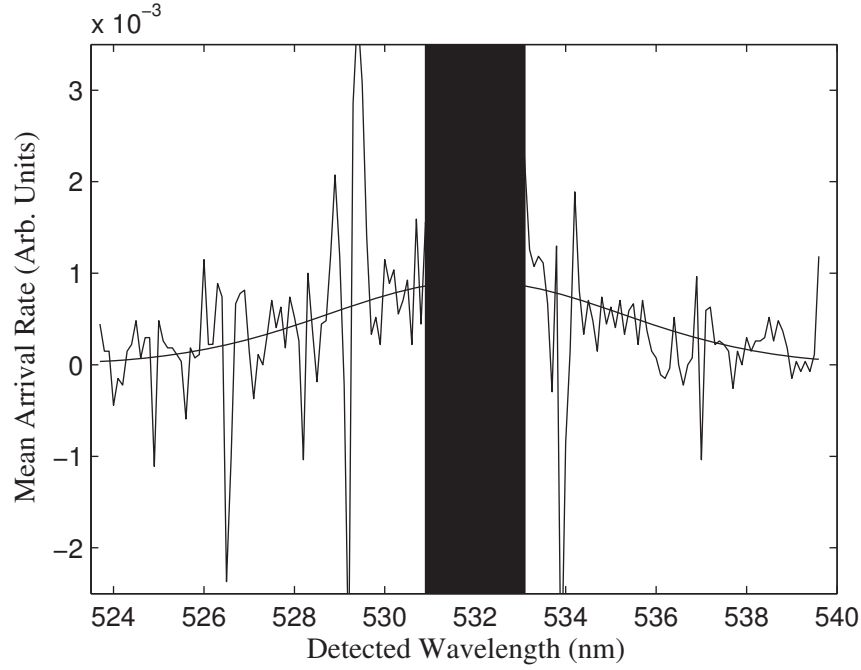


**Figure 6.18:** Corrected Thomson scattering spectrum as determined using the maximum likelihood estimation technique. Thruster was operating at 300 V 40 SCCM, and the Gaussian fit indicates an electron temperature of 9.6 eV and density of  $7.1 \times 10^{17} \text{ m}^{-3}$ .

The density is determined according to equation 5.2 given in Chapter 5, repeated here for reference:

$$n_e = n_R \frac{\sigma_R}{\sigma_T} \frac{P_T}{P_R} \frac{\int_{\lambda} I_T}{\int_{\lambda} I_R}. \quad (6.11)$$

The laser power is the same during measurement of both the Rayleigh and Thomson spectra, so the ratio of power terms is one. The cross-sections for Thomson and Rayleigh scattering are known constants and the number density during Rayleigh calibration can be calculated using:

$$n = \frac{p}{k_B T} \quad (6.12)$$

where  $p$  is the neutral gas pressure during Rayleigh calibration,  $k_B$  is Boltzmann's constant, and  $T$  is the temperature of the calibration gas ( $N_2$ ). The integral of the Rayleigh spectrum is performed numerically, and for the Thomson spectrum the integral is calculated from the amplitude and standard deviation of the fit to the spectrum. The density is calculated using the integrated values for each row, then the densities from each row are averaged.

### 6.7.3 Advantages of MLE

Using the maximum likelihood estimation technique with the detailed probability density function for the scattering has key advantages over simple thresholding methods such as photon counting. Most importantly, all information about the photon arrival is preserved. This is especially important in situations where multiple photons arrive at the same super-pixel during a single acquisition. When applying thresholding methods to pixels that have received multiple photons, two or more photons are counted as only one. For the conditions in this work the photon arrival rate is exceptionally low, but because the detector is binned into large super-pixels there are multiple photon arrival events that are accurately accounted for using maximum likelihood methods. Incorrect counting can lead to underestimates of the photon arrival rate, and give an inaccurate picture of the distribution.

Another related advantage of maximum likelihood estimation over thresholding methods is accuracy in density estimates. When performing Thomson scattering



measurements calibration with Rayleigh scattering is necessary for absolute measurements of density. As was discussed previously in this chapter, even for short measurement times of 20 ns the photon flux at the laser wavelength is much higher than the photon arrival rate for the Thomson scattered electrons. Applying thresholding techniques to Rayleigh calibration data leads to significant under estimation of the photon flux which leads to an overestimation of the electron density. The maximum likelihood estimation technique used in this work adapts to all levels of photon flux, and thus gives a much more accurate estimate of electron density.

# **Chapter 7**

## **Near-Field Plume Measurements**

### **7.1 Introduction**

The purpose of this chapter is to report and compare measurements of electron temperature and density in the near-field plume of a Hall thruster using multiple techniques. The results of processing the laser Thomson scattering measurements with both the thresholding and maximum likelihood estimation methods will be presented. These results will also be compared to electrostatic probe measurements taken at the same location in the plume. Comparing the plasma properties determined by laser measurement to the properties determined by electrostatic probes will serve to validate the laser measurements against an accepted method.

## 7.2 Experimental Parameters and Test Matrix

For this work both laser and probe measurements of temperature and density were performed at a variety of operating conditions. When operating the thruster a specific discharge voltage and mass flow rate was chosen. After starting the mass flow at the selected discharge voltage the anode begins to draw electron current. The magnet current is then increased, causing the discharge current to decrease from its initial value. As the magnet current is increased the discharge current will decrease until it reaches a minimum, after which the discharge current increases with increasing magnet current. Tuning the magnetic field consists of minimizing the discharge current for a given mass flow, and when running mass flow limited the discharge current is nearly constant for a given mass flow rate, largely independent of discharge voltage.

The discharge voltage and propellant mass flow rates along with the order of measurement is specified in Table 7.1. This test matrix spans a range of discharge voltages and mass flow rates typical for Hall thruster operation. For all thruster operating conditions the cathode was operated at a mass flow rate of 5 SCCM of xenon, with 0.5 A of current drawn by the keeper. The discharge current at each operating condition and the magnet current required to minimize the discharge current can be seen in Figures 7.2 and 7.3, respectively. The measured pressure in the vacuum chamber during each measurement can be seen in Table 7.4.

**Table 7.1**  
Test Matrix with Measurement Order

Mass Flow (SCCM)	Discharge Voltage (V)				
–	250	300	350	400	450
40	–	1	6	4	–
50	–	5	3	8	–
60	13	9	2	7	11
70	–	–	12	–	–
80	–	–	10	–	–

**Table 7.2**  
Discharge current (A) for each operating condition.

Mass Flow (SCCM)	Discharge Voltage (V)				
–	250	300	350	400	450
40	–	3.40	3.34	3.34	–
50	–	4.40	4.30	4.24	–
60	5.30	5.27	5.30	5.20	5.27
70	–	–	6.25	–	–
80	–	–	7.40	–	–

**Table 7.3**  
Magnet current (A) for each operating condition.

Mass Flow (SCCM)	Discharge Voltage (V)				
–	250	300	350	400	450
40	–	3.00	3.00	3.00	–
50	–	3.25	3.25	3.25	–
60	3.00	3.00	3.75	4.00	5.00
70	–	–	4.50	–	–
80	–	–	5.00	–	–

**Table 7.4**  
Background pressure (  $\times 10^{-5}$  Torr) for each operating condition.

Mass Flow (SCCM)	Discharge Voltage (V)				
–	250	300	350	400	450
40	–	1.60	3.30	1.70	–
50	–	7.30	2.00	2.00	–
60	2.40	2.80	2.20	2.50	2.20
70	–	–	2.50	–	–
80	–	–	2.90	–	–

## 7.3 Electron Temperature Measurements

The results of electron temperature measurements will be presented in the following subsections. All measured values in the test matrix will be presented for each processing method. The results for each method will be discussed individually, after which the results for all three methods will be compared to one another.

### 7.3.1 Probe Results

The first set of results that will be discussed are the double probe measurements, since electrostatic probes are the accepted method of measuring plasma temperature and density in Hall thruster plasmas. Measured electron temperature for each operating condition can be seen in Table 7.5. The electron temperature in the near-field plume varied little with discharge conditions. Electron temperature was not expected to exhibit dependence on the mass flow rate, but it was somewhat surprising to see that the discharge voltage had minimal effect on the measured electron temperature. The measurement position was located 10 mm downstream of the thruster exit plane which should be outside of the acceleration zone for all discharge voltages, but a slight dependence was still expected based on internal fast-probe measurements of a Hall thruster taken by Raitses et. al. [5]. The geometry of the thruster used in that study was quite different than the thruster used for this work, but the general result was expected to hold.

**Table 7.5**

Electron temperature in eV as measured by electrostatic double probe.

Mass Flow (SCCM)	Discharge Voltage (V)				
–	250	300	350	400	450
40	–	8.08	7.40	6.43	–
50	–	7.02	6.85	8.97	–
60	7.38	7.49	7.32	7.85	6.42
70	–	–	7.31	–	–
80	–	–	6.73	–	–

### 7.3.2 Thresholding Results

The next technique that will be discussed is the thresholding method. Raw electron temperature for each operating condition can be seen in Table 7.6. It is immediately clear that some of the values determined by this method are nonsensical. As was discussed in Chapter 6, the data analysis algorithm calculates the electron temperature and density on a row-by-row basis and then averages the values for each row. If one row fails to converge to a reasonable value it can dominate and generate a meaningless value for the average. An example of a such a line can be seen in Figure 7.1. Since there appears to be no Thomson spectrum visible the fitting algorithm determines that if the spectrum is Gaussian the width parameter,  $\sigma$ , must be enormous. For the sample plot in Figure 7.1 the value of  $\sigma$  is  $1.62 \times 10^8$ . For lack of better, compact terminology these lines will be referred to simply as “low-signal lines”.

While there are occasionally low-signal lines after processing the data, these lines are usually very obvious and are simple to remove from the average used to determine the

**Table 7.6**  
Raw electron temperature in eV as determined using the thresholding method.

Mass Flow (SCCM)		Discharge Voltage (V)				
	–	250	300	350	400	450
40	–		6.93	13.6	25.9	–
50	–		11.3	9.55	327	–
60	0.14		$4.73 \times 10^{11}$	25.9	25.5	$4.34 \times 10^{20}$
70	–		–	19.1	–	–
80	–		–	41.1	–	–

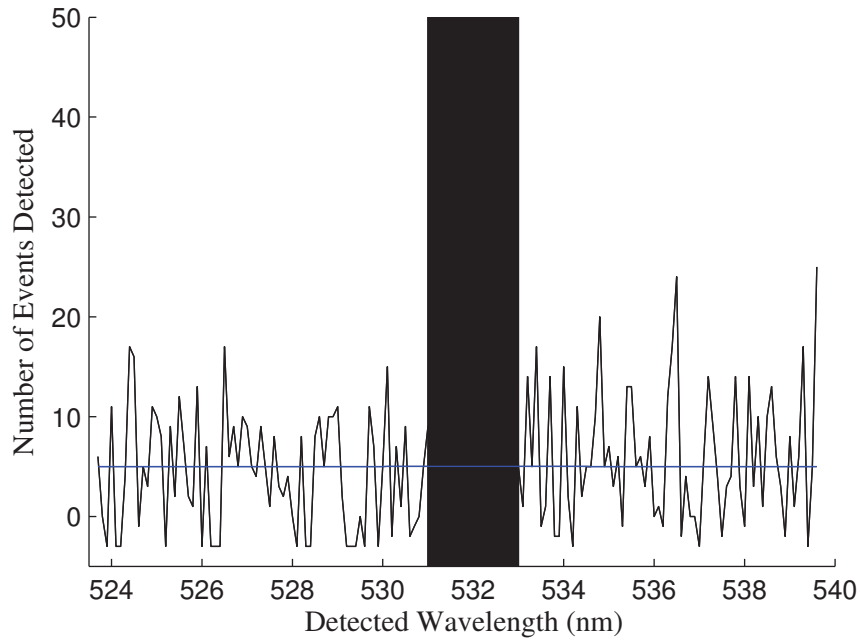


**Figure 7.1:** Example of a low-signal line and the corresponding fit using the thresholding method.

electron temperature. For the case just discussed, the one low-signal line had a value of  $\sigma$  that was 6 orders of magnitude larger than all of the other lines. Sometimes low-signal lines are less obvious, and in either case a rigorous method of testing and eliminating low-signal lines is required. The well-established Peirce criterion [79] was used to determine which



**Table 7.7**

Corrected electron temperature in eV as determined using the thresholding method. The number of lines that were removed (if any) are in parentheses.

Mass Flow (SCCM)		Discharge Voltage (V)				
	–	250	300	350	400	450
40	–	–	6.93	10.5 (1)	20.7 (1)	–
50	–	–	11.3	9.55	55.1 (1)	–
60	–	0.25 (3)	41.3 (3)	15.6 (1)	25.5	26.4 (4)
70	–	–	–	19.1	–	–
80	–	–	–	32.7 (1)	–	–

lines (if any) needed to be removed after the data was processed with both the thresholding and maximum likelihood estimation methods. For the data set corresponding to the 300 V 60 SCCM operating condition there are two low-signal lines, and removing these lines yields a corrected temperature of 43.1 eV instead of  $4.73 \times 10^{11}$  eV. The corrected electron temperature determined after removing low-signal lines can be seen in Table 7.7.

The values in Table 7.7 are much more reasonable in general, but it is very noticeable that the correspondence with the probe data is not strong. An obvious anomaly is the calculated temperature at the 250 V 60 SCCM condition. All six lines contained very little signal at this operating condition, and a sample spectrum and fit (single row) from this operating point can be seen in Figure 7.2. For unknown reasons the least-squares fit applied to this data set produced a very low estimate of electron temperature instead of the usual failure mode of an exceptionally large temperature estimate. This anomaly occurred only at this operating condition.

In general it appears that temperatures in the upper left portion of Table 7.7 are

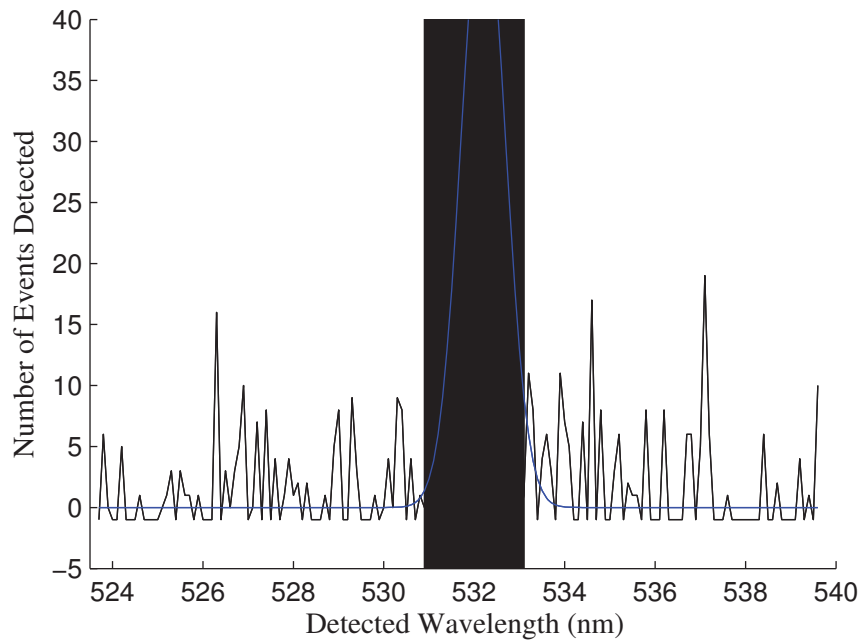


**Figure 7.2:** Second example of a low-signal line and the corresponding fit using the thresholding method. Thruster conditions were 250 V discharge and 60 SCCM mass flow rate.

somewhat similar to the probe measurements, while the temperatures in the lower right portion of Table 7.7 are significantly higher. Given the order in which the measurements occurred it does not appear to be a systematic measurement effect. It is possible that as the voltage was increased the acceleration zone increased in distance from the anode. If this was the case it is possible that laser scattering from the hotter electrons on the edge of the acceleration region was detected.

**Table 7.8**

Raw electron temperature in eV as determined using the MLE method.

Mass Flow (SCCM)		Discharge Voltage (V)			
–	250	300	350	400	450
40	–	5.93	28.0	27.9	–
50	–	8.46	9.72	30.4	–
60	1.01	$4.03 \times 10^{13}$	$5.77 \times 10^9$	19.1	$7.12 \times 10^{10}$
70	–	–	$8.78 \times 10^6$	–	–
80	–	–	24.4	–	–

### 7.3.3 MLE Results

The maximum likelihood estimation technique was then applied to the same data set. Raw electron temperature for each operating condition can be seen in Table 7.8. Like the thresholding method, there are several operating conditions at which the electron temperatures are clearly nonsensical as determined by the MLE method when using the averaged parameters for all six lines. Peirce's criterion was applied to the processed data in order to remove outliers from the results. A sample of a low-signal line determined by the MLE method can be seen in Figure 7.3. For comparison, a sample of a good line from the 300 V 40 SCCM data set can be seen in Figure 7.4. In this particular spectrum (corresponding to a spatial average over approximately 0.1 mm of the scattering volume) there is a large amount of subtraction noise located at the  $\text{Xe}^{2+}$  lines in the vicinity of 532 nm, but this noise is well localized spectrally and has minimal effect on the fit to the spectrum.

The corrected values of electron temperature after removal of low-signal lines can be

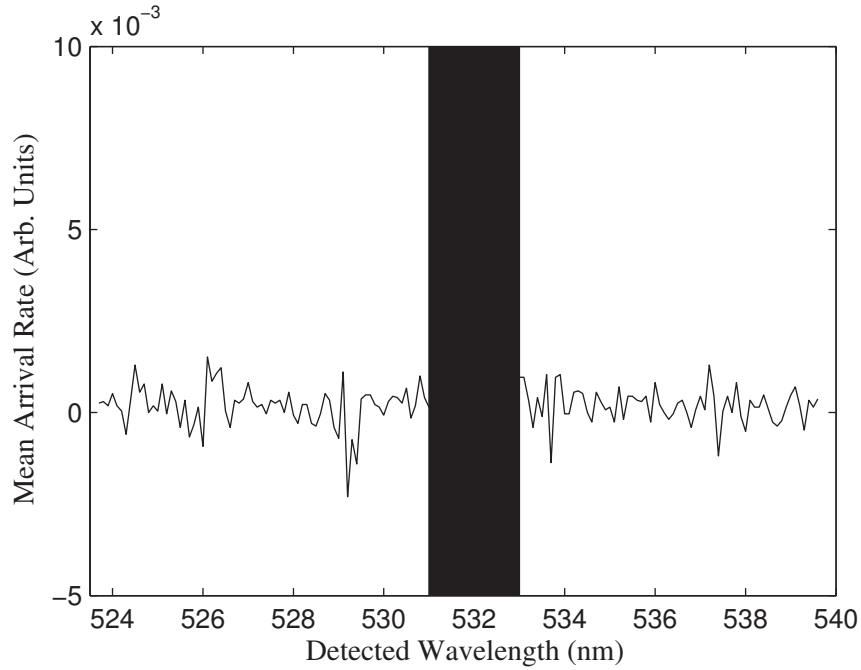


**Figure 7.3:** Example of a low-signal line as processed by the MLE method. Thruster conditions were 300 V discharge and 60 SCCM mass flow rate.

**Table 7.9**

Corrected electron temperature in eV as determined using the MLE method. The number of lines that were removed (if any) are in parentheses.

Mass Flow (SCCM)	Discharge Voltage (V)				
	250	300	350	400	450
40	–	5.93	9.48 (1)	12.2 (1)	–
50	–	6.87 (1)	6.57 (1)	22.1 (1)	–
60	1.01	12.1 (2)	3.31 (2)	19.1	47.4 (2)
70	–	–	13.6 (2)	–	–
80	–	–	21.0 (1)	–	–

seen in Table 7.9. Trends in the MLE processed data are more similar to the thresholding results than the probe results. The discharge voltage seems to have the expected effect on the electron temperature, with the electron temperature increasing with increased discharge voltage. Mass flow rate does not seem to have a correlation with the electron temperature.

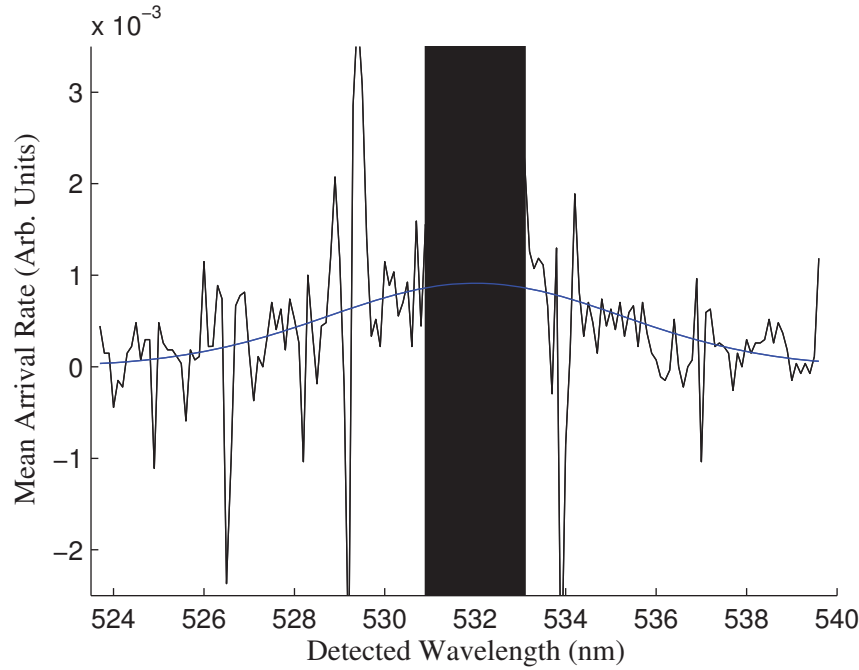


**Figure 7.4:** Example of a good line as determined by the MLE method. Thruster conditions were 300 V discharge and 40 SCCM mass flow rate.

### 7.3.4 Comparison of Temperature Measurements

Each of the methods produces a matrix of temperature estimates with different characteristics. The defining feature for the electron temperatures determined by the double probe is that the entire matrix is relatively flat. One would expect the temperature to increase with discharge voltage and the density to increase with mass flow rate, but these trends were not observed. With the exception of the 300 V 40 SCCM operating condition all of the probe traces conformed very well to the expected hyperbolic tangent shape. Trace fits were especially good in the range of low probe-to-probe voltage, which is the region of the curve where the electron temperature is determined. All probe traces and corresponding

fits can be found in Appendix A.

The corrected electron temperatures determined by the thresholding method have a very different character. For one, several low-signal lines were present and needed to be removed. Even after removal of these lines the table seemed to be split into two sections: one with reasonable estimates of temperature that were slightly higher when compared to the probe measurements, and one with very high estimates of electron temperature that were as much as three times higher than the probe estimates. This break is almost a vertical line between 350 V and 400 V, with the exception of the 350 V 80 SCCM and 300 V 60 SCCM operating conditions.

Corrected electron temperature determined using the maximum likelihood estimation method seems to be compromise between agreement with the double probe and agreement with the thresholding method. At discharge voltages of 300 V and 350 V most of the temperature estimates are similar to the double probe values. The temperature estimates increase at higher voltages, which was seen in the thresholding data but not seen in the double probe data. There is also a somewhat suspicious electron temperature value at the 350 V 80 SCCM operating condition. It is unknown what would cause the electron temperature to rise so drastically at this mass flow rate with no change in discharge voltage. The thresholding method also produced a very large temperature estimate at this operating condition, which may indicate a defect in the laser data.

A comparison of electron temperature versus mass flow rate at a discharge voltage of

350 V for all three methods can be seen in Figure 7.5. The error bars were calculated from the residuals of the fits to the data and the calculated covariance matrix using Matlab's<sup>®</sup> *nlparci* function (and some additional processing to combine the errors for each line) [80]. Error bars correspond to one  $\sigma$  of confidence such that the proper way to interpret the MLE temperature estimate at 350 V and 70 SCCM in Figure 7.5 is  $13.6 \pm 6.4$  eV. It is important to note that these error bars are indicative of the uncertainty in the fits to the data, and are not a measure of accuracy (which will be discussed in section 7.5). All subsequent error bars displayed in this work adhere to this convention. This slice contains the 350 V 80 SCCM operating condition where both the thresholding method and the MLE method produced very high estimates of electron temperature.

All three methods possess different trends with respect to mass flow rate. The thresholding method shows a steady increase in electron temperature with flow rate. The probe measurements show no correlation between mass flow rate and temperature. At lower flow rates the MLE method shows a decrease in electron temperature, but then temperature increases at the higher flow rates. The thresholding method consistently produces temperature estimates higher than both the probe and MLE methods. All three methods agree well at the 40 and 50 SCCM flow rates but deviate significantly at 60 SCCM and above. At 60 SCCM the thresholding value is twice as large as the probe and MLE values, but the uncertainty in the thresholding value is enormous at this flow rate. Using the probe values as a reference the thresholding method values are higher by approximately 40 percent at 40 and 50 SCCM, and rapidly increase to 4 times the probe value at 80 SCCM.

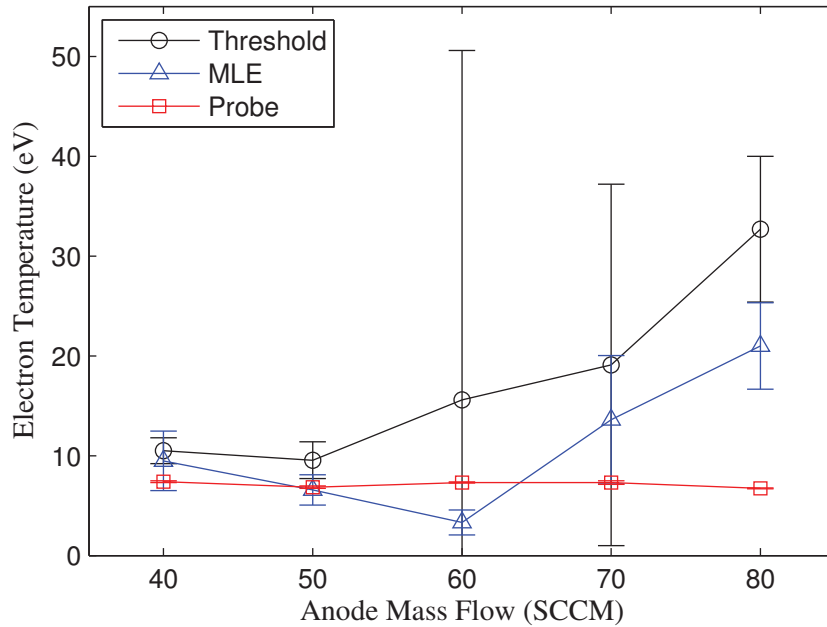


**Figure 7.5:** Comparison of electron temperature measurements vs. mass flow rate at a fixed discharge voltage of 350 V.

The MLE method produced temperature estimates that were somewhat closer in magnitude to the probe measurements, with variations ranging from less than 5 percent at 50 SCCM to approximately 85 percent at 70 SCCM. At a flow rate of 80 SCCM the MLE method produced a temperature estimate more than twice as high as the probe.

A comparison of electron temperature versus discharge voltage for a fixed mass flow rate of 60 SCCM can be seen in Figure 7.6. Once again, each method has a very different character. The thresholding method shows no clear trend, and the uncertainty in the values are large. Probe measurements are very flat, exhibiting minimal variation as a function of discharge voltage. The MLE values show a general increase in electron temperature as a function of discharge voltage, which was expected but not seen in the



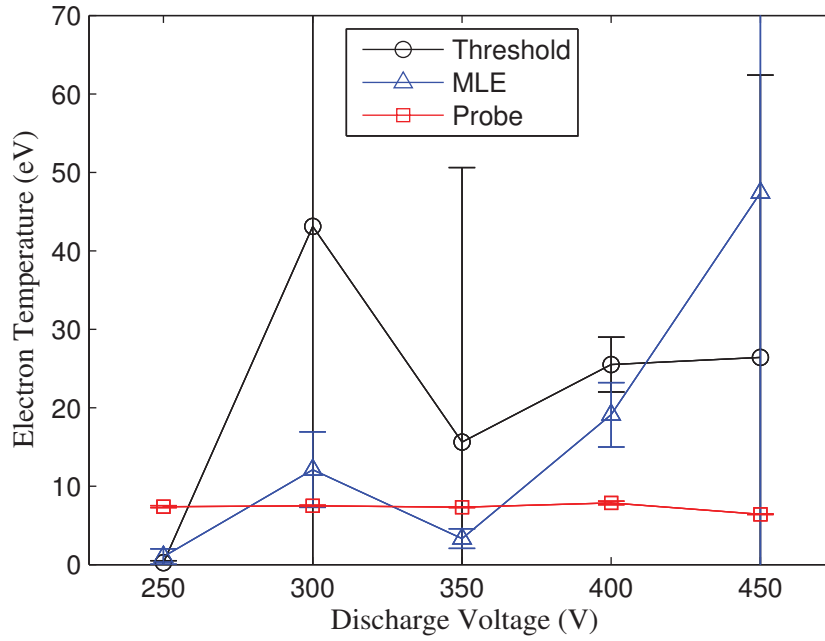


**Figure 7.6:** Comparison of electron temperature measurements vs. discharge voltage at a fixed mass flow rate of 60 SCCM.

probe measurements. The laser data taken at the 250 V 60 SCCM operating condition produced very low temperature estimates with both the thresholding and MLE methods (below the detection capability of the LTS diagnostic), and the values at this operating condition must be discarded. Similarly, both laser methods produced high estimates of electron temperature at the 400 V and 450 V operating conditions, whereas the probe method did not. The size of the error bars at the 450 V operating condition indicates that the values produced by both laser methods are highly suspect.

This comparison of electron temperature measurements has displayed some of the key features of the results produced by the different data processing methods employed in this work. Electrostatic probe measurements are considered to be the standard method

of determining electron temperature, and using the double probe method produces a measurement matrix that is very flat with no trends with respect to discharge voltage or mass flow rate. The thresholding method produces values that are reasonably close to both the probe and MLE methods at lower discharge voltages, but the values at higher discharge voltages tend to be more similar to the values determined by the MLE method. The MLE method shows an increase in electron temperature with discharge voltage at all flow rates, whereas the thresholding method shows a decrease in electron temperature at 350 V at all flow rates.

## **7.4 Plasma Density Measurements**

The results of plasma density measurements will be presented in the following subsections. Presentation will follow the form taken for the electron temperature data discussed previously. The results for each method will be discussed individually, after which the results for all three methods will be compared to one another.

### **7.4.1 Probe Results**

Plasma density calculated from the double probe measurements can be seen in Table 7.10. Details of how the density is calculated from a probe trace can be found in section 4.3.2. Density ranged from approximately  $7 \times 10^{17} \text{ m}^{-3}$  to  $1.3 \times 10^{18} \text{ m}^{-3}$ . This range agrees fairly well with previous fast-probe measurements performed by Haas [4] on a similar

**Table 7.10**  
Electron number density ( $\times 10^{18} \text{ m}^{-3}$ ) as measured by electrostatic double probe.

Mass Flow (SCCM)	Discharge Voltage (V)				
–	250	300	350	400	450
40	–	0.67	1.15	0.79	–
50	–	0.81	0.80	0.86	–
60	0.88	1.14	0.82	1.06	0.80
70	–	–	1.02	–	–
80	–	–	0.81	–	–

thruster, where plasma density of approximately  $3 \times 10^{17} \text{ m}^{-3}$  was measured at similar discharge power. Like the electron temperature, the plasma density measurement matrix is relatively flat and does not exhibit any clear trends with respect to the discharge parameters. It was expected that the plasma density at the measurement point would increase with increased mass flow rate, but this trend was not seen.

### 7.4.2 Thresholding Results

The raw plasma density for each operating condition can be seen in Table 7.11. It is clear from this table that the average value of plasma density is strongly affected by including low-signal lines in the average. When determining the density the area under the curve is determined by assuming that the spectrum is Gaussian and calculating the area under the curve using the amplitude and standard deviation ( $A, \sigma$ ) from the fit. For lines with no discernible signal this usually results in a very large value of  $\sigma$ , and since the area

**Table 7.11**  
Raw electron number density ( $\times 10^{18} \text{ m}^{-3}$ ) as determined by the  
thresholding method.

Mass Flow (SCCM)	Discharge Voltage (V)				
–	250	300	350	400	450
40	–	4.09	2.67	4.01	–
50	–	3.20	2.30	6.57	–
60	28,700,000	130,000	2.42	4.50	2,800,000,000
70	–	–	2.62	–	–
80	–	–	6.81	–	–

under a Gaussian curve is given by:

$$Area = A\sqrt{2\pi\sigma^2} \quad (7.1)$$

large values of  $\sigma$  cause an overestimation of the area under the curve fit to the scattered spectrum. Since the area is directly proportional the free electron density (which is equal to the plasma density for the quasi-neutral plasma in the plume), this causes an overestimate of the plasma density. The corrected electron density after removal of low-signal lines can be seen in Table 7.12.

After removing low-signal lines the values for plasma density take on more reasonable values. Plasma density determined by the thresholding method ranges from approximately  $1.5 \times 10^{18} \text{ m}^{-3}$  to  $6.5 \times 10^{18} \text{ m}^{-3}$ . There appears to be no correlation between mass flow rate and plasma density, a feature also seen in the probe measurements. Bad estimates of density and bad estimates of temperature went hand in hand since the density and temperature are both calculated from the value of  $\sigma$  for the fit, and the same operating conditions that have

**Table 7.12**

Corrected electron number density ( $\times 10^{18} \text{ m}^{-3}$ ) as determined by the thresholding method. The number of lines that were removed (if any) are in parentheses.

Mass Flow (SCCM)	Discharge Voltage (V)				
–	250	300	350	400	450
40	–	4.09	2.75 (1)	3.87 (1)	–
50	–	3.20	2.30	4.14 (1)	–
60	1.57 (3)	3.92 (3)	2.06 (1)	4.50	2.77 (4)
70	–	–	2.62	–	–
80	–	–	6.42 (1)	–	–

suspect estimates of temperature also have suspect estimates of plasma density.

### 7.4.3 MLE Results

The raw plasma density as determined by the maximum likelihood estimation method for each operating condition can be seen in Table 7.13. A few of the raw temperature values determined by the MLE method exhibit the same problem as the raw values determined by thresholding, with low-signal lines making the density estimates nonsensical. The corrected plasma density measurements can be seen in Table 7.14.

Corrected plasma density as determined by the MLE method ranges from approximately  $2 \times 10^{17} \text{ m}^{-3}$  to  $7 \times 10^{17} \text{ m}^{-3}$ . There does not appear to be any strong correlation between plasma density and mass flow rate or discharge voltage. The range of plasma density estimates are less than both the probe and thresholding methods, and many of the values are close to the expected plasma density of approximately  $3 \times 10^{17} \text{ m}^{-3}$ .

**Table 7.13**  
Raw electron number density ( $\times 10^{17} \text{ m}^{-3}$ ) as determined by the MLE method.

Mass Flow (SCCM)		Discharge Voltage (V)				
–	250	300	350	400	450	
40	–	6.96	3.91	4.46	–	
50	–	5.55	5.77	3.48	–	
60	3.24	1,700,000	18,900	4.77	56,100	
70	–	–	152	–	–	
80	–	–	6.22	–	–	

**Table 7.14**  
Corrected electron number density ( $\times 10^{17} \text{ m}^{-3}$ ) as determined by the MLE method. The number of lines that were removed (if any) are in parentheses.

Mass Flow (SCCM)		Discharge Voltage (V)				
–	250	300	350	400	450	
40	–	6.96	3.56 (1)	4.11 (1)	–	
50	–	5.67 (1)	6.18 (1)	3.43 (1)	–	
60	3.23	3.63 (2)	3.76 (2)	4.77	3.83 (2)	
70	–	–	2.35 (2)	–	–	
80	–	–	6.21 (1)	–	–	

#### 7.4.4 Comparison of Density Measurements

Unlike the temperature measurements, the plasma density measurements all have a similar character. For all three techniques there is very little variation in the density and no clear trends with respect to discharge voltage and mass flow rate. In general the thresholding method density estimates are higher than both the probe and MLE methods, and the probe values are higher than the MLE values.

A comparison of the plasma density versus mass flow rate at a fixed discharge voltage

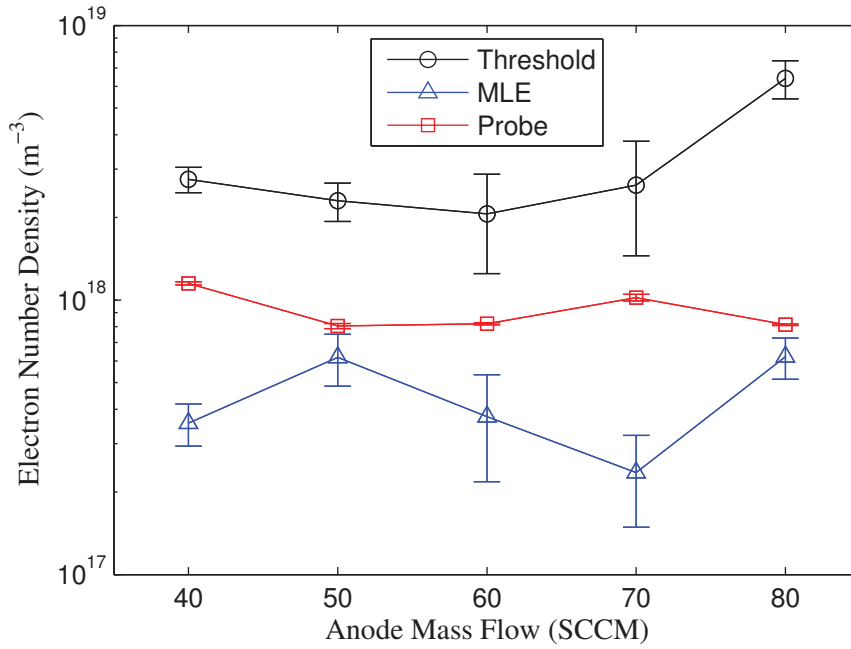


**Figure 7.7:** Comparison of plasma number density measurements vs. mass flow rate at a fixed discharge voltage of 350 V.

of 350 V can be seen in Figure 7.7. The densities determined by the thresholding method are consistently higher than the other two methods. The thresholding method also deviates significantly from the probe and MLE methods at the 350 V 80 SCCM operating condition. Using the plasma density determined by the probe as the reference value the thresholding method estimates are at least twice as high for all 350 V operating conditions. The MLE method produces density estimates that are less than the probe measurements by 25 - 80 percent.

A comparison of the plasma density versus discharge voltage for a fixed mass flow rate of 60 SCCM can be seen in Figure 7.8. All three methods have a similar trend as a function of discharge voltage, and are very flat. The thresholding method estimates are

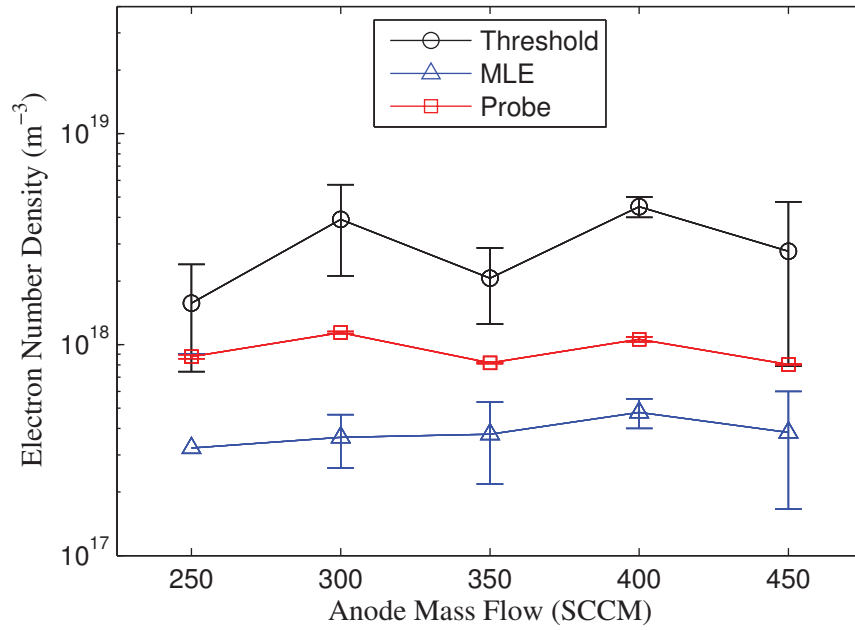


**Figure 7.8:** Comparison of plasma number density measurements vs. discharge voltage at a fixed mass flow rate of 60 SCCM.

approximately two to three times higher than the probe measurements. Estimates produced using the MLE method are consistently lower than the probe values by 50 - 70 percent.

Across all operating conditions the electron temperatures determined by the two laser methods were fairly similar, but the density estimates were remarkably different in magnitude. The reason for this was alluded to in section 6.5.3 and will now be fully explained. During laser measurements there are very few photon arrivals at a single super-pixel in the detector, and when arrivals do occur it is most often a single photon that arrives. During Rayleigh calibration there are multiple photons arriving at many super-pixels in the detector during every laser pulse. When applying the thresholding processing algorithm to the Rayleigh calibration data any instance of multiple photons



arriving at a super-pixel are regarded as a single arrival. Because of this, calculated photon arrival rate is grossly underestimated for a given calibration gas density provided the density is high enough that multiple photon arrivals are occurring regularly. This means that when the Thomson spectrum is compared to the Rayleigh spectrum it appears that the difference in photon arrival rate between the two spectra are much smaller than they really are. The MLE method produces much more reasonable electron density estimates since it accurately accounts for multiple photon arrivals in the calibration data.

## **7.5 Uncertainty, Accuracy, and Signal to Noise Ratio**

So far the results of both the laser and probe measurements have been presented without comment on the accuracy of the electron temperature and density values. The pressing question remains: which measurement method produces the most accurate values? In order to answer this question one must consider in more depth the uncertainty inherent to each of the methods. Since the thresholding method has obvious shortcomings when determining the plasma density only the maximum likelihood estimation method and probe method will be addressed.

### **7.5.1 Laser Measurements**

In theory, Thomson scattering should provide the greatest accuracy for electron temperature measurements since the electron velocity distribution is being measured

directly. In practice, there are factors that limit the certainty that can be placed on the laser measurements. The main difficulty encountered when performing Thomson scattering measurements on a Hall thruster plasma is the small scattered signal produced by the low plasma density. Equation 6.1 shows that the number of photons that are scattered by the plasma is directly proportional to the plasma density. Calculation of the estimated number of photons collected by the detection system for the experimental conditions in this work indicates that the plasma density is barely sufficient to detect any photons at all, and use of MLE data processing was required to determine the electron temperature and density from the Thomson spectrum and Rayleigh calibration data. When using pulse accumulation methods and photon counting methods with PMTs the process of defining a signal to noise ratio is well defined, but after transforming the data using the MLE processing method an SNR is difficult to define.

The first of two key sources of uncertainty in the MLE processed laser measurements is the uncertainty in the mean photon arrival rate at a given wavelength. Uncertainty in the mean photon arrival rate at a super-pixel arises due to the noise present in the detected number of counts and the rounding that occurs during MLE processing. The two specific occurrences that contribute to this uncertainty are counting of a noise-generated event as a real photon arrival and attributing an event generated by a real photon arrival to the wrong number of photons (for example, interpreting a two-photon arrival event as a single photon). In the first situation the probability of counting a noise value as a real photon event is quite small. A histogram of the noise measured at a single super-pixel with

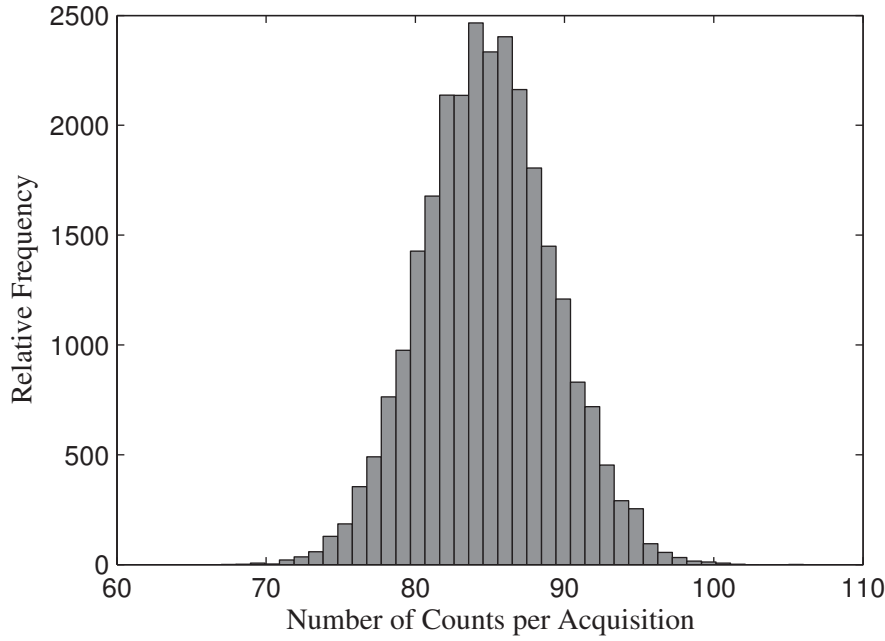


**Figure 7.9:** Histogram of the number of counts detected at a super-pixel with the spectrograph entrance slit closed over 27,000 acquisitions with an exposure time of 20 ns. These counts are purely due to noise and possess a mean of 85 counts and a standard deviation of 4.5 counts.

the spectrograph closed can be seen in Figure 7.9. Since the standard deviation of the noise (approximately 4.5 counts) is small compared to the camera gain (approximately 38 counts/photon), on average only one noise-generated event will have a count level high enough to be incorrectly attributed to an actual photon arrival during a 27,000 shot sequence. For the spectrum shown in Figure 6.18 this corresponds to less than 10 percent of the mean photon arrival rate at the  $\Delta\lambda_{1/e}$  half-width, and will be even less for the larger mean arrival rates closer to the laser wavelength. In general for the spectra determined from the data in this work the uncertainty in mean arrival rate is approximately 10 – 15 percent at the  $\Delta\lambda_{1/e}$  half-width.

The second source of uncertainty in the mean arrival rate is the miscounting of real photon arrivals. The count levels that are generated by real photon arrivals contain shot noise on the signal itself as well as noise due to the amplification process. The shot noise for an iCCD is given by [81]:

$$\sigma_{shot} = G \times F \times \sqrt{\eta \phi_p \tau} \quad (7.2)$$

where  $G$  is the camera gain,  $F$  is the noise factor (due to the gain process),  $\eta$  is the quantum efficiency,  $\phi_p$  is the photon flux in photons per second per super-pixel, and  $\tau$  is the acquisition time. Converting from photons to counts and substituting the camera noise factor of 1.6 yields:

$$\sigma_{shot} = 1.6 \cdot \sqrt{Counts}. \quad (7.3)$$

Since the noise level is a function of the count level, the count level influences the chances of a miscount occurring. The shot noise and detector noise are uncorrelated and add in quadrature, such that:

$$\sigma_{total} = \sqrt{\sigma_{shot}^2 + \sigma_{detector}^2} \quad (7.4)$$

Using 38 as the mean count level for single photon arrivals the rate at which a single photon arrival will be counted as a 0 or 2 is approximately 8 percent. For two-photon arrivals using 76 as the mean count value yields a miscount rate of approximately 20 percent. The miscount rate continues to increase for higher count values, but the signal to noise ratio actually increases since the error from counting a single photon as zero or two photons is

much greater than the error from counting three photons as two or four photons. Since most of the arrivals are single photon events with only a few multi-photon events the uncertainty in the mean arrival rate determined from these calculations can be estimated at approximately 10 - 15 percent.

The second key source of uncertainty in the MLE processed laser measurements is the uncertainty in the fit of the scattered spectrum. The first and most obvious contribution is the assumption that the plasma is both isotropic and Maxwellian. The scattered spectra are well fit by a Gaussian curve and the probe data reduction technique also makes this assumption, so it is of secondary concern. A more important factor is the certainty that can be placed on the determination of the fit parameters of the scattered spectrum, which is related to the uncertainty in the mean photon arrival rate at each wavelength that was just discussed. Using the residuals calculated from the non-linear least-squares fit it is possible to compute 95 percent confidence intervals for the fit parameters. The 95 percent confidence intervals give a range within which one can say the true values of the parameters lie, with 95 percent confidence. If repeated measurements were made at this same condition one would expect that 95 percent of these measurements would produce fit parameters within these bounds. While these confidence intervals are not predictive, reasonable bounds can be put on the estimates of electron temperature and density calculated from the scattered spectra. An example of these bounds for a good spectrum can be seen in Figure 7.10. The calculated values of temperature and density at this operating condition for the best fit (averaged over 0.5 mm along the beam) are 5.93 eV and  $6.96 \times 10^{17} \text{ m}^{-3}$ ,

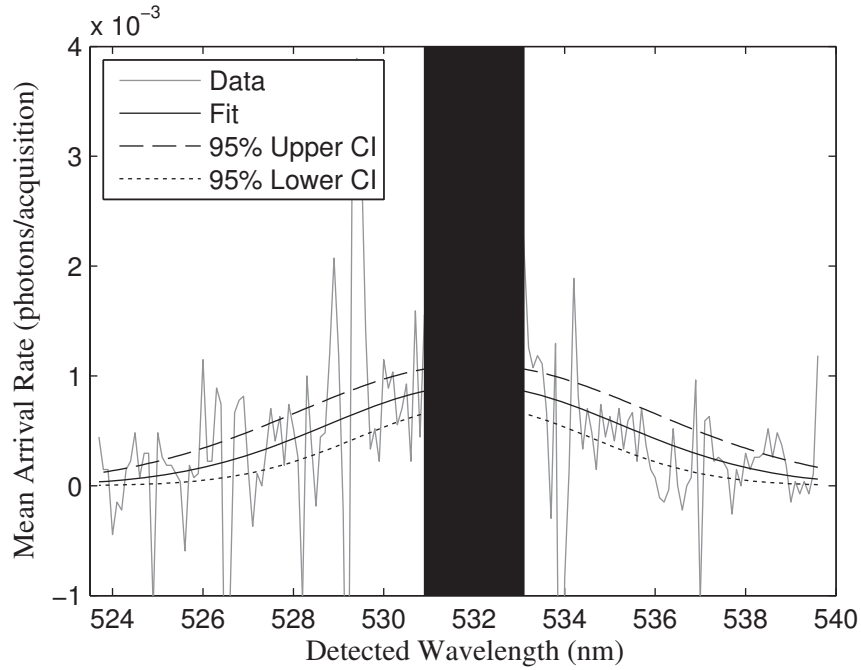


**Figure 7.10:** Plot of the curve fit to a Thomson spectrum, including 95 percent confidence intervals. Thruster operating at 300 V discharge and 40 SCCM mass flow rate.

respectively. If the parameter estimates corresponding to the confidence interval bounds are used to calculate the electron temperature and density the upper values provide a temperature of 8.98 eV and a density of  $1.09 \times 10^{18} \text{ m}^{-3}$ , which are approximately 50 percent higher than the values given by the best fit to the data. The lower values yield a temperature of 3.52 eV and a density of  $3.91 \times 10^{17} \text{ m}^{-3}$ , which are approximately 40 percent lower than the values calculated from the best fit.

The effect of the curve fit to the spectrum is more pronounced when the Thomson signal is weaker. There are multiple reasons for a weaker signal, including a coating on the collection lens, lower electron density, and misalignment of the laser and collection

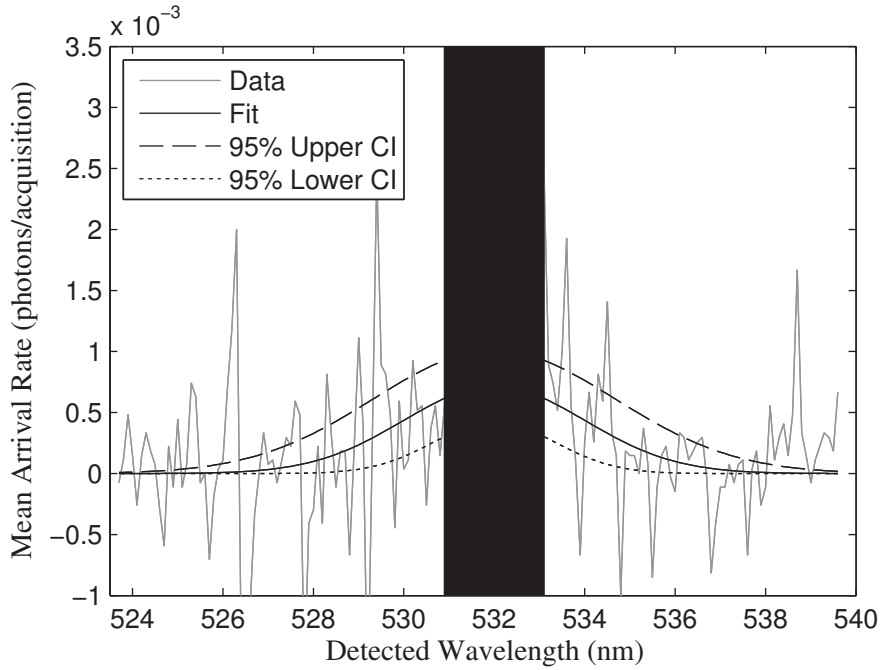


**Figure 7.11:** Plot of the curve fit to a Thomson spectrum, including 95 percent confidence intervals. Thruster operating at 350 V discharge and 40 SCCM mass flow rate.

volume. Alignment of the probing laser and the collection lens axis has a strong effect on the signal in scattering measurements. The Thomson signal is produced by the laser beam, and if the optics are not capturing the scattered photons no signal is measured at the detector. On the other hand, xenon emission is present nearly everywhere in the plasma, and even if the collection optics are not targeted near the laser beam a strong emission signal will be detected. The mean value of the emission signal can be subtracted but the noise on this signal cannot, making the fit less certain. An example of the fit to a line with less detected Thomson signal can be seen in Figure 7.11. The calculated values of temperature and density at this operating condition for the best fit are 9.48 eV and  $3.56 \times 10^{17} \text{ m}^{-3}$ , respectively. The upper confidence interval values provide a temperature of 20.7

eV and a density of  $6.80 \times 10^{17} \text{ m}^{-3}$ , which are approximately 120 percent and 90 percent higher (respectively) than the values given by the best fit to the data. The lower values yield a temperature of 2.82 eV and a density of  $1.39 \times 10^{17} \text{ m}^{-3}$ , which are approximately 70 percent and 60 percent lower (respectively) than the values calculated from the best fit. This high degree of uncertainty is reflected in the large error bars at this operating condition seen in Figure 7.5.

Given the sources of uncertainty just discussed and the error bars calculated from the fits to the data, the uncertainty of the MLE processed laser measurements presented in this work is estimated at 30 to 100 percent depending on the scattered signal strength. The uncertainty in the fit parameters is a more dominant factor than the uncertainty in the mean arrival rate at a given wavelength, and decreases with increased Thomson signal. This figure also includes the fact that for most operating conditions at least one low-signal line was removed during processing. Methods of increasing the Thomson signal will be discussed in detail in the next chapter. In addition to the uncertainty in the fit of the Thomson spectrum, determination of the Rayleigh scattering spectrum that is used to calibrate the density measurements can affect the density estimates. Although the same camera and spectrograph settings are used during measurement of the Rayleigh signal as for the scattered signal, the Rayleigh signal is in a different photon flux regime than the Thomson signal. The MLE method accounts for this difference, but there is clearly greater certainty in the estimation of the Rayleigh scattering spectrum than the Thomson spectrum, and difference in relative uncertainty limits the overall confidence in the density



estimates provided by the MLE method. Since the Rayleigh measurements are not used to calculate the electron temperature, the temperature values have less uncertainty than the density values.

### **7.5.2 Probe Measurements**

The estimated accuracy of Langmuir probe measurements varies greatly depending on the type of probe, the plasma conditions, the equipment used to perform the measurement, and the analysis method applied to the data [82]. Langmuir probes have been used extensively since the late 1920's but the accuracy of probe measurements with respect to the actual plasma properties is not well addressed. There are a few papers in the literature that compare different probe types and data analysis methods to one another [82–85], but in most work performed with probes the issue of probe accuracy is simply ignored. Sudit and Woods [82] compared plasma densities determined by applying various data reduction methods to Langmuir probe measurements and found that the difference in plasma density varied by as much as a factor of 10 depending on which analysis method was used. They also compared the probe measurements to electron density measurements made using microwave interferometry techniques and reported uncertainties in the range of 30 to 50 percent, but added the caveat that better local measurements were required to truly know the relative accuracy since microwave interferometry is a line-integrated measurement. Meulenbroeks et al. [86] compared four different methods of measuring the electron temperature and density in low temperature plasmas and stated an accuracy of

approximately 25 percent for double Langmuir probes without direct justification. They also reported that while the statistical errors involved in probe measurements are often low, the values provided can deviate significantly from other measurement methods such as Thomson scattering. The reason given to explain this discrepancy was that the presence of the probe disturbed the plasma, especially in regions with large gradients in the plasma properties [86].

It is the author's experience that in the space propulsion diagnostics field it is generally accepted that probes have an accuracy of 15 to 50 percent depending on the plasma conditions and reduction technique. Most researchers never address this issue since no references in the literature are readily available and each plasma/probe/analysis combination will suffer from unique uncertainties and shortcomings. In general the author considers this a reasonable range for typical probe measurements, and given the location of the probe and possible influence on the plasma discharge during measurement the accuracy is in the upper end of this range for the probe measurements performed in this work. While the discharge current disruption was small, this does not mean that discharge oscillations were not increased. It is also possible that the probe was intercepting Hall current in the near-field plume of the thruster, thus altering the measured electron temperature and density [4]. Since probe measurements are invasive, the effect of the presence of the probe cannot be de-coupled from the measurement. Even though the uncertainty in the curve fits to the probe traces are very small, this does not mean that the measurements accurately reflect the plasma conditions when the probe is not present.

## 7.6 LTS versus Double Probes

Now that the measurement accuracy and uncertainty have been addressed it is possible to compare and contrast laser and probe measurements. In general the probe traces conform very well to the expected hyperbolic tangent shape, with the only exception being the two traces taken at the first operating condition (300 V and 40 SCCM). A plot of the first trace taken at this condition can be seen in Figure 7.12. In this trace it appears that the plasma is actually jumping between two distinct plasma conditions when the probe-to-probe voltage is above approximately 5 volts. The cause of this unusual trace is unknown, but the two traces taken at this operating condition were the only traces that exhibited this strange behavior (plots of all probe traces can be found in Appendix A). It is obvious that the uncertainty in the electron temperature and density determined from such an unusual trace is quite high, especially for the density.

In contrast, the LTS spectra measured at the 300 V 40 SCCM operating condition are quite good. A sample Thomson spectrum can be seen in Figure 7.13. The signal contains significant noise, but the Gaussian shape of the spectrum is clearly visible. In spite of the poor probe traces the probe and LTS measurements at this operating condition agree remarkable well, with the probe indicating a temperature of 8.08 eV and density of  $6.69 \times 10^{17} \text{ m}^{-3}$ , and the LTS data indicating a temperature of 5.93 eV and  $6.96 \times 10^{17} \text{ m}^{-3}$ . This was the first operating condition and some of the best Thomson spectra were measured at

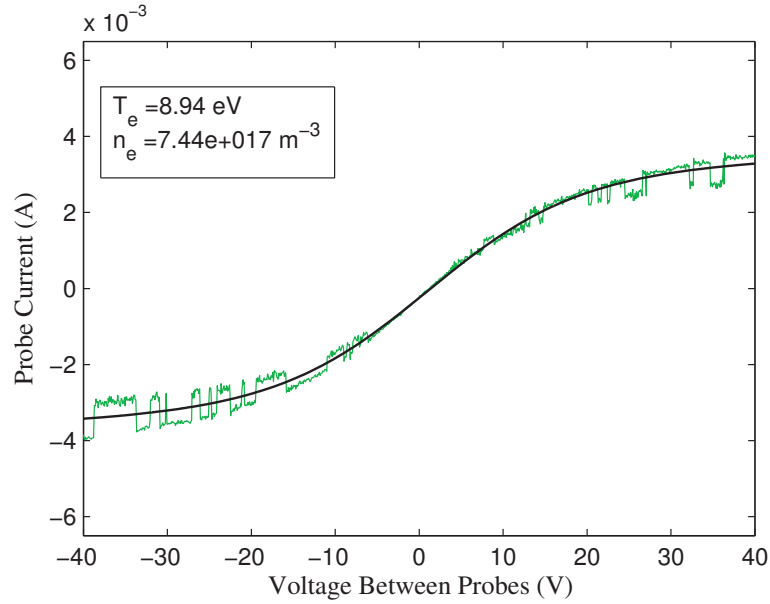


**Figure 7.12:** First Langmuir probe trace taken at 300 V discharge and 40 SCCM mass flow rate. The plasma seems to be jumping between two distinct operational states.

this condition.

Given the uncertainty in the two measurement techniques the electron temperatures and densities produced by both the double probe and the LTS measurements agree fairly well at lower discharge voltages, but deviate significantly at the 350 V 80 SCCM, 400 V 50 SCCM, 400 V 60 SCCM, and 450 V 60 SCCM operating conditions. Which measurement technique gives the correct values? To answer that we must again turn to inspection of the probe traces and Thomson spectra. A sample Thomson spectrum from the 400 V 60 SCCM operating condition can be seen in Figure 7.14. Although a Gaussian curve fit can be applied to the spectrum, the fit is not very good. This is especially true for wavelengths between 526 and 529 nm where the fit line is almost always above the data. Such poor

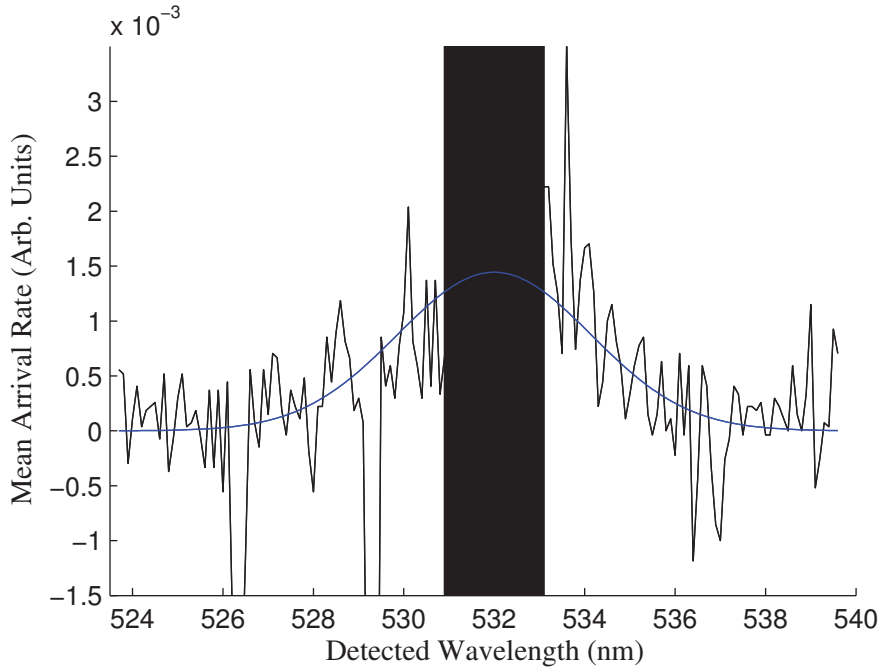


**Figure 7.13:** Sample Thomson spectrum measured at 300 V discharge and 40 SCCM mass flow rate. The Gaussian shape of the trace is clearly visible.

fits can skew the calculated electron temperature and density significantly. For all of the measurement conditions just mentioned the one-sigma error bars range from 30 percent of the stated value all the way up to more than twice the stated value.

In addition to poor curve fits skewing the temperature and density estimates, high electron temperatures can effectively reduce the signal level. A second trace from the 400 V 60 SCCM operating condition can be seen in Figure 7.15. This spectrum is fit reasonably well by a Gaussian curve, but the amplitude is very low and the signal is very noisy. For a fixed plasma density the number of electrons that scatter photons into the collection solid angle is constant, and as the temperature is increased more photons will be scattered off of faster electrons. This flattens the scattered spectrum and increases the calculated

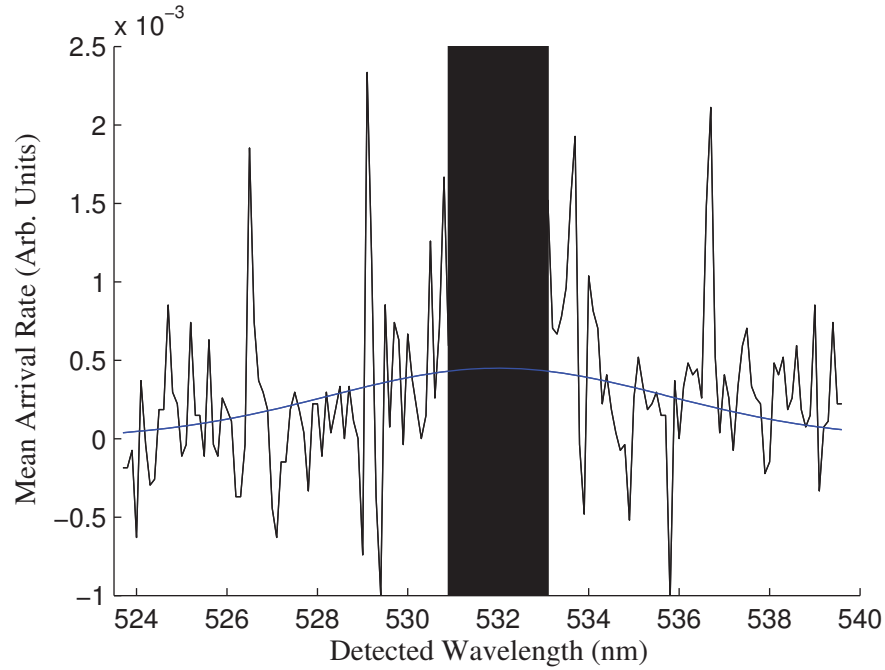


**Figure 7.14:** Sample Thomson spectrum measured at 400 V discharge and 60 SCCM mass flow rate. This trace is not fit well by a Gaussian curve.

temperature (as expected). Unfortunately, this flattening causes two negative effects. The first effect reduces the signal level in the high SNR regions near the laser wavelength, which makes high-confidence fits to the spectrum difficult. The second negative effect is that for high enough electron temperatures signal photons will be shifted to wavelengths further from the laser line than the system can detect. For the spectrum shown in [Figure 7.15](#) the electron temperature determined from the fit is 27.5 eV. For this temperature the 1/e half-width is approximately 7.7 nm, which means that a significant fraction of the spectrum is not detected by the iCCD. A practical upper limit for electron temperatures measurable with the current experimental apparatus is approximately 30 eV, which places the 1/e half-width at the edge of the detector. Measurements of higher electron temperatures

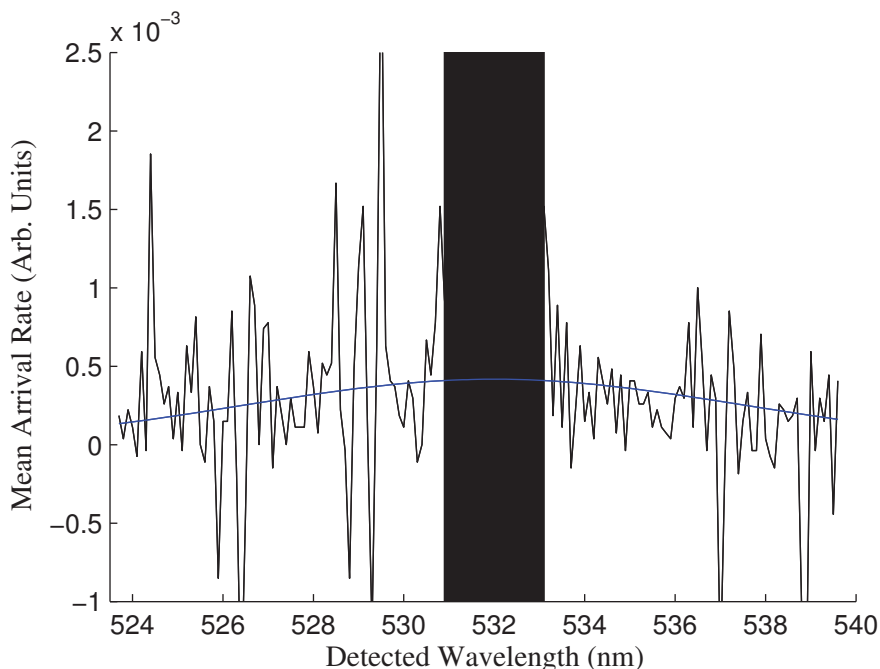


**Figure 7.15:** Second sample Thomson spectrum measured at 400 V discharge and 60 SCCM mass flow rate. This trace is fit reasonably well by a Gaussian curve, but has very low amplitude.

are possible if only one side of the spectrum is recorded, provided the electron density is high enough.

The next step is to inspect the probe traces taken at the 400 V 60 SCCM operating condition and see if there are any significant deviations in the I-V curves. The double probe traces performed at this condition can be seen in Figures 7.16 and 7.17. Inspection of both traces shows very good fit at low probe-to-probe voltages and the temperature measurements from the two traces are similar. It is interesting that 2 measurements taken approximately 30 seconds apart differ by approximately 16 percent, which is in line with the expected uncertainty discussed previously. The probe fit to the first trace (7.16) is

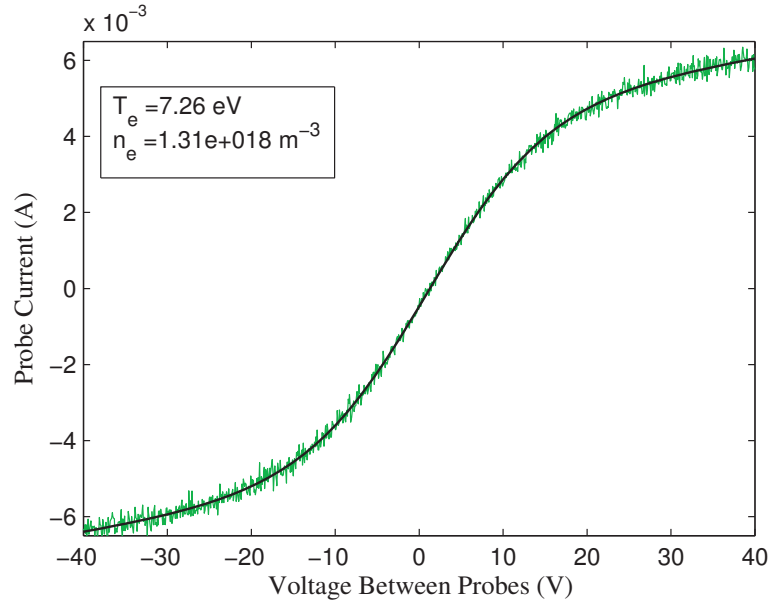


**Figure 7.16:** First Langmuir probe trace taken at 400 V discharge and 60 SCCM mass flow rate.

quite good in the ion saturation regions, and the uncertainty in the fit parameters from this trace are small. The second trace fit (7.17) is not nearly as good in the ion saturation regions, and there is significantly more noise in the measurement. The probe measurements are consistent, but even if the probe is disrupting the discharge it should do so in a consistent manner. As such, the probe measurements actually reflect a measurement of the probe-plasma system.

One of the key differences between probe and laser measurements is the source of measurement uncertainty. While the probe traces were fit reasonably well by the hyperbolic tangent data analysis, there is no way of knowing exactly how the probe disrupts the plasma it is measuring and how the disruption modifies the temperature and density values produced from analysis of the data. Probe measurements may be consistent from



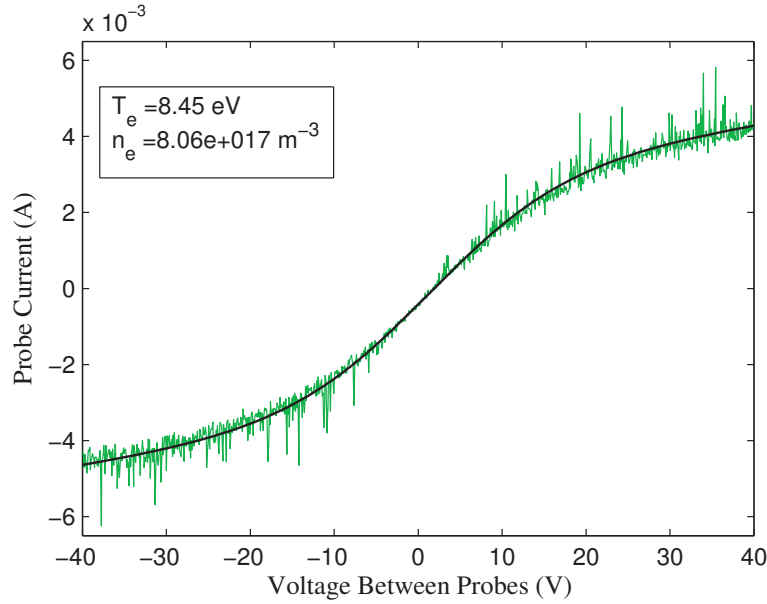


**Figure 7.17:** Second Langmuir probe trace taken at 400 V discharge and 60 SCCM mass flow rate.

measurement to measurement, but this does not mean that the measured plasma properties accurately reflect the state of the plasma.

The source of uncertainty in the laser measurements is quite different, and primarily comes from low signal to noise ratio. Thomson scattering is both non-invasive and direct, so measurement uncertainty and accuracy are closely linked. Some of the lines contained so little signal that they were removed from the data analysis entirely. At lower discharge voltages there is reasonable agreement between the double probes and the laser measurements, and although the error bars are somewhat large, one can be confident that the LTS measurement is not disrupting the plasma. At higher discharge voltages the Thomson spectra indicated temperatures much higher than the probes, but the accuracy of the LTS measurements at these higher temperatures is suspect primarily due to low SNR from a

significant fraction of the scattered photons not being detected. –

At lower voltages agreement between the probe temperature values and the MLE values was often strong, with the error bars overlapping at the 300 V 60 SCCM, 350 V 40 SCCM, and 350 V 50 SCCM operating conditions. The density values determined by the MLE method were consistently lower than the probe values, but it is likely that the coating on the collection lens caused the reduced density estimates. Based on the MLE measurements it appears that at these conditions the probe is not disrupting the probe enough to cause disagreement with the LTS measurements. At higher discharge voltages there is strong disagreement between the LTS and probe measurements. This could be caused by increased probe disruption or it could be an artifact of the low signal to noise ratio at these conditions. Although Thomson scattering has the ability to accurately determine the electron temperature and density in a plasma without perturbation, for the work reported the SNR was not sufficiently high to conclusively say that the double probe measurements were inaccurate due to the disruptive presence of the probe. This is especially true at the higher discharge voltage conditions where the uncertainty in the LTS measurements were very large. In order to determine the extent of the disruption caused by the probe (if any) more accurate LTS measurements are required. Improvements to the LTS diagnostic developed for this work will make highly accurate measurements possible, and discussion of these improvements can be found in Chapter 8.



# **Chapter 8**

## **Conclusion and Future Work**

### **8.1 Introduction**

The main goal of this work was to perform both electrostatic probe and laser Thomson scattering measurements in the near-field plume of a Hall thruster in order to determine the feasibility of laser Thomson scattering as a diagnostic for space propulsion devices. This chapter will discuss the key results of this study and provide an assessment of the use of Thomson scattering as a diagnostic for space propulsion plasmas. Suggestions for improvement of the current experimental apparatus will also be discussed.

## 8.2 Summary of Experimental Results

This study has demonstrated that it is possible to perform laser Thomson scattering measurements in the plume of a Hall thruster. Doing so required overcoming significant experimental challenges along with development of a new method of processing the scattered signal. It was discovered through progressive development of the measurement apparatus that the plasma conditions and measurement geometry combined to produce a scattered signal that was barely detectable by the equipment available for this project. Early work required a modest detection limit of approximately  $10^{18} \text{ m}^{-3}$  for plasma temperatures on the order of a few electron volts [87]. As LTS was applied to more plasmas the detection limit was decreased to approximately  $10^{17} \text{ m}^{-3}$  for plasmas with temperatures of around 1 eV [35]. More complicated implementations using Rayleigh blocks, atomic notch filters, and multi-pass cells have pushed the detection limit to approximately  $5 \times 10^{16} \text{ m}^{-3}$  [43], and for some systems a theoretical detection limit as low as  $2 \times 10^{15} \text{ m}^{-3}$  has been suggested [15]. While the detection limit of approximately  $10^{17} \text{ m}^{-3}$  for the LTS diagnostic at MTU is not exceptional in this regard, difficult optical access problems were overcome and Thomson scattering spectra were obtained that produced values of electron temperature and plasma density that exhibited reasonable agreement with electrostatic probe techniques over a wide range of operating conditions.

Two methods of processing the laser measurements were compared to double probe

measurements, and the values produced by each method had distinct characteristics. The new maximum likelihood estimation method of data processing produced estimates of electron temperature and density that reproduced some of the general trends seen in the electrostatic probe data, and also exhibited trends that were expected but not seen in the probe measurements. The thresholding method produced electron temperature estimates that were often similar to the MLE values, but plasma density estimates were higher by nearly an order of magnitude. For both the thresholding and MLE methods a significant number of low-signal lines had to be removed from the processed data, which increased the uncertainty in the measured values.

Although there was considerable uncertainty in the laser measurements, they are inherently non-disruptive. The uncertainty is therefore closely related to the accuracy, unlike the probe measurements where the effect of the probe on the measured plasma properties is unknown. Agreement between the laser and probe measurements at lower discharge voltages is encouraging, but at higher discharge voltages the two methods deviate. If increasing the discharge voltage moved the acceleration zone downstream from the anode it is possible that the laser measurements detected the increase in temperature while the probe cooled the plasma locally by its presence. The signal to noise ratio was low for the higher discharge voltage conditions, and although higher SNR measurements are required in order to definitively say that the probe was causing local cooling of the plasma, it appears that this was the case for the measurements performed in this work. Improvements to the laser measurement system will enable high SNR measurements and

allow the extent of probe disruption to be quantified.

## **8.3 Improvements and Future Work**

### **8.3.1 External Measurements**

Having discussed the results and some key limitations on the application of LTS to Hall thrusters (see section 7.6), specific areas of improvement for the MTU LTS diagnostic will be discussed. One of the most important improvements that can be made is obtaining an iCCD with much higher quantum efficiency. Multi-channel plates (MCPs) with GaAsP photocathodes have quantum efficiencies of nearly 50 percent near 532 nm, and iCCDs that use these types of MCPs are readily available. While these cameras are rather expensive, this simple upgrade would increase the number of detected photons by a factor of five. A related improvement is to change the spectrograph from a triple monochromator to a double monochromator. The increase in throughput from using a double monochromator would result in as many as two times the photons arriving at the detector. Ultimate resolution may have to be sacrificed for greater throughput but since the electron temperature is relatively large this should not greatly affect the detected spectrum.

Minimizing stray light is always a concern in Thomson scattering measurements, and reducing stray light can extend the detection limit to lower electron densities. Stray light sets the limit of how close to the discharge channel exit plane the measurement position

could be located for this work, and was determined mainly by scatter produced by poorly focused light scattering from the thruster itself. The number of poorly focused photons seems negligible when compared to the number of photons at the focus, but is significant when compared to the number of Thomson scattered photons that enter the detection solid angle. Beam quality can be improved significantly by using a focal-plane stop described by Evans and Katzenstein [27], but implementing such a system would be very difficult given the current position of the laser due to space limitations. It would be possible to fold the beam using mirrors and make an extended beam enclosure to implement this change, but this may not be a feasible upgrade for the MTU LTS diagnostic.

Regardless of whether or not it is possible to produce a cleaner and better-focused beam, measurements closer to the thruster would be possible if the focusing lens and beam dump were modified. Due to space limitations the beam is focused from full to minimum diameter in 0.5 meters. This is necessary so that after passing through the plasma the beam increases in diameter enough to allow the beam dump to handle the power density without being destroyed. If the beam was focused more slowly the beam envelope would be more narrow near the thruster face, allowing the focal point to be closer the thruster. This would require adding a port to the bottom of the vacuum chamber in order to move the beam dump further away from the focus, allowing time for the power density to decrease to manageable levels.

A different approach is to worry less about the stray light level and instead implement



a Rayleigh block inside of the spectrograph. A Rayleigh block is usually just a thin strip of material placed in the light path after a diffraction grating, positioned such that it blocks a narrow wavelength band centered at the laser line. This has the advantage of reducing the stray light level by several orders of magnitude, allowing closer measurements with higher stray light without making difficult changes to the beam delivery and disposal components. A drawback to this approach is that calibration for density measurements can no longer be performed using Rayleigh scattering measurements and more complicated methods of calibration (for example, using ro-vibrational Raman scattering [15]) must be implemented.

Beam alignment could be greatly improved by the addition of a 6-axis motorized mount for the laser turning mirror. The collection lens and spectrograph are fixed with respect to the vacuum chamber and the only method of aligning the detection system is by adjusting the turning mirror. Currently the turning mirror is on a 3-axis kinematic mount with manual adjustments. At 100 threads per inch the adjustments are fine enough for delicate manipulation of the mirror, but even the pressure of one's hand on the mount can cause small changes in the position of the mirror. Using a motorized mount would give much finer control, and using a 6-axis mount would allow for small translational adjustments in addition to angular control of the beam. A program could also be written that automatically steers the beam around a small range and maximizes the Rayleigh scattering in order to better align the system, and could even be used at high vacuum to "hunt" for the correct beam position in the event that no Thomson signal is detected.

In addition to the use of a motorized mirror, it may be possible to actively align the laser with the scattering volume. One way that this could work would be to find a gas that fluoresces strongly when excited at 532 nm and can be added in trace quantities to the propellant gas. Ideally the gas would be excited by the laser photons at 532 nm and relax non-resonantly at a different wavelength. The signal detected from the trace gas can then be used as feedback to the mirror steering system. Implementing active alignment may require a beam splitter and a second spectrograph to detect the tracer signal since the spectrograph that is detecting the Thomson signal must have a high dispersion. Adding a beam splitter would reduce the Thomson signal but may be an acceptable loss since poor alignment can make the signal disappear altogether.

All of the changes that have been discussed thus far can be considered direct upgrades to the current diagnostic which is only capable of measurements outside the discharge channel. There are other avenues of future work requiring major changes to the current LTS diagnostic that will allow internal measurements of electron temperature and density in a Hall thruster (as well as better external measurements).

### **8.3.2 Internal Measurements**

External measurements of electron temperature and density are of value but the ultimate goal for laser Thomson scattering is to be able to perform internal measurements, especially in the acceleration zone near the end of the discharge channel. In order to perform such

measurements the scattering geometry will have to be modified significantly. One way to do this is to add a spool-piece to the end of the main vacuum chamber that is large enough to house a Hall thruster but small enough that the laser and collection optics can be located much closer to the scattering volume. Implementation of this test arrangement has several important advantages. First, optical access to the plasma will be much easier which in turn simplifies alignment significantly. Second, it will be possible to deliver the beam and collect the scattering from different angles. This allows measurement of the electron velocity distribution function along different directions in the plasma which will be important in the acceleration zone where the strong applied magnetic field may cause significant anisotropy in the electron distribution. Finally, it will be fairly simple to change the type of laser being used to interrogate the plasma. A different wavelength may be desirable to reduce plasma emission or to perform coherent Thomson scattering measurements (see [88]).

Moving the thruster to a compact spool piece allows improved measurement even if the beam delivery remains transverse to the thruster axis. A schematic showing one possible experimental configuration can be seen in Figure 8.1. If the beam is delivered external to the thruster movable collection optics allow measurements very close to the exit plane. More importantly, if the thruster body is machined such that sections of the discharge channel walls are removable internal measurements can be performed by passing the beam through the thruster itself. The scattered signal can be collected through additional openings in the thruster body. A schematic of this configuration can be seen in Figure 8.2. If the thruster is

mounted on a small motion stage spatial mapping of the electron temperature and density inside the thruster is possible.

Another major change that could be implemented is to modify the thruster to allow the laser beam to pass through it. If a hole is drilled in the back plate of the thruster and an anode is constructed with an aperture for the beam to pass through the laser can be introduced into the plasma from the back of the thruster and pass out of the channel in the same direction as the plasma beam. A schematic of this concept can be seen in Figure 8.3. If the beam was passed through the back of the thruster the existing optics could still measure at the current downstream location, and if moveable optics were introduced it would also be possible to measure electron temperature and density in portions of the exit plane of the thruster. Once again, the thruster could be mounted on a motion stage and translated such that measurements at different locations in the plume could be performed. If sections of the thruster wall can be removed it is possible to perform internal measurements in a similar manner to the transverse beam configuration. A schematic of an equipment configuration that allows internal measurement can be seen in Figure 8.4. One possible issue that would have to be overcome is that a rather large opening would be needed to accommodate the fast, large diameter lens currently required. Slots added to the thruster body may also affect the operation of the thruster significantly.

If adding slots to the thruster greatly changes the operational behavior, the throughput of the spectrograph could be increased along with the quantum efficiency of the camera.

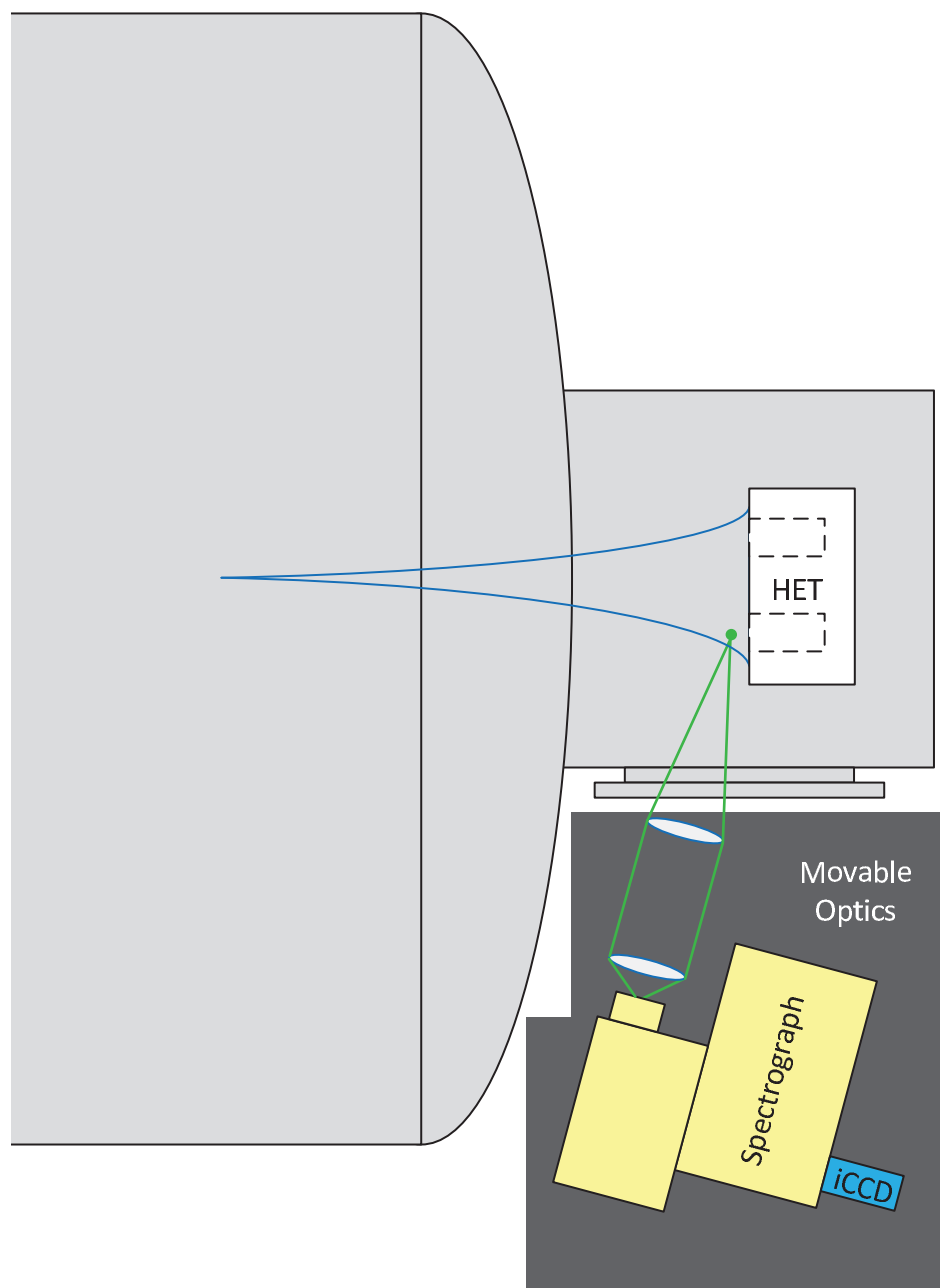


**Figure 8.1:** Sample scattering configuration with the Hall thruster in a small spool-piece. The laser beam is delivered from above (not shown).

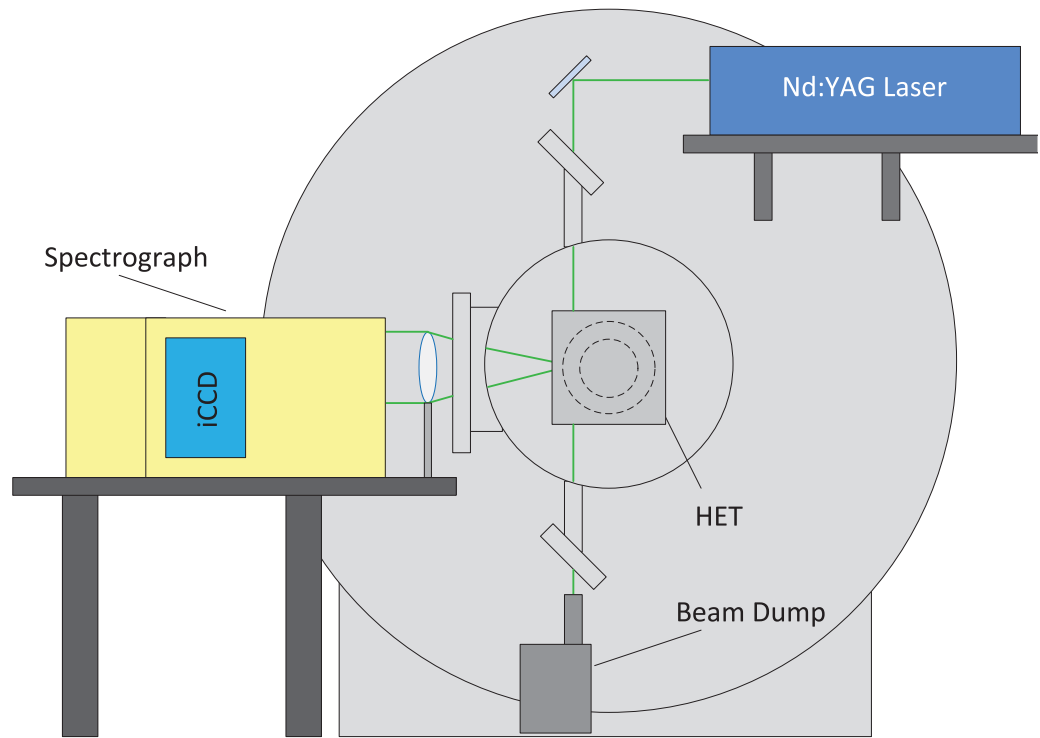


**Figure 8.2:** Sample scattering configuration with the Hall thruster in a small spool-piece. The beam can be passed through the thruster body where the wall has been removed.

This would allow the use of a smaller lens or even optical fibers that would either greatly reduce the size of the slot needed in the thruster body or completely eliminate it. A configuration that utilizes a beam passing through the thruster axially and optical fibers for signal collection can be seen in Figure 8.5. In this schematic optical fibers with integral lenses are located at fixed positions inside the wall of the thruster. An alternative to a fixed-fiber configuration would be a slot along the entire length of the discharge channel that would allow a fiber to be translated along the wall. One potentially serious drawback to this method would be the survival of the lens and fiber in the extreme plasma environment

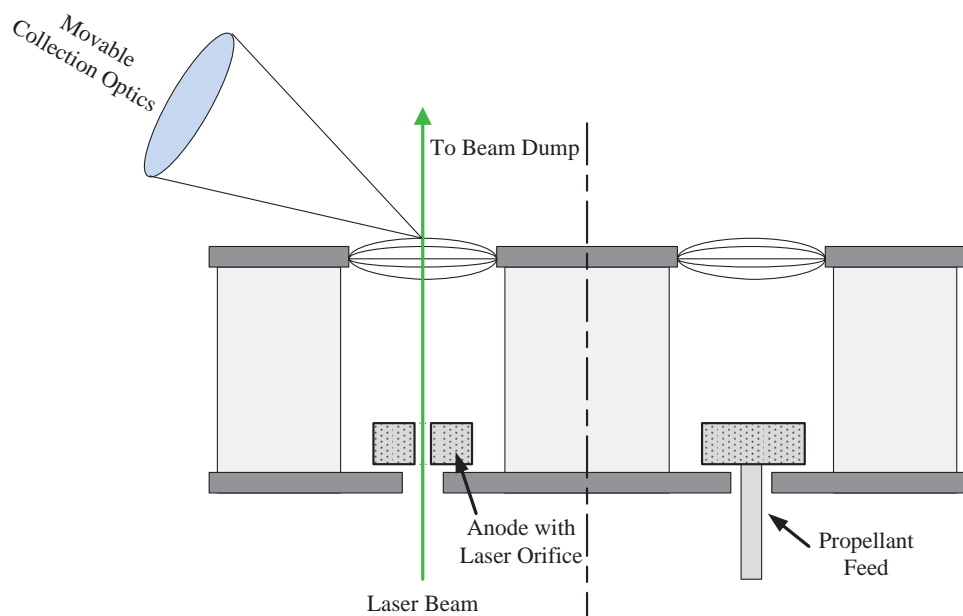


**Figure 8.3:** Schematic of measurement geometry where the laser beam passes through the thruster. Downstream optics collect the scattered photons.

of the channel.

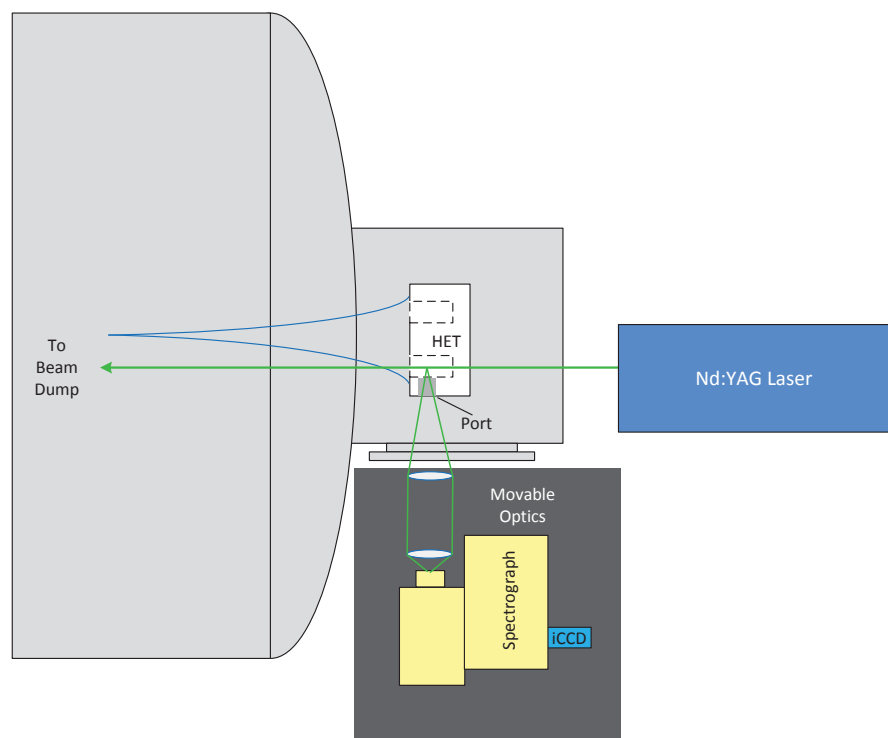


**Figure 8.4:** Schematic of measurement geometry where the laser beam passes through the thruster. Slots in the thruster body allow internal measurements of electron temperature and density.



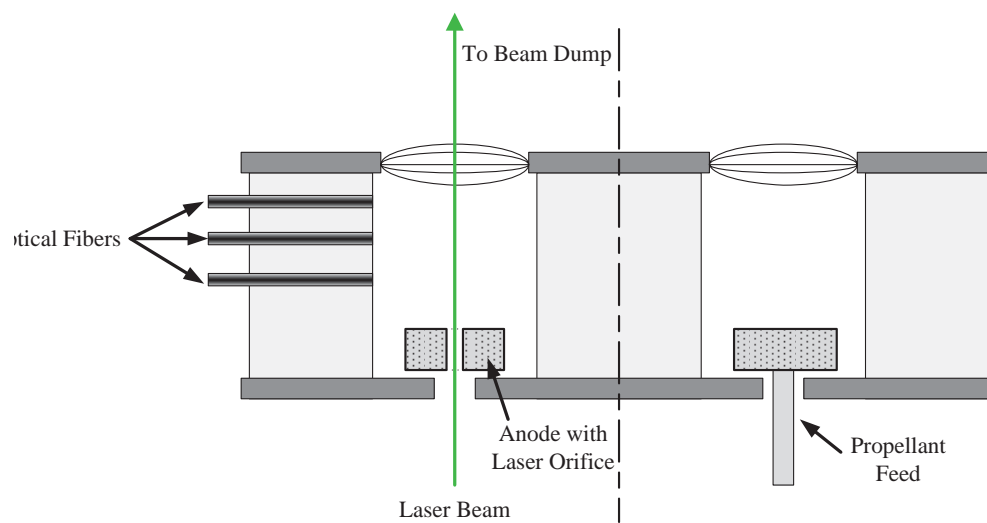


**Figure 8.5:** Schematic of measurement geometry where the laser beam passes through the thruster. Fiber optics embedded in the thruster wall can measure internal electron properties.

## 8.4 Conclusion

Hall thrusters have been developed and studied extensively over the past 60 years. Research on these devices continues, with particular emphasis on understanding the electron properties in the discharge. The vast majority of electron temperature and density studies have been performed using electrostatic probes methods. Probes are relatively simple to use but can disrupt the very plasma conditions they are trying to measure. This work has demonstrated that laser Thomson scattering can be used as a non-perturbing alternative to probe measurements and has the potential to provide accurate measurements of electron temperature and density in Hall-effect discharges (and other space propulsion devices).

Laser measurements were processed using both a thresholding method and a new maximum likelihood estimation method, and corresponding measurements were performed using traditional electrostatic double probes. Given the uncertainty in the laser and probe measurements electron temperature values were reasonably similar for the MLE and probe methods for discharge voltages of 350 Volts or less (excluding the 250 V 60 SCCM condition). At higher discharge voltages the both the thresholding values and the MLE values were significantly higher than the probe values, but the uncertainty in the laser measurements was very high at these discharge voltages (see section 7.6). Temperature values produced by the probes were insensitive to discharge voltage and mass flow rate, but

both laser methods produced temperature values that increased with increasing discharge voltage.

Agreement between the three methods was not as good for electron density measurements. All three methods possessed similar trends with respect to mass flow rate and discharge voltage, but the magnitudes of the measurements varied significantly. The thresholding method produced density values that were much higher than the MLE and probe methods at all operating conditions. In general the density values produced by the thresholding method were approximately two to three times higher than the probe values, and approximately five times higher than the MLE values. The MLE values exhibited much better agreement with the probe values, but were still approximately half of the probe values at most operating conditions.

Laser Thomson scattering is a non-invasive technique that should provide the most accurate measurements electron temperature by directly measuring the electron velocity distribution function, and as such it is tempting to conclude that the probe measurements missed a real increase in electron temperature at the measurement location at higher discharge voltages. However, the scattered spectra at these high discharge voltage operating conditions were very weak and there is a great deal of uncertainty in the temperature and density values determined from these spectra. At this time it is not possible to say that the electrostatic probe measurements performed in this work are inaccurate. Further development of the LTS diagnostic at MTU will allow higher SNR measurements which

will conclusively demonstrate how accurate electrostatic probe measurements are in the near-field plume of a Hall thruster. Several paths of improvement of the LTS diagnostic at MTU have been identified, and further development of this diagnostic tool will enable accurate external and internal measurements of electron temperature and density in Hall thrusters. Accurate measurements of electron properties in the discharge will improve understanding of the plasma conditions in the discharge and ultimately aid the development of the next generation of Hall thrusters.



# References

- [1] Gascon, N. M., Dudek, M., and Barral, S., “Wall Material Effects in Stationary Plasma Thrusters. I. Parametric Studies of an SPT-100,” *Physics of Plasmas*, Vol. 12, No. 10, 2003, pp. 4123–4136.
- [2] Fossum, E. C., *Electron Transport in  $E \times B$  Devices*, Doctoral dissertation, Michigan Technological University, 2009.
- [3] Raitses, Y., Staack, D., Keidar, M., and Fisch, N. J., “Electron-Wall Interaction in Hall Thrusters,” *Physics of Plasmas*, Vol. 12, 2005.
- [4] Haas, J., *Low-Perturbation Interrogation of the Internal and Near-Field Plasma Structure of a Hall Thruster Using a High-Speed Probe Positioning System*, Ph.D. thesis, University of Michigan, 2001.
- [5] Raitses, Y., Staack, D., Dorf, L., and Fisch, N. J., “Experimental Study of Acceleration Region in a 2 kW Hall Thruster,” *39th AIAA/ASME/SAE/ASEE Joint Propulsion Conference & Exhibit*, Huntsville, AL, 2003.

- [6] Ross, J. L., *Probe Studies of a Hall Thruster at Low Voltages*, Dissertation, Michigan Technological University, 2011.
- [7] Maiman, T. H., “Stimulated Optical Emission in Ruby,” *Nature*, Vol. 187, 1960, pp. 493–494.
- [8] Jahn, R. G., *Physics of Electric Propulsion*, McGraw-Hill, Inc., New York, 1968.
- [9] Choueiri, E. Y., “Fundamental Difference Between the Two Variants of Hall Thrusters: SPT and TAL,” *37th AIAA Joint Propulsion Conference*, Salt Lake City, Utah, 2001.
- [10] Goebel, D. M. and Katz, I., *Fundamentals of Electric Propulsion*, John Wiley & Sons, Hoboken, NJ, 2008.
- [11] Hofer, R. R., *Development and Characterization of High-Efficiency, High-Specific Impulse Xenon Hall Thrusters*, Doctoral dissertation, University of Michigan, 2004.
- [12] Kim, V., “Main Physical Features and Processes Determining the Performance of Stationary Plasma Thrusters,” *Journal of Propulsion and Power*, Vol. 14, No. 5, 1998, pp. 736–743.
- [13] King, L. B., *Transport-Property and Mass Spectral Measurements in the Plasma Exhaust Plume of a Hall-Effect Space Propulsion System*, Doctoral dissertation, University of Michigan, 1998.

- [14] Keidar, M., Boyd, I. D., and Beilis, I. I., “Plasma Flow and Plasma-Wall Transition in Hall Thruster Channel,” *Physics of Plasmas*, Vol. 8, No. 12, 2001, pp. 5315–5322.
- [15] van de Sande, M. C. M., *Laser Scattering on Low Temperature Plasmas*, Doctoral dissertation, Eindhoven University of Technology, 2002.
- [16] Mott-Smith, H. M. and Langmuir, I., “The Theory of Collectors in Gaseous Discharges,” *Physical Review*, Vol. 28, 1926, pp. 727–763.
- [17] Dorf, L., Raitses, Y., and Fisch, N. J., “Electrostatic Probe Apparatus for Measurements in the Near-Anode Region of Hall Thrusters,” *Review of Scientific Instruments*, Vol. 75, No. 5, 2004, pp. 1255–1260.
- [18] Hutchinson, I. H., *Principles of Plasma Diagnostics*, Cambridge University Press, New York City, 2nd ed., 2002.
- [19] Warner, K. and Heiftje, G. M., “Thomson Scattering from Analytical Plasmas,” *Spectrochimica Acta Part B*, Vol. 57, 2002, pp. 201–241.
- [20] Muraoka, K. and Maeda, M., *Laser-Aided Diagnostics of Plasmas and Gases*, Series in Plasma Physics, Institute of Physics Publishing, London, 2001.
- [21] Chiu, Y. H., Austin, B. L., Williams, S., and Dressler, R. A., “Passive Optical Diagnostic of Xe-Propelled Hall Thrusters. I. Emission Cross Sections,” *Journal of Applied Physics*, Vol. 99, 2006.



- [22] Karabadzhak, G. F., Chiu, Y. H., and Dressler, R. A., “Passive Optical Diagnostics of Xe-Propelled Hall Thrusters. II. Collisional-Radiative Model,” *Journal of Applied Physics*, Vol. 99, 2006.
- [23] Bowles, K. L., “Observations of Vertical-Incidence Scatter from the Ionosphere at 41 Mc/sec,” *Physical Review Letters*, Vol. 1, No. 12, 1958, pp. 454–455.
- [24] Fiocco, G. and Thompson, E., “Thomson Scattering of Optical Radiation from an Electron Beam,” *Physical Review Letters*, Vol. 10, No. 3, 1963, pp. 89–91.
- [25] Funfer, E., Kronast, B., and Kunze, H.-J., “Experimental Results on Light Scattering by a Theta-Pinch Plasma Using a Ruby Laser,” *Physics Letters*, Vol. 5, 1963, pp. 125–127.
- [26] Schwarz, S. E., “Scattering of Optical Pulses from Nonequilibrium Plasma,” *Proceedings of the IEEE*, Vol. 51, No. 10, 1963, pp. 1362.
- [27] Evans, D. E. and Katzenstein, J., “Laser Light Scattering in Laboratory Plasmas,” *Reports on Progress in Physics*, Vol. 32, 1969, pp. 207–271.
- [28] Peacock, N. J., Robinson, D. C., Forrest, M. J., Wilcock, P. D., and Sannikov, V. V., “Measurement of the Electron Temperature by Thomson Scattering in Tokamak T3,” *Nature*, Vol. 224, 1969, pp. 488–490.

- [29] Johnson, D., Dimock, D., Grek, B., Long, D., McNeill, D., Palladino, R., Robinson, J., and Tolnas, E., “TFTR Thomson Scattering System,” *Review of Scientific Instruments*, Vol. 56, 1985, pp. 1015–1017.
- [30] Glenzer, S. H., Alley, W. E., Estabrook, K. G., De Groot, J. S., Haines, J. H., Hammer, J. H., Jadaud, J.-P., MacGowan, B. J., Moody, J. D., Rozmus, W., Suter, L. J., and Williams, E. A., “Thomson Scattering from Laser Plasmas,” *40th Annual Meeting of the Division of Plasma Physics, LLNL*, New Orleans, LA, 1998.
- [31] Huang, M. and Hieftje, G., “Thomson Scattering from an ICP,” *Spectrochimica Acta Part B*, Vol. 40, No. 10-12, 1985, pp. 1387–1400.
- [32] Huang, M., Marshall, K., and Hieftje, G., “Electron Temperatures and Electron Number Densities Measured by Thomson Scattering in the Inductively Coupled Plasma,” *Analytical Chemistry*, Vol. 58, 1986, pp. 207–210.
- [33] Hidaka, R., Ooki, T., Takeda, K., Kondo, K., Kanda, H., Uchino, K., Matsuda, Y., Muraoka, K., and Akazaki, M., “Ruby-Laser Scattering Diagnostics of a Supersonic Plasma Flow for Low-Pressure Plasma Spraying,” *Japanese Journal of Applied Physics*, Vol. 26, No. 10, 1987, pp. 1724–1726.
- [34] Sakoda, T., Momii, S., Uchino, K., Muraoka, K., Bowden, M., Maeda, M., Manabe, Y., Kitagawa, M., and Kimura, T., “Thomson Scattering Diagnostics of an ECR Processing Plasma,” *Japanese Journal of Applied Physics*, Vol. 30, No. 8A, 1991, pp. 1425–1427.

- [35] Muraoka, K., Uchino, K., and Bowden, M. D., “Diagnostics of Low-Density Glow Discharge Plasmas Using Thomson Scattering,” *Plasma Physics and Controlled Fusion*, Vol. 40, 1998, pp. 1221–1239.
- [36] van de Sanden, M. C. M., Janssen, G. M., de Regt, J. M., Schram, D. C., van der Mullen, J. A. M., and van der Sijde, B., “A Combined Thomson-Rayleigh Scattering Diagnostic Using an Intensified Photodiode Array,” *Review of Scientific Instruments*, Vol. 63, No. 6, 1992, pp. 3369–3377.
- [37] van der Meiden, H. J., Al, R. S., Barth, C. J., Donne, A. J. H., Engeln, R., Goedheer, W. J., de Groot, B., Kleyn, A. W., Koppers, W. R., Lopez Cardozo, N. J., van de Pol, M. J., Prins, P. R., Schram, D. C., Shumak, A. E., Smeets, P. H. M., Vijvers, W. A. J., Westerhout, J., Wright, G. M., and van Rooij, G. J., “High Sensitivity Imaging Thomson Scattering for Low Temperature Plasma,” *Review of Scientific Instruments*, Vol. 79, 2008.
- [38] Bowden, M. D., Okamoto, T., Kimura, F., Muta, H., Uchida, K., Muraoka, K., Sakoda, T., Maeda, M., Manabe, Y., Kitagawa, M., and Kimura, T., “Thomson Scattering Measurements of Electron Temperature and Density in an Electron Cyclotron Resonance Plasma,” *Journal of Applied Physics*, Vol. 73, No. 6, 1993, pp. 2732–2738.
- [39] Hori, T., Bowden, M. D., Uchino, K., and Muraoka, K., “Measurement of Non-Maxwellian Electron Energy Distributions in an Inductively Coupled Plasma,”

*Applied Physics Letters*, Vol. 69, No. 24, 1996, pp. 3683–3685.

- [40] Hori, T., Kogano, M., Bowden, M. D., Uchino, K., and Muraoka, K., “A Study of Electron Energy Distributions in an Inductively Coupled Plasma by Laser Thomson Scattering,” *Journal of Applied Physics*, Vol. 83, No. 4, 1998, pp. 1909–1916.
- [41] Prokisch, C., Bilgic, A. M., Voges, E., Broekaert, J. A. C., Jonkers, J., van de Sande, M., and van der Mullen, J. A. M., “Photographic Plasma Images and Electron Number Density as well as Electron Temperature Mappings of a Plasma Sustained with a Modified Argon Microwave Plasma Torch (MPT) Measured by Spatially Resolved Thomson Scattering,” *Spectrochimica Acta Part B*, Vol. 54, No. 9, 1999, pp. 1253–1266.
- [42] van der Mullen, J., Boidin, G., and van de sandea, M., “High-Resolution Electron Density and Temperature Maps of a Microwave Plasma Torch Measured with a 2-D Thomson Scattering System,” *Spectrochimica Acta Part B*, Vol. 59, 2004, pp. 929–940.
- [43] Bowden, M. D., Goto, Y., Yanaga, H., Howarth, P. J. A., Uchino, K., and Muraoka, K., “A Thomson Scattering Diagnostic System for Measurement of Electron Properties of Processing Plasmas,” *Plasma Sources Science & Technology*, Vol. 8, 1999, pp. 203–209.

- [44] Bakker, L. P., Freriks, J. M., de Hoog, F. J., and Kroesen, G. M. W., “Thomson Scattering Using an Atomic Notch Filter,” *Review of Scientific Instruments*, Vol. 71, No. 5, 2000, pp. 2007–2014.
- [45] Miles, R. B., Yalin, A. P., Tang, Z., Zaidi, S. H., and Forkey, J. N., “Flow Field Imaging Through Sharp-Edged Atomic and Molecular "Notch" Filters,” *Measurement Science and Technology*, Vol. 12, 2001, pp. 442–451.
- [46] Zaidi, S. H., Tang, Z., Yalin, A. P., Barker, P., and Miles, R. B., “Filtered Thomson Scattering in an Argon Plasma,” *American Institute of Aeronautics and Astronautics Journal*, Vol. 40, No. 6, 2002, pp. 1087–1093.
- [47] Lee, W. and Lempert, W. R., “Spectrally Filtered Raman/Thomson Scattering Using a Rubidium Vapor Filter,” *American Institute of Aeronautics and Astronautics Journal*, Vol. 40, No. 12, 2002, pp. 2504–2510.
- [48] Kono, A. and Nakatani, K., “Efficient Multichannel Thomson Scattering Measurement System for Diagnostics of Low-Temperature Plasmas,” *Review of Scientific Instruments*, Vol. 71, 2000, pp. 2716–2721.
- [49] Yamamoto, N., Tomita, K., Yamasaki, N., Tsuru, T., Ezaki, T., Kotani, Y., Uchino, K., and Nakashima, H., “Measurements of Electron Density and Temperature in a Miniature Microwave Discharge Ion Thruster Using Laser Thomson Scattering Technique,” *Plasma Sources Science & Technology*, Vol. 19, 2010, pp. 1–7.

- [50] Miles, R. B., Lempert, W. R., and Forkey, J. N., “Laser Rayleigh Scattering,” *Measurement Science and Technology*, Vol. 12, 2001, pp. R33–R51.
- [51] Sheffield, J., *Plasma Scattering of Electromagnetic Radiation*, Academic Press, Inc., New York, 1975.
- [52] Jackson, J. D., *Classical Electrodynamics*, John Wiley & Sons, Inc., New York, 3rd ed., 1999.
- [53] Smith, G. S., *An Introduction to Classical Electromagnetic Radiation*, Cambridge University Press, Cambridge, 1997.
- [54] Kunze, H.-J., *The Laser as a Tool for Plasma Diagnostics*, Plasma Diagnostics, North-Holland Publishing Company, Amsterdam, 1968.
- [55] Mainfray, G. and Manus, C., “Multiphoton Ionization of Atoms,” *Reports on Progress in Physics*, Vol. 54, 1991, pp. 1333–1372.
- [56] Lambropoulos, P., “Mechanisms for Multiple Ionization of Atoms by Strong Pulsed Lasers,” *Physical Review Letters*, Vol. 55, No. 20, 1985, pp. 2141–2144.
- [57] Agostini, P., Barjot, G., Mainfray, G., Manus, C., and Thebault, J., “Multiphoton Ionization of Rare Gases at 1.06  $\mu\text{m}$  and 0.53  $\mu\text{m}$ ,” *IEEE Journal of Quantum Electronics*, Vol. QE-6, No. 12, 1970, pp. 782–788.
- [58] Merlino, R. L., “Understanding Langmuir Probe Current-Voltage Characteristics,” *American Journal of Physics*, Vol. 75, No. 12, 2007, pp. 1078–1085.

- [59] Chen, F. F., *Plasma Physics and Controlled Fusion*, Vol. 1, Springer Science + Business Media, LLC, New York, NY, 2006.
- [60] Sommerville, J. D., *Hall-Effect Thruster-Cathode Coupling*, Dissertation, Michigan Technological University, 2009.
- [61] Peterson, E. W. and Talbot, L., “Collisionless Electrostatic Single-Probe and Double-Probe Measurements,” *American Institute of Aeronautics and Astronautics Journal*, Vol. 8, No. 12, 1970, pp. 2215–2219.
- [62] Druyvesteyn, M. J., “Der Niedervoltbogen,” *Zeitschrift für Physik*, Vol. 64, 1930, pp. 781–789.
- [63] Johnson, E. O. and Malter, L., “A Floating Double Probe Method for Measurements in Gas Discharges,” *Physical Review*, Vol. 80, No. 1, 1950, pp. 58–68.
- [64] Huddleston, R. H. and Leonard, S. L., *Plasma Diagnostic Techniques*, Academic Press, Inc., New York, 1965.
- [65] Brockhaus, A., Borchardt, C., and Engemann, J., “Langmuir Probe Measurements in Commercial Plasma Plants,” *Plasma Sources Science & Technology*, Vol. 3, No. 4, 1994, pp. 539–544.
- [66] Swift, J. D. and Schwar, M. J. R., *Electrical Probes for Plasma Diagnostics*, American Elsevier Publishing Company, Inc., New York, 1969.

- [67] Washeleski, R. L. and King, L. B., "Characterization of the Plasma Plume from a LaB6 Cathode: A Comparison of Probe Techniques," *45th AIAA/ASME/SAE/ASEE Joint Propulsion Conference and Exhibit*, Denver, CO, 2009.
- [68] King, D., "Development of the BPT Family of U.S.-Designed Hall Current Thrusters for Commercial LEO and GEO Applications," *34th AIAA/ASME/SAE/ASEE Joint Propulsion Conference & Exhibit*, Cleveland, OH, 1998.
- [69] Wilson, F., "Development Status of the BPT Family of Hall Current Thrusters," *35th AIAA/ASME/SAE/ASEE Joint Propulsion Conference & Exhibit*, Los Angeles, CA, 1999.
- [70] de Grys, K., "BPT Hall Thruster Plume Characterization," *35th AIAA/ASME/SAE/ASEE Joint Propulsion Conference & Exhibit*, Los Angeles, CA, 1999.
- [71] Kieckhafer, A. W., Massey, D. R., King, L. B., and Sommerville, J. D., "Effect of Segmented Anodes on the Beam Profile of a Hall Thruster," *40th AIAA/ASME/SAE/ASEE Joint Propulsion Conference & Exhibit*, Fort Lauderdale, FL, 2004.
- [72] Sommerville, J. D. and King, L. B., "Effect of Cathode Position on Hall-Effect Thruster Performance and Cathode Coupling Voltage," *43rd AIAA/ASME/SAE/ASEE Joint Propulsion Conference & Exhibit*, Cincinnati, OH, 2007.



- [73] Hobbs, P. C. D., *Building Electro-Optical Systems: Making It All Work*, John Wiley & Sons, Inc., New York, 1st ed., 2000.
- [74] Rahn, J. P., “How to Extinguish a Light Beam Without Scatter,” *Applied Optics*, Vol. 17, No. 16, 1978, pp. 2475–2476.
- [75] Aldrich, J., “R. A. Fisher and the Making of Maximum Likelihood 1912-1922,” *Statistical Science*, Vol. 12, No. 3, 1997, pp. 162–176.
- [76] Fisher, R. A., “On the Mathematical Foundations of Theoretical Statistics,” *Philosophical Transactions of the Royal Society A*, 1922, pp. 309–368.
- [77] Myung, J., “Tutorial on Maximum Likelihood Estimation,” *Journal of Mathematical Psychology*, Vol. 47, 2003, pp. 90–100.
- [78] Yates, R. D. and Goodman, D. J., *Probability and Stochastic Processes*, John Wiley & Sons, Inc., Hoboken, 2nd ed., 2005.
- [79] Ross, S. M., “Peirce’s Criterion for the Elimination of Suspect Experimental Data,” *Journal of Engineering Technology*, Vol. 20, No. 2, 2003, pp. 38–41.
- [80] Holman, J. P., *Experimental Methods for Engineers*, McGraw-Hill, New York, seventh ed., 2001.
- [81] Dussault, D. and Hoess, P., “Noise Performance Comparison of ICCD with CCD and EMCCD Cameras,” *Society of Photo-Optical Instrumentation Engineers Conference*, 2004.

- [82] Sudit, I. D. and Woods, R. C., "A Study of the Accuracy of Various Langmuir Probe Theories," *Journal of Applied Physics*, Vol. 76, No. 8, 1994, pp. 4488–4498.
- [83] Castro, R. M., Cirino, G. A., Verdonck, P., Macial, H. S., Massi, M., Pisani, M. B., and Masano, R. D., "A Comparative Study of Single and Double Langmuir Probe Techniques for RF Plasma Characterization," *Contributions to Plasma Physics*, Vol. 39, No. 3, 1999, pp. 235–246.
- [84] Goodall, C. V. and Smith, D., "A Comparison of the Methods of Determining Electron Densities in Afterglow Plasmas from Langmuir Probe Characteristics," *Plasma Physics*, Vol. 10, No. 249-261, 1968.
- [85] Demidov, V. I., Ratynskaia, S. V., and Rypdal, K., "Electric Probes for Plasmas: The Link Between Theory and Instrument," *Review of Scientific Instruments*, Vol. 73, No. 10, 2002, pp. 3409–3439.
- [86] Meulenbroeks, R. F. G., Steenbakkens, M. F. M., Qing, Z., van de Sanden, M. C. M., and Schram, D. C., "Four Ways to Determine the Electron Density in Low-Temperature Plasmas," *Physics Review E*, Vol. 49, No. 3, 1994, pp. 2272–2275.
- [87] Bowden, M. D., Goto, Y., Hori, T., Uchino, K., Muraoka, K., and Noguchi, M., "Detection Limit of Laser Thomson Scattering for Low Density Discharge Plasmas," *Japanese Journal of Applied Physics*, Vol. 38, 1999, pp. 3723–3730.

- [88] Tsikata, S., *Small-Scale Electron Density Fluctuations in the Hall Thruster, Investigated by Collective Light Scattering*, Doctoral dissertation, Ecole Polytechnique, 2009.

# Appendix A

## Langmuir Probe Traces

Langmuir probe traces taken at all operating conditions (see Table 7.2) are displayed in the order of measurement (see Table 7.1). With the exception of the 300 V 40 SCCM operating condition all of the probe traces conform very well to the expected hyperbolic tangent shape. It seems that at the 300 V 40 SCCM operating condition the plasma was oscillating between two states as evidenced by the probe traces (See Figures A.1 and A.2).

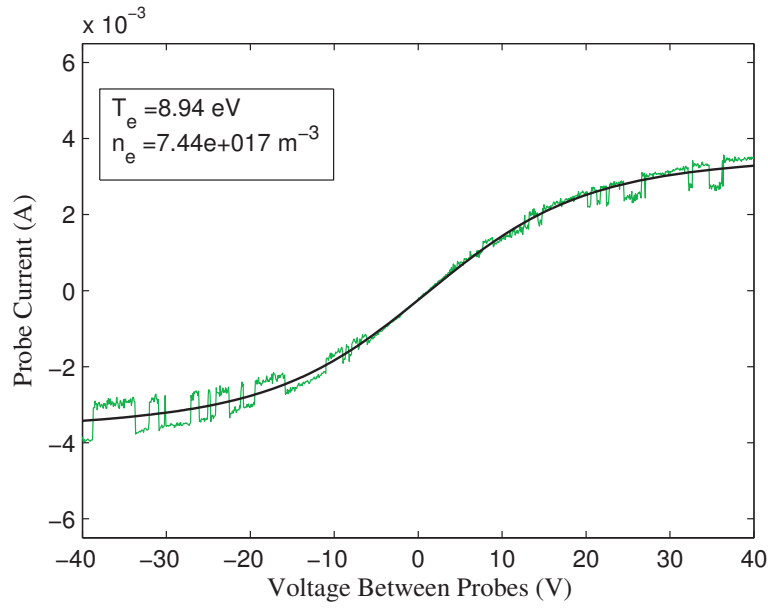


**Figure A.1:** First Langmuir probe trace taken at 300 V discharge and 40 SCCM mass flow rate.

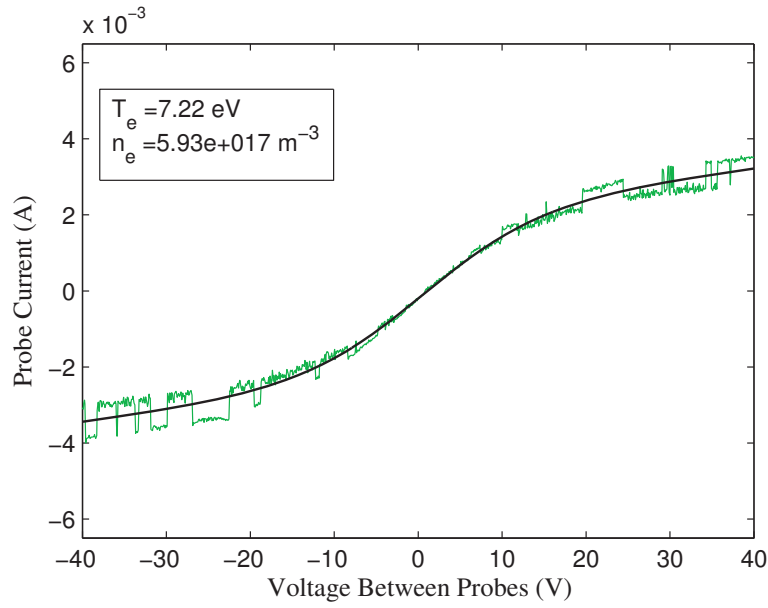


**Figure A.2:** Second Langmuir probe trace taken at 300 V discharge and 40 SCCM mass flow rate.

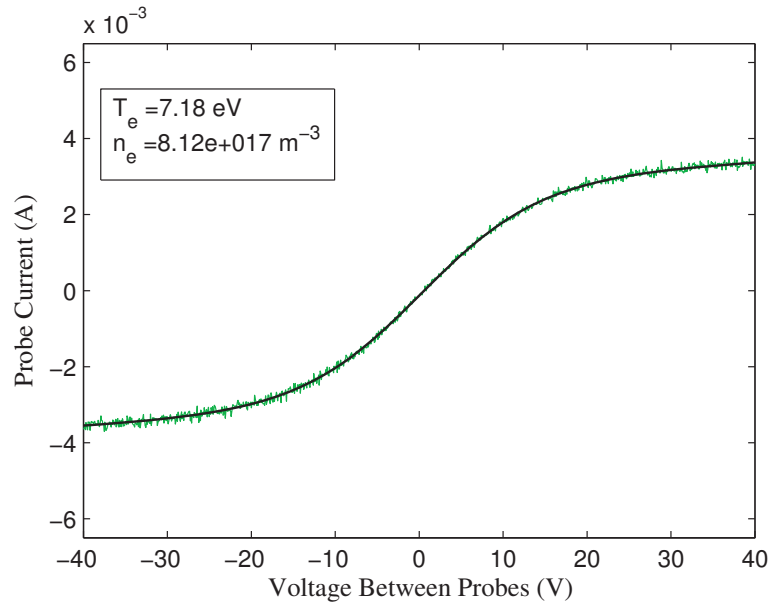


**Figure A.3:** First Langmuir probe trace taken at 350 V discharge and 60 SCCM mass flow rate.

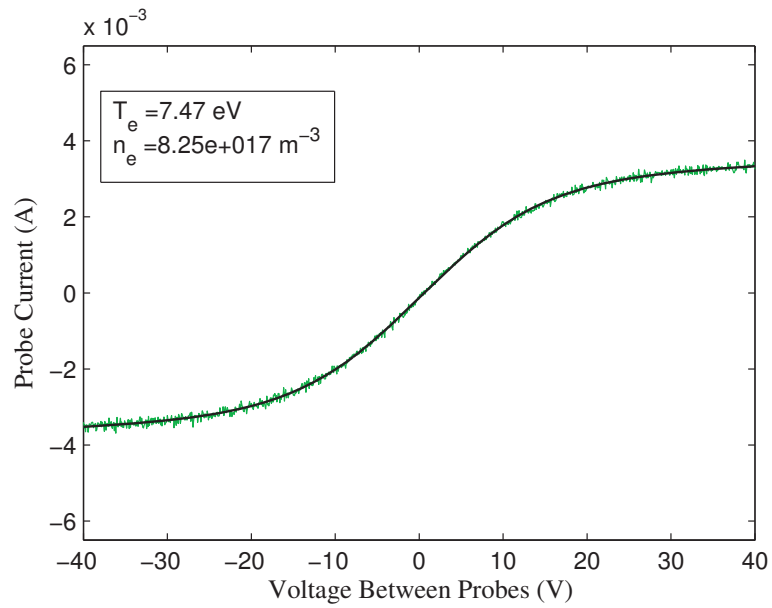


**Figure A.4:** Second Langmuir probe trace taken at 350 V discharge and 60 SCCM mass flow rate.

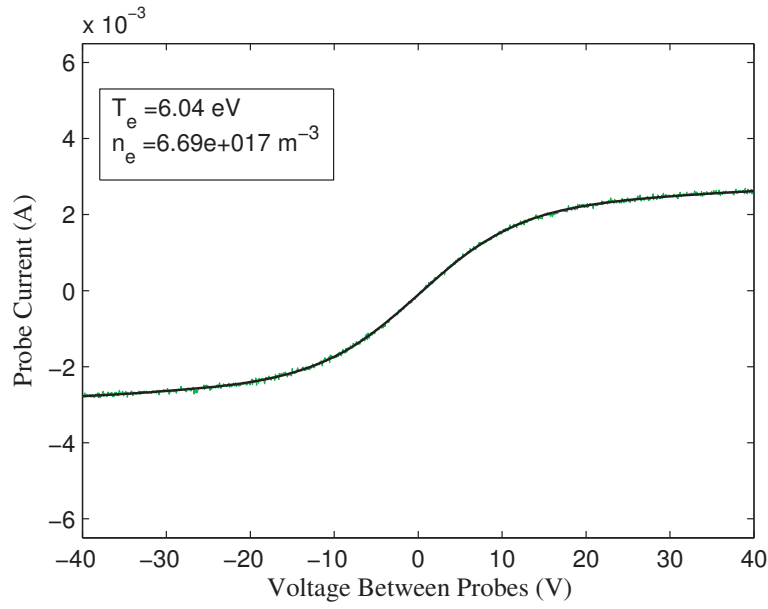


**Figure A.5:** First Langmuir probe trace taken at 350 V discharge and 50 SCCM mass flow rate.

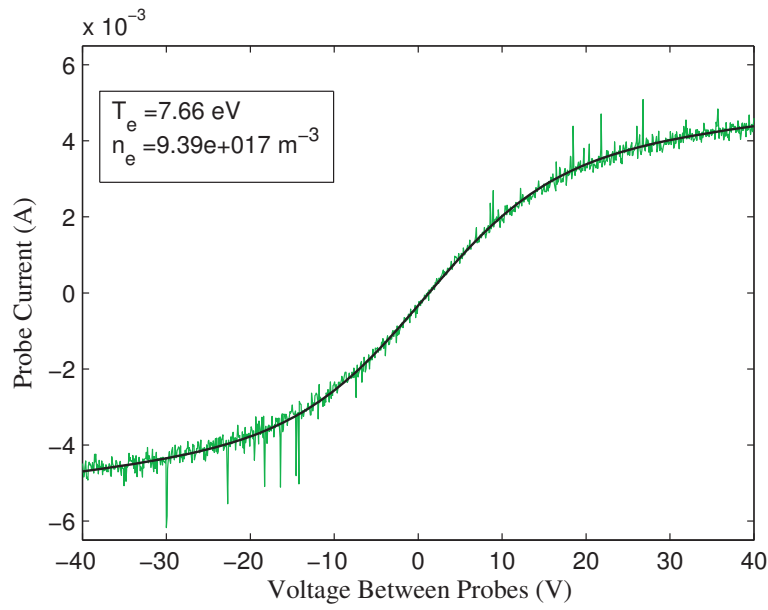


**Figure A.6:** Second Langmuir probe trace taken at 350 V discharge and 50 SCCM mass flow rate.

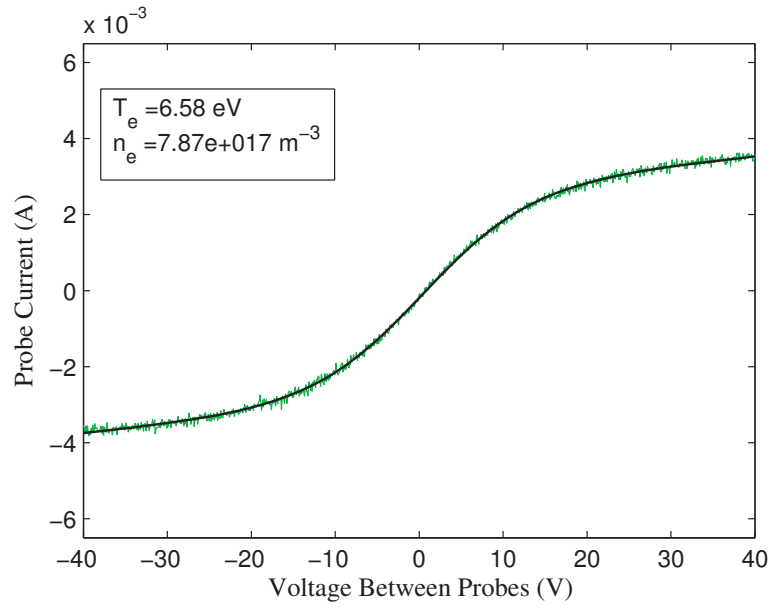


**Figure A.7:** First Langmuir probe trace taken at 400 V discharge and 40 SCCM mass flow rate.

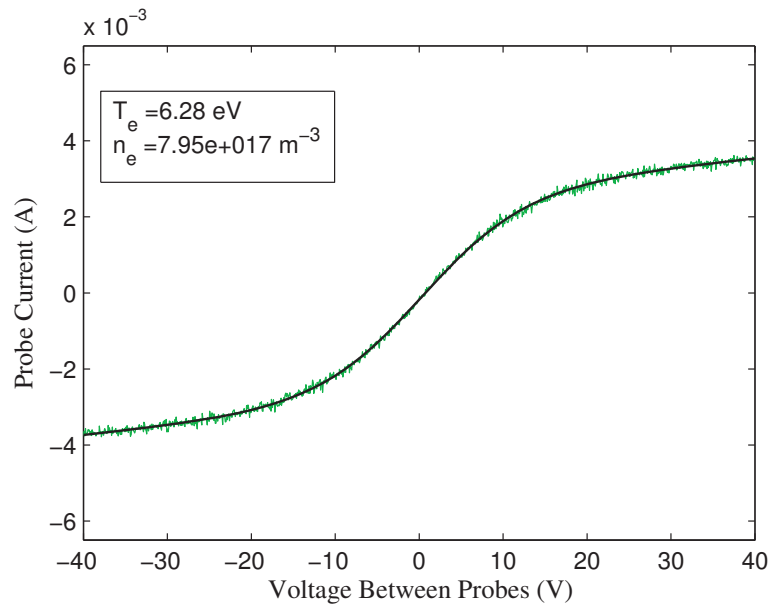


**Figure A.8:** Second Langmuir probe trace taken at 400 V discharge and 40 SCCM mass flow rate.



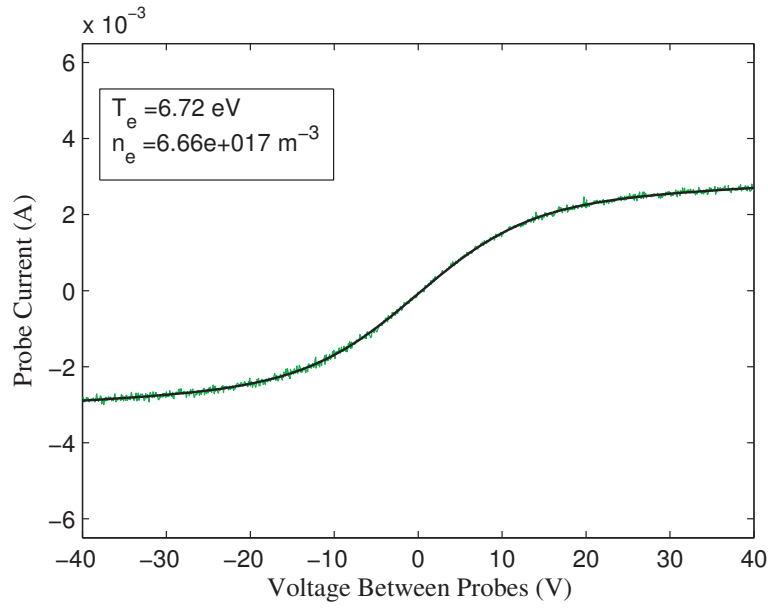


**Figure A.9:** First Langmuir probe trace taken at 300 V discharge and 50 SCCM mass flow rate.

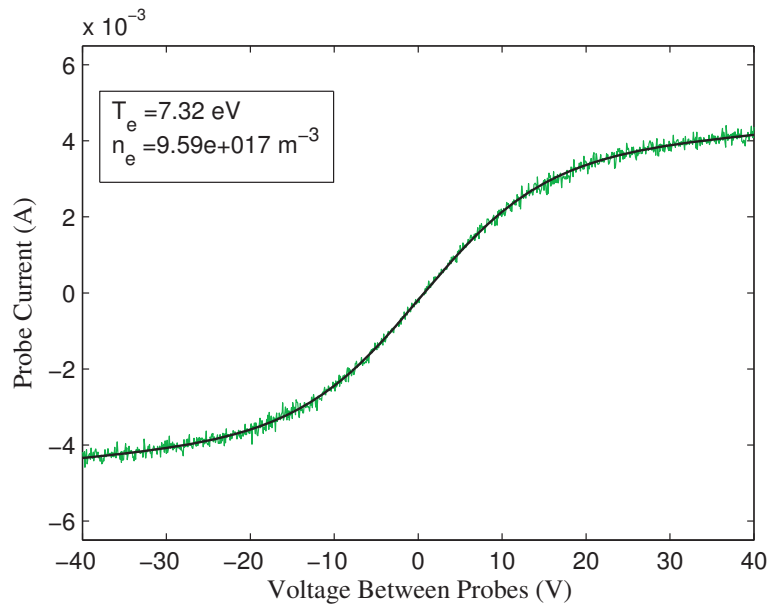


**Figure A.10:** Second Langmuir probe trace taken at 300 V discharge and 50 SCCM mass flow rate.

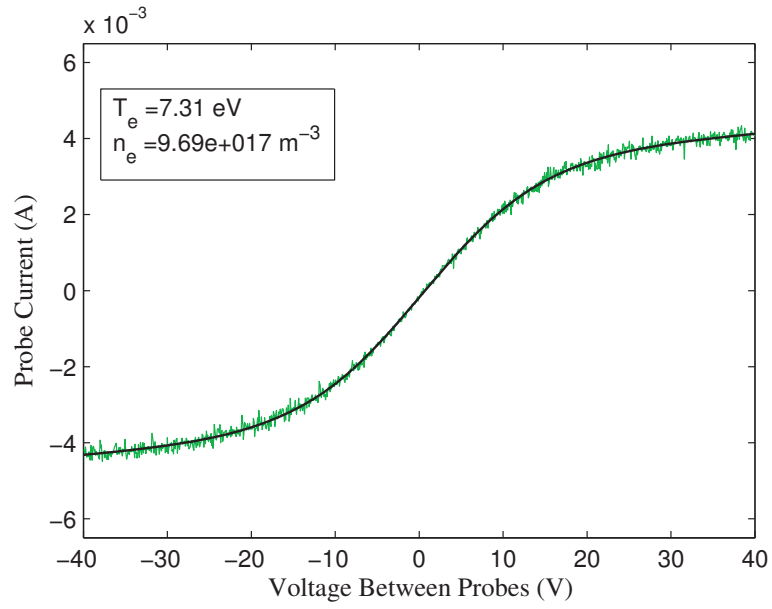


**Figure A.11:** First Langmuir probe trace taken at 350 V discharge and 40 SCCM mass flow rate.

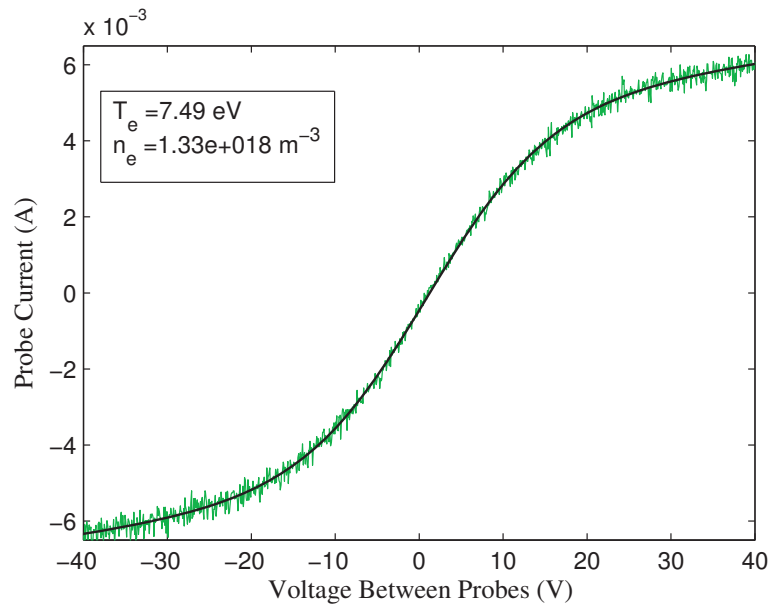


**Figure A.12:** Second Langmuir probe trace taken at 350 V discharge and 40 SCCM mass flow rate.

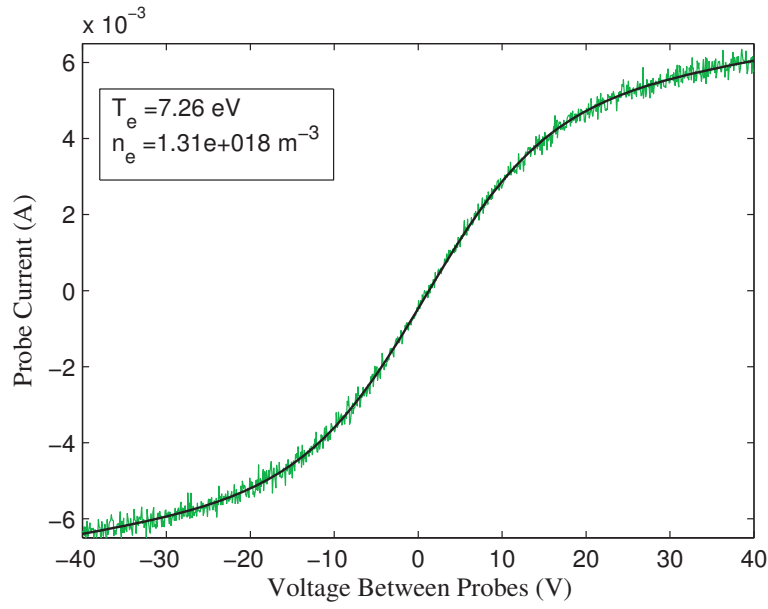


**Figure A.13:** First Langmuir probe trace taken at 400 V discharge and 60 SCCM mass flow rate.

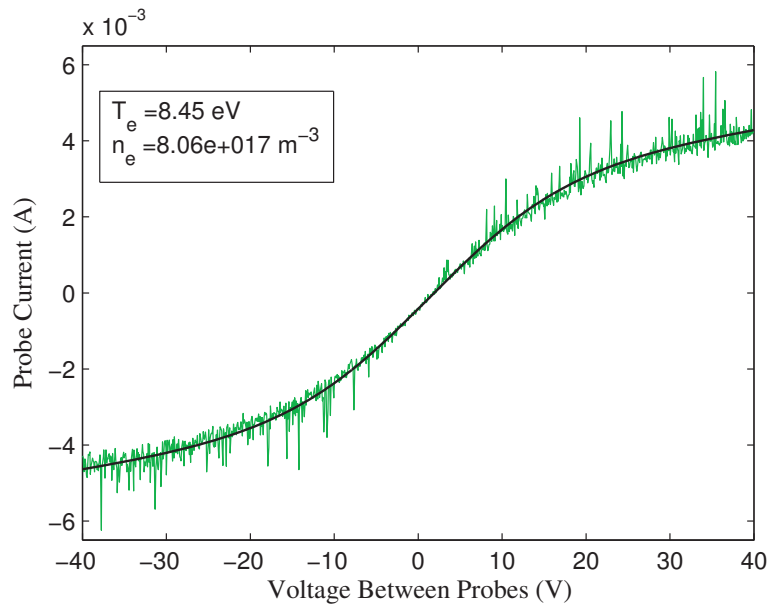


**Figure A.14:** Second Langmuir probe trace taken at 400 V discharge and 60 SCCM mass flow rate.

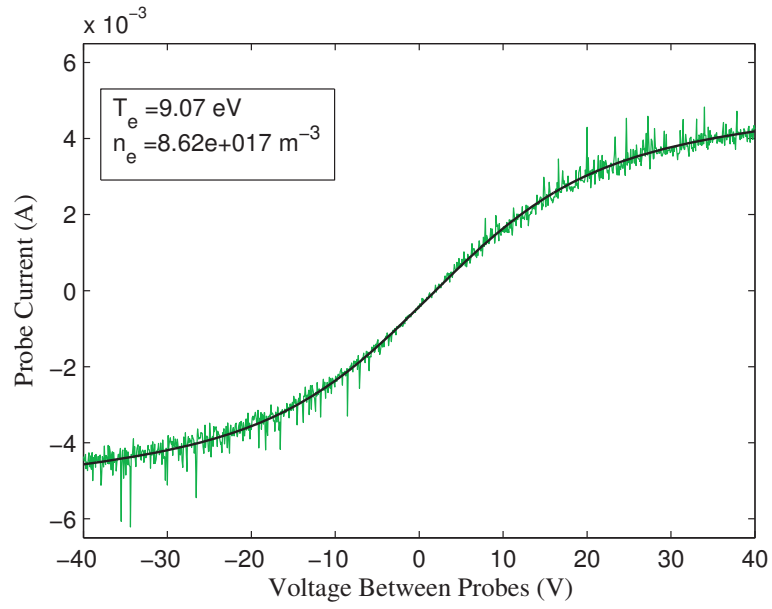


**Figure A.15:** First Langmuir probe trace taken at 400 V discharge and 50 SCCM mass flow rate.

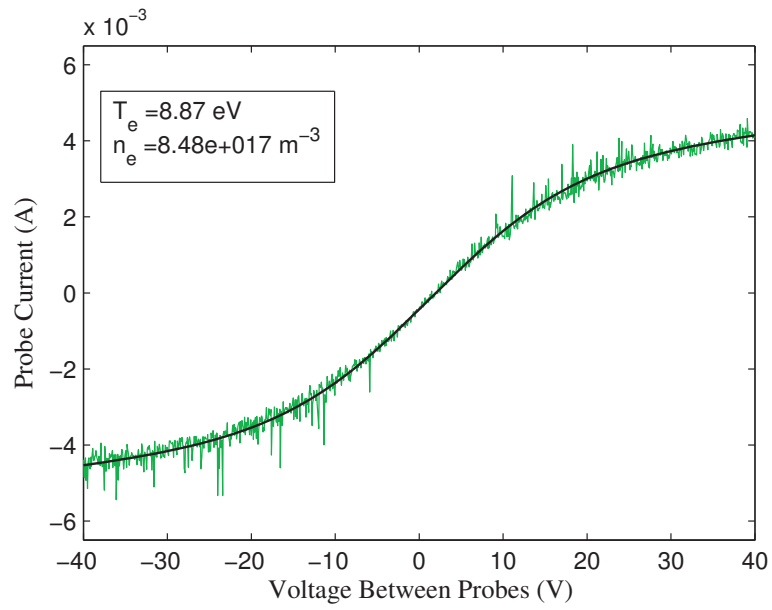


**Figure A.16:** Second Langmuir probe trace taken at 400 V discharge and 50 SCCM mass flow rate.

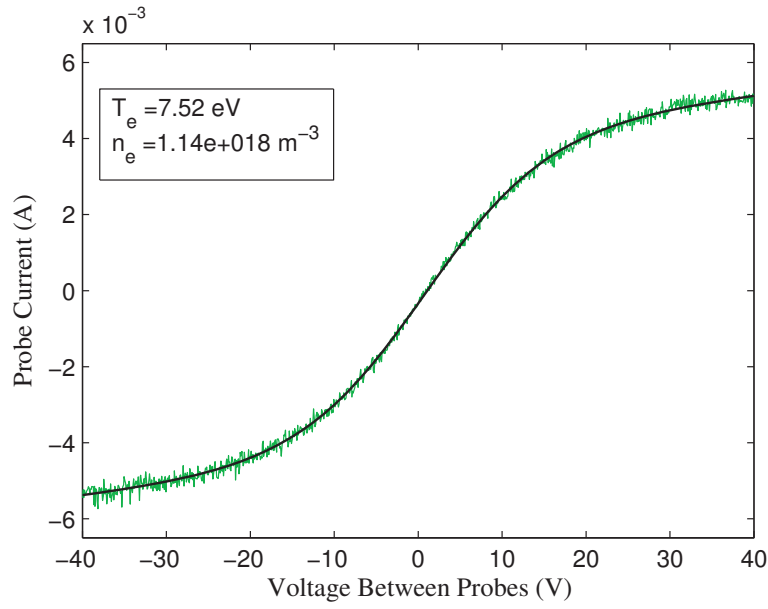


**Figure A.17:** First Langmuir probe trace taken at 300 V discharge and 60 SCCM mass flow rate.

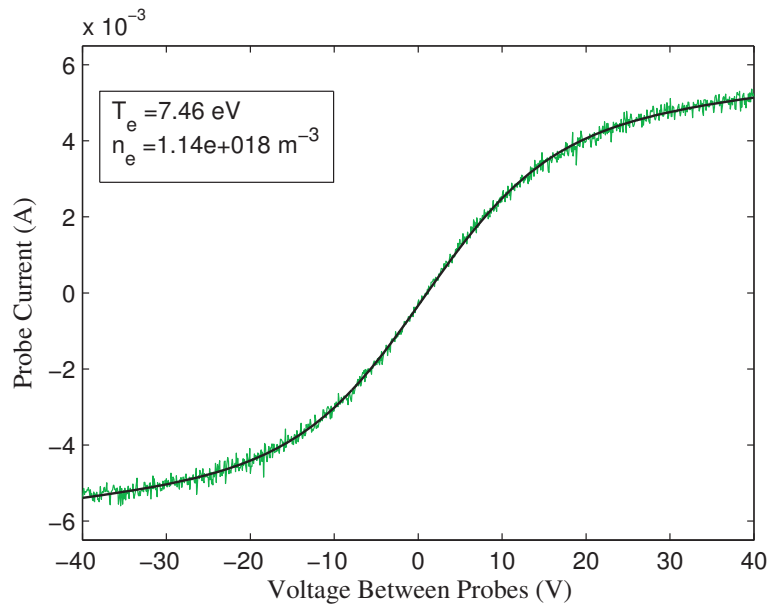


**Figure A.18:** Second Langmuir probe trace taken at 300 V discharge and 60 SCCM mass flow rate.

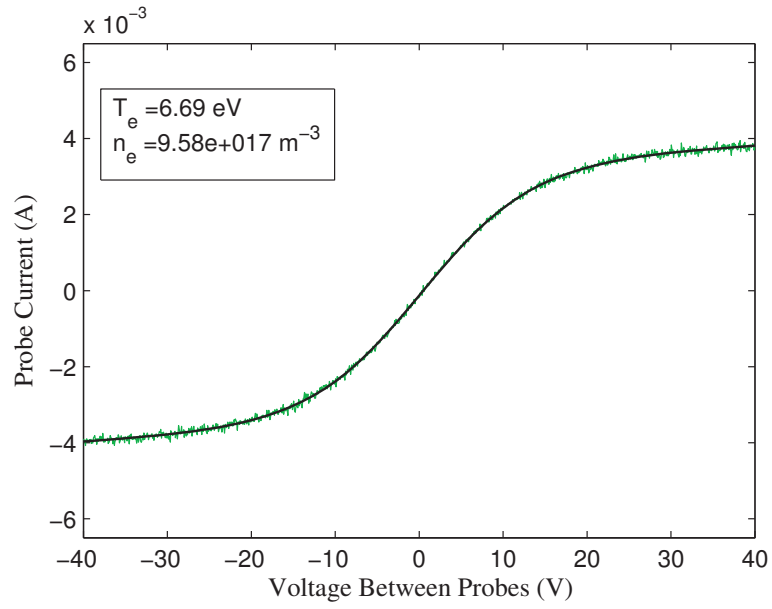


**Figure A.19:** First Langmuir probe trace taken at 350 V discharge and 80 SCCM mass flow rate.

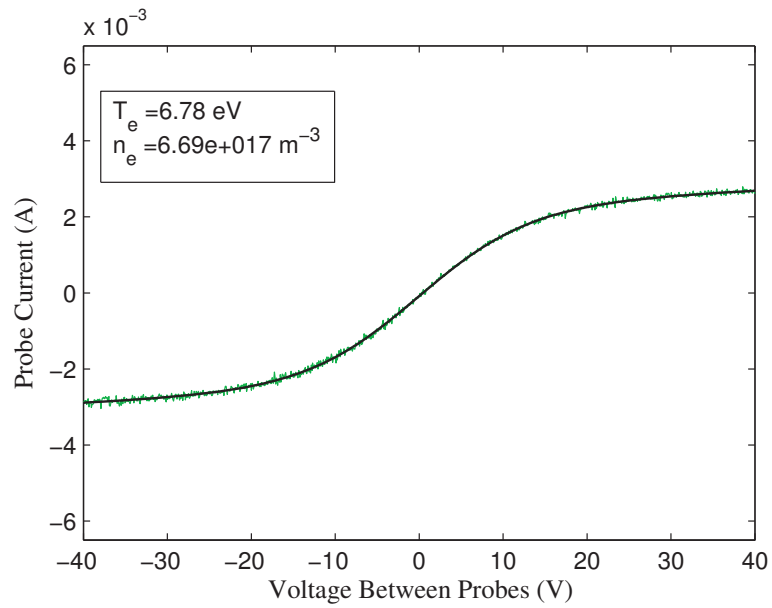


**Figure A.20:** Second Langmuir probe trace taken at 350 V discharge and 80 SCCM mass flow rate.

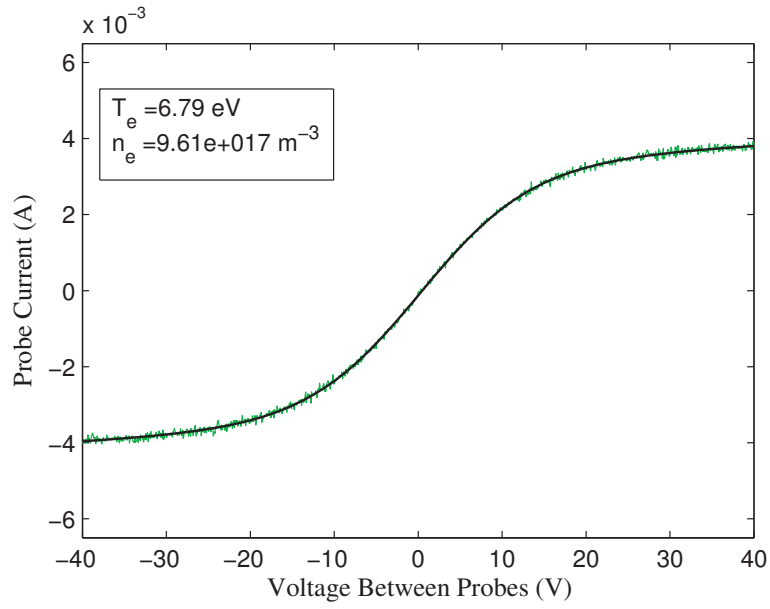


**Figure A.21:** First Langmuir probe trace taken at 450 V discharge and 60 SCCM mass flow rate.

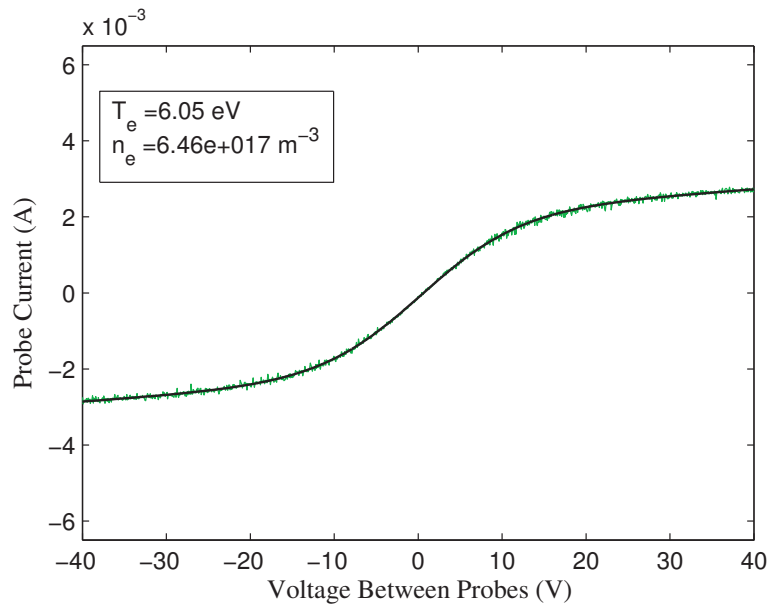


**Figure A.22:** Second Langmuir probe trace taken at 450 V discharge and 60 SCCM mass flow rate.

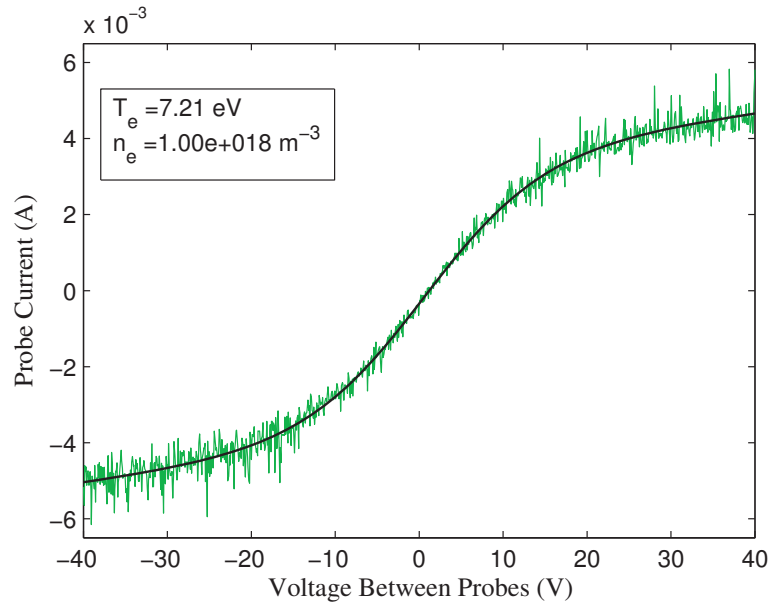


**Figure A.23:** First Langmuir probe trace taken at 350 V discharge and 70 SCCM mass flow rate.

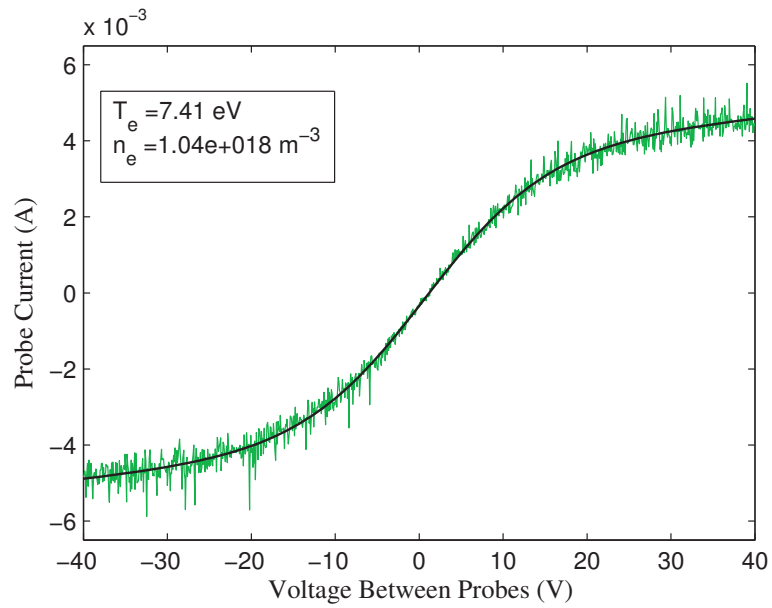


**Figure A.24:** Second Langmuir probe trace taken at 350 V discharge and 70 SCCM mass flow rate.



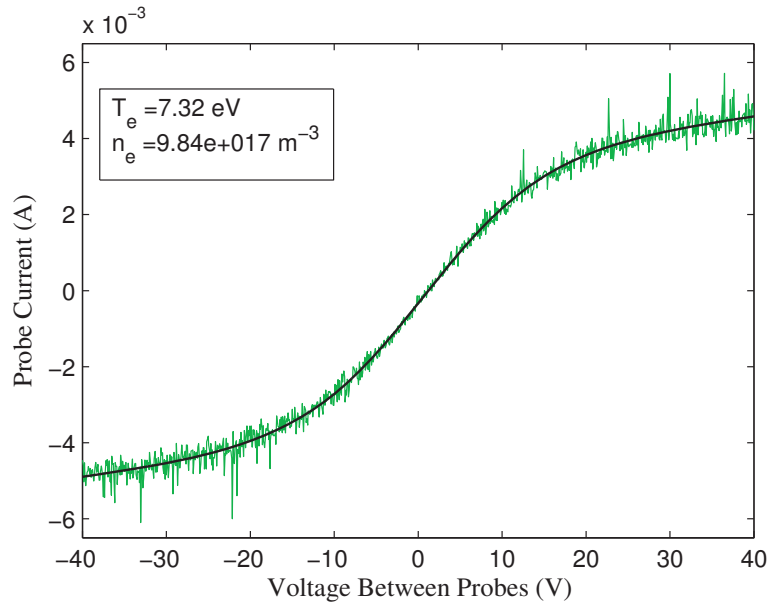


**Figure A.25:** First Langmuir probe trace taken at 250 V discharge and 60 SCCM mass flow rate.

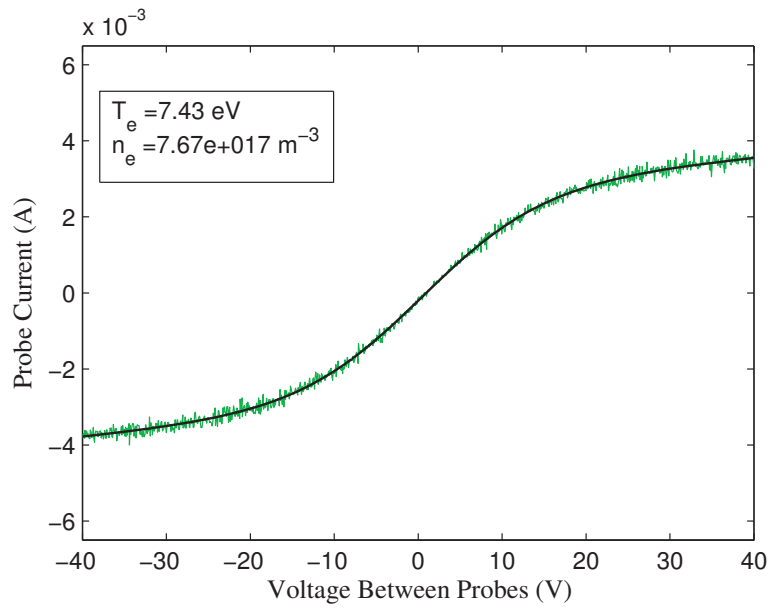


**Figure A.26:** Second Langmuir probe trace taken at 250 V discharge and 60 SCCM mass flow rate.

## Appendix B

### Folding the Spectrum

If one can make the assumption that the plasma being measured by laser Thomson scattering is isotropic along the scattering vector in the plasma the data can be processed in a special way. For a Maxwellian plasma the scattered spectrum will have a symmetric Gaussian shape. Since symmetry is assumed, the scattered signal at 534 nm should be the same as the scattered signal at 530 nm (assuming an Nd:YAG laser at 532 nm). Instead of performing maximum likelihood estimation at each wavelength, one can “fold” the spectrum about the laser line and effectively double the number of laser shots used to calculate the mean arrival rate. In order to do this the following algorithm is used:

1. All acquisitions are combined into a single three-dimensional matrix.
2. The matrix is then divided in two symmetrically about the laser line.

3. One side (positive or negative wavelength shifts) is then reflected about the laser line.
4. This new, “folded”, half is then concatenated to the other side. For this work it changes the data matrix from  $6 \times 160 \times 27,000$  into a matrix that is  $6 \times 80 \times 54,000$ .
5. The maximum likelihood algorithm of section 6.7 is then performed as normal.

This procedure is depicted graphically in Figure B.1. The result of this data transform is that there should (in theory) be twice the number of Thomson photons arriving at each wavelength. Performing maximum likelihood estimation on more acquisitions per wavelength increases confidence in the mean photon arrival rate.

In spite of the fact that an isotropic Maxwellian electron distribution was assumed for this work, this method of folding the spectrum was not used. The reason why is the presence of strong emission lines in the spectrum near 532 nm. There are strong lines spaced asymmetrically both above and below 532 nm, and when the spectrum is folded these lines cover most of the new half-spectrum. Figure B.2 shows the emission spectrum determined by maximum likelihood estimation after performing the folding operation. The corrected spectrum (total spectrum minus the emission spectrum) can be seen in Figure B.3. The large amount of subtraction noise from the line emission across the entire half-spectrum nullifies any gain in Thomson signal. While folding the spectrum does not help in this case, if the plasma lacks lines in the region of interest folding may be used to effectively increase the Thomson signal.

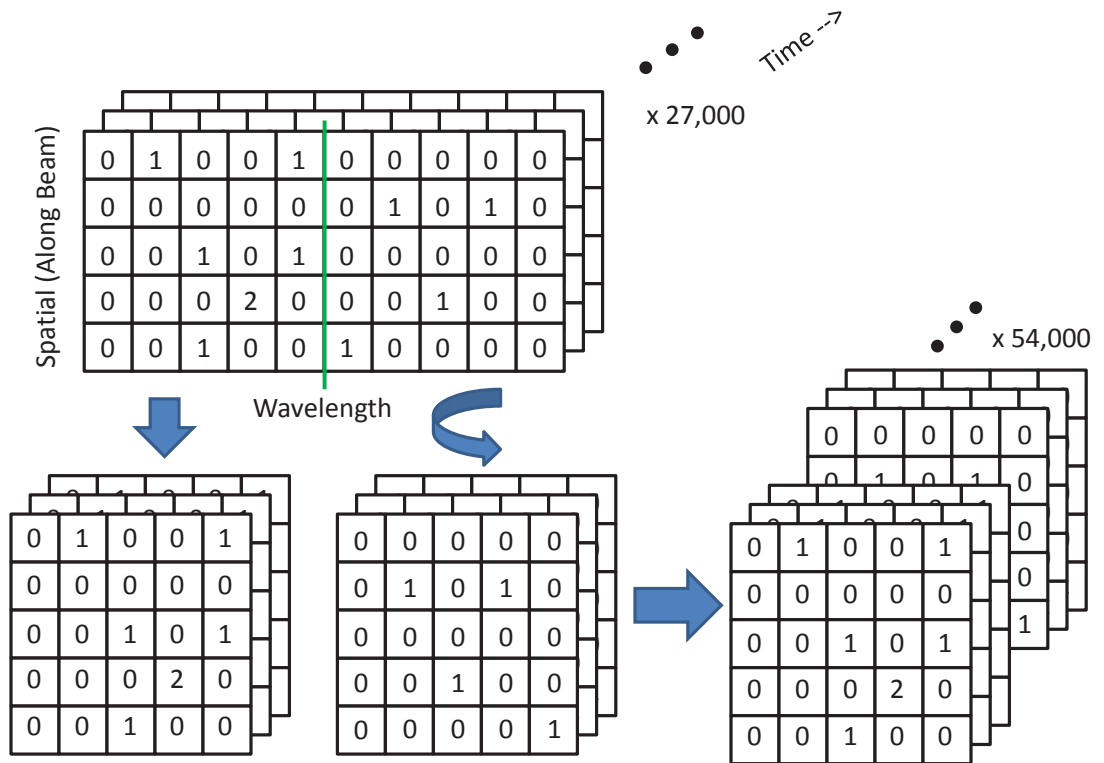


**Figure B.1:** Graphical depiction of the data folding operation.

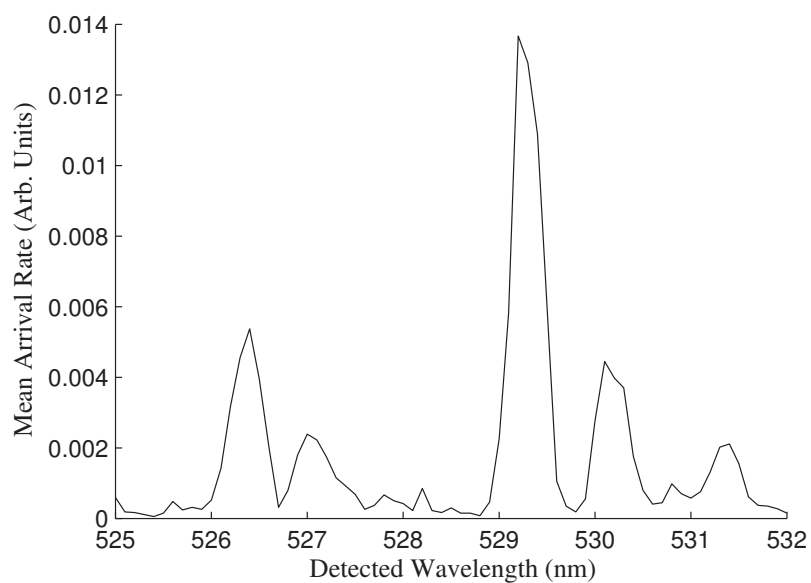


**Figure B.2:** Emission spectrum calculated at 300 V 40 SCCM after folding the data. Note that due to the folding transform emission lines cover most of the spectrum.

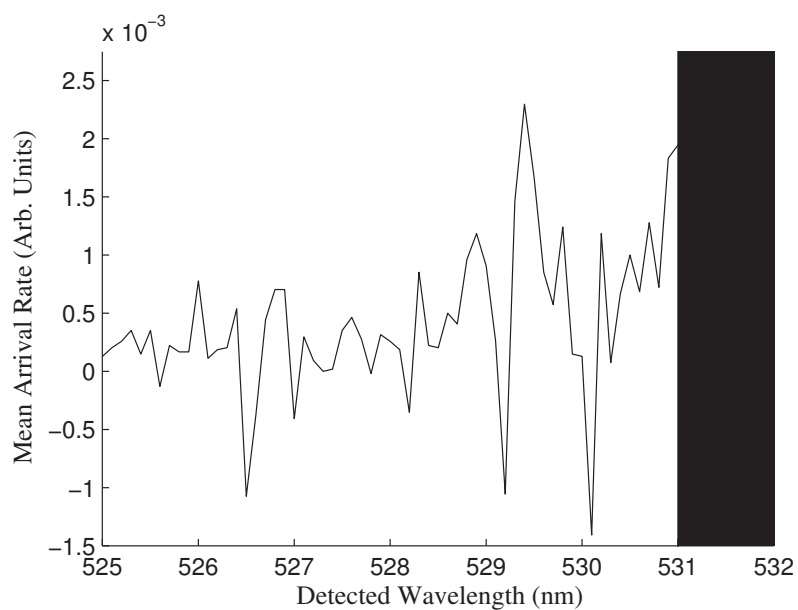


**Figure B.3:** Corrected spectrum at 300 V 40 SCCM after folding the data. Strong subtraction noise is present from the emission lines in the spectral region of interest.